POLITECHNIKA WROCŁAWSKA

WYDZIAŁ INFORMATYKI
I TELEKOMUNIKACJI

PRACA DOKTORSKA

Recognition and matching of microscopic images in 2D space

Rozpoznawanie i dopasowywanie obrazów mikroskopowych
w przestrzeni 2D

Aneta Górniak

Promotor: **prof. dr hab. inż. Ewa Skubalska-Rafajłowicz**

Promotor pomocniczy: **dr hab. inż. Andrzej Rusiecki**

WROCŁAW 2022

Abstract

The aim of this thesis is to present a new approach to using Zernike moments in problems of microscope image analysis of tissue sections. We also offer a new approach to know problems of image analysis like sequencing of microscope slides, identification of tissue types and detection of damage in microscope images. The final step is development of algorithms on the basis of Zernike moments to solve the aforementioned problems.

Medical images provide a visual representation of the interior of the human body and the function of organs and tissues. It is a broad category of images which varies greatly in terms of the subject and the means of its acquisition. It makes medical image registration an extensive field of study with a very diverse subject base ranging from of alignment of MRIs to computer-aided diagnosis or simple atlas building. Microscope images of histological sections are a subcategory of medical images. By their nature tissue sections are complex structures which often require custom-made methods of analysis and processing. Therefore, in our thesis we focus mostly on three problems of microscope image analysis. These are sequencing and tissue reconstruction, identification of types of tissue and detection of damage in microscope images.

In our approach, we rely on image descriptors built out of Zernike moments and their modified version of accumulated Zernike moments. As support, we employ other tools in the form of dedicated neural networks or logistic regression models. Using Zernike moment-based descriptors allows us to control the size of the descriptors by controlling the number and the order of moments. Such approach has many advantages carried from the properties of Zernike moments like reduction of data to process or robustness to noise and rotation invariance to begin with.

In the problem of sequencing of microscope image slides, the proposed solution uses Zernike moment-based descriptors as image representations and finds the optimal order by finding the sequence with the least value of error between subsequent entries. In the problem of recognition of tissue types from microscope images of histological sections, we use machine learning algorithms like neural networks to build classification profiles of different tissue types, and then to identify tissue with descriptors as input data. We further develop this approach into identifying tissue using random samples from the image. Here, the Zernike moment-based descriptors are calculated for the sampled images. Since Zernike moment-based descriptors work for various problems of identification, we expanded the use to the problem of detection of aberrations and other damages in tissue sections. In this case, we use Zernike moment-based descriptors to sort through tissue collections and identify images which contain missing fragments, noticeable disfigurements or do not match the profile of the collection at all.

We examine the effectiveness of Zernike moment-based descriptors and their derivatives on the presented set of problems. The data pool in all cases consists of microscope images of histological section which come in varying levels of details and magnification. We most prominently use samples of vein tissue, cardiac muscle tissue and tendon tissue, however, these are not the only types in use.

All algorithms are tailored to each type of problem. While all use Zernike moment-based descriptors at their core, some adjustments have to be made in order to properly accommodate the specifics of each problem. Each proposed solution is tested using a diverse set of data. The final results are satisfactory, and the proposed approach may find further applications. All conclusions and output data are gathered in proper figures, tables and summaries in the thesis.

Streszczenie

Tematem tej rozprawy doktorskiej są nowe metody wykorzystania momentów Zernike w problemach analizy obrazów mikroskopowych sekcji tkanek. Rozwijamy również dostępne podejście do problemów budowania sekwencji tkanek na obrazach mikroskopowych, a także problemów identyfikacji typów tkanek na obrazach oraz detekcji uszkodzeń na obrazach tkanek. Do rozwiązania użyjemy zaprojektowanych przez nas algorytmów wykorzystujących momenty Zernike.

Obrazy medyczne są wizualną reprezentacją wnętrza ludzkiego organizmu, odzwierciedlają także funkcjonowanie jego organów i tkanek. Jest to szeroka kategoria obrazów, zróżnicowanych pod względem zawartości jak i sposobu pozyskiwania. Czyni to rejestrację obrazów medycznych rozległą dziedziną badań o bardzo zróżnicowanej bazie obiektów badawczych i powiązanych problemów począwszy od wyrównywania obrazów z rezonansu magnetycznego po diagnozowanie komputerowe na podstawie sekcji histologicznych czy po prostu budowanie atlasów medycznych.

Obrazy mikroskopowe sekcji histologicznych są podkategorią obrazów medycznych. Tkanki z natury są złożonymi strukturami, a ich obrazy często wymagają odpowiednio skrojonych metod analizy i przetwarzania. Z tego względu w naszej rozprawie zawęziliśmy temat do wybranych trzech zagadnień z analizy obrazów mikroskopowych. Są to: sekwencjonowanie i rekonstrukcja tkanek, identyfikacja typów tkanek i wykrywanie uszkodzeń na obrazach mikroskopowych.

W naszym podejściu polegamy na deskryptorach obrazów zbudowanych z momentów Zernike oraz ich zmodyfikowanej wersji – skumulowanych momentach Zernike. Pozostałe narzędzia obejmują m.in. dedykowane sieci neuronowe czy modele regresji logistycznej. Użycie momentów Zernike w takiej formie pozwala nam na kontrolowanie rozmiaru deskryptora m.in. przez zmianę liczby i rzędu momentów. Ma to wiele zalet, które wynikają z właściwości momentów Zernike jak redukcja ilości danych w obiegu, zwiększona odporność na szum czy zmianę orientacji kąta.

W problemie sekwencjonowania slajdów mikroskopowych algorytm używa deskryptorów z momentów Zernike jako reprezentacji obrazów i na ich podstawie wyszukuje optymalnego porządku slajdów, czyli sekwencji o najmniejszej wartości błędu pomiędzy sąsiadującymi obrazami w kolejce. W problemie rozpoznawania typów tkanek na obrazach mikroskopowych używamy algorytmów uczenia maszynowego jak sieci neuronowe do budowy profili klas dla różnych typów tkanek, a potem do ich identyfikacji na podstawie deskryptorów obrazów. To podejście jest w dalszej części rozwinięte do identyfikacji tkanek na podstawie losowo spróbkowanych fragmentów obrazu mikroskopowego. W tym przypadku deskryptory z momentów Zernike są liczone tylko dla tych próbek, a nie całego obrazu. Z racji tego, że deskryp-

tory działają dla różnych problemów identyfikacyjnych, rozwinęliśmy ich użycie do detekcji odchyleń i uszkodzeń w obrazach tkanek. W tym przypadku używamy deskryptorów i uczenia maszynowego do przeglądania kolekcji tkanek w celu identyfikacji obrazów, na których są uszkodzone, odkształcone lub niepasujące do kolekcji tkanki.

Skuteczność proponowanego rozwiązania została sprawdzona na przedstawionym zestawie problemów. Zestaw danych testujących składa się z obrazów mikroskopowych sekcji histologicznych, które są zróżnicowane pod kątem złożoności struktur jak i poziomu powiększenia. Najczęściej używamy tkanki naczyniowej, tkanki mięśnia sercowego i tkanki ścięgna, ale nie są to jedyne typy tkanek użyte w testach.

Wszystkie przedstawione algorytmy są zaadaptowane do wymagań każdego z problemów. Wszystkie używają deskryptorów z momentami Zernike u podstaw, jednak pewne modyfikacje są konieczne do spełnienia wymagań poszczególnych problemów. Każde z rozwiązań jest przetestowane na zróżnicowanym zestawie danych. Wyniki końcowe potwierdzają wstępne założenia, a proponowane rozwiązanie może być wykorzystane jako narzędzie w tego typu problemach identyfikacyjnych. Wszystkie wnioski i wyniki są zobrazowane na odpowiednich rysunkach, bądź umieszczone w odpowiednich tabelach i podsumowaniach w rozprawie.

Contents

Chapter 1

Introduction

The main goal of our thesis is to introduce a new approach to using Zernike moments in problems of pattern recognition in microscope images. We also plan to broaden the scope of known problems of image analysis of tissue slides. Finally, we provide a viable solution to posed problems in the form of algorithms using the proposed methods.

Zernike moments have a history of use in various pattern recognition problems. Initially, they were widely used in the study of optical aberrations due to the disk nature of the Zernike moment itself. Since then, they were used mostly in shape-recognition problems. Newer publications cover updated use of Zernike moments in problems of more pattern-recognition variety, but their practical application is mostly limited to detection problems and binary classifications.

Many properties of Zernike moments make them a useful tool in image analysis. There is rotation invariance of the module of the moment and through some modifications we can also achieve other types of invariance like translation or scale invariance. There is also a general roubustness of the moments to take into the account. In our approach, we use Zernike moments in the form of a vector image descriptor. It becomes a basic tool in all algorithms presented in the thesis. Additionally, we introduced a brand new image descriptor using a modified form of Zernike moments, named accumulated Zernike moments. It is also a vector image descriptor, which contains accumulated Zernike moments instead of Zernike moments.

In our thesis, we plan to find new ways of application of Zernike moments in problems dealing with heavily textured images like tissue sections. Such assumptions put them in the category of complex microscope image analysis problems. Further in the work, we present a selection of problems and methods of their solution.

Microscope image analysis comes with many problems which often require custom-made methods of solution. Most publications focus on a single problem and present a method of solution designed for it. Finding alternative ways of solving such problems may sometime prove fruitless or not cost-efficient enough. The tried and tested approach remain segmentation and filtering algorithms used to extract certain features from images among their many uses like in the case of retrieving object data from CT or MRI scans. Neural networks are also a very popular method, used mostly in binary classification and detection problems, e.g. in detection of maligned mass like cancer cells in microscope images. In summary, methods of solution wholly depend on the data fromat of the expected output.

In our case, we expand on the scope of microscope image analysis of tissue slides and provide a new approach to some of the known problems.

1. We present a new take on the problem of sequencing of microscope slides. Here, we establish whether Zernike moments are capable of detecting slight changes between similar images.
2. Then, we explore Zernike moments and their application in problems of identification of tissue types in microscope images.
3. With further expansion into automatic classification of tissue types and detection of aberrations in collections of microscope images. It is important to note that we examine these problems in the context of multi-class classification.

All of this is to provide more accurate methods of tissue analysis in microscope images.

Another important part of this thesis is designing and implementing new algorithms to solve presented problems. Our main tool is a vector of Zernike moments, used in the form of an image descriptor. It provides us with a specific identifier of the image that also carries the information on some features of the image. Such image signatures allow us to identify particular samples in the set as well as find other samples with similar features, thus, making the descriptor a good classification tool. This is further expanded to detect samples which do not fit a certain standard. We also propose a more robust approach which we describe as accumulated Zernike moments. It is a shortened version of a Zernike moment descriptor constructed by accumulating the values of Zernike moments within a given order of the moment. Data sets of both types of descriptors are used to build a reference model for each type of tissue. It is a construct which serves as the point of reference for classification algorithms.

The focus of this thesis are problems which we can categorize first and foremost as pattern-recognition problems. Depending on the expected outcome we can divide them into three major categories: sequencing of microscope slides, identification of tissue types and detection of damage in tissue samples. An algorithms is designed to solve each type of problem. The descriptions for each algorithm are as follows:

1. Sequencing of microscope slides using optimizing functions to estimate the order of slides.
2. Identification of tissue types in microscope images which is solved in three different ways.
3. In the first case, we use Zernike moments and reference models, supported by machine learning algorithms (MLA) to identify tissue type in microscope images.
4. In the second case, we use a multi-classifier which combines properties of multiple MLAs and uses Zernike moments as input data.
5. In the third case, we calculate Zernike moments for randomly sampled data from high-resolution microscope images and use it in an accumulative classifier.
6. Finally, it is detection of damage and other aberrations in microscope images using Zernike moments, reference models and MLAs.

We use Zernike moment-based descriptors as the key component of the proposed algorithms. Such approach allows us for easier storage of data since Zernike moment descriptors take less volume compared to source images, thus, saving on space needed to store the data. The properties of Zernike moments make the descriptor rotation invariant, and in the case of tissue samples it can be further expanded to translation and scale invariance, too. Another adventage of this approach is its general roubustness and versatility. Zernike moments in the form of descriptors can be cross-applied to many types of image analysis problems. Since the descriptor is a stand-in for the original image, it also allows us to collect data of many images and build up profiles of various tissue types to use in the future.

Additionally, the proposed algorithms work on heavily textured images like human tissue.

In summary, in this thesis:

1. We explore and prove an alternate approach to Zernike moments. That is image descriptors in the form of vectors constructed out of Zernike moments.
2. We introduce accumulated Zernike moments which are modified version of Zernike moments composed out of accumulated values of the moments.

3. We expand the use of Zernike moments from the scope of shape recognition and pattern recognition to a more complex problem of identification of tissue types in microscope image slides. It is important to note that the approach works on heavily textured images of human tissue.

4. The vector form of the descriptor allows us to automatize the process of classification of types of tissue in microscope images.

5. To a certain extent, it allows us to reconstruct or at least optimize the sequences of tissue slides.

6. Moreover, Zernike moment descriptors prove to be robust enough and sensitive enough to differentiate between images in the same group of tissue. This allows us to use them in the process of automated detection of damage in microscope images.

The focus group of images for the thesis consists of microscope images of human tissue. Images of tissue samples come from various types of tissue (e.g. cardiac muscle tissue or tendon tissue) and in varying levels of magnitude which we can describe as medium (40X), large (100X) and extra-large (400X). Some preparations take form of subsequent tissue slides (e.g. vein slides). Histological sections are a very diverse group that depicts content structures built out of many specialized cells. A lot of these elements are seen in microscope images. However, despite these complex structures and many cursory similarities we can discern different patterns in those structures which characterize different tissue types like neurons (gray matter) or cardiac muscle tissue. Such collection of tissue slides forms a diverse database which serves as reliable and robust input data for the proposed approach.

In the next chapter, we present the concept of medical images as defined by source literature. We put special emphasis on microscope image section. Further, we highlight some popular problems of medical image analysis and most common methods of their solution. Finally, we bring up some examples of practical applications with relevant citations. In Chapter 3, we recall the official definitions of Zernike moments and polynomials. We also feature sections on properties of Zernike moments and the implementation of Zernike moments in discrete spaces. Both of those items are important if we want to use Zernike moments in digital image analysis at all. In Chapter 4, we introduce our approach to using Zernike moments in image descriptors. We present two methods of calculating a Zernike moment-based descriptor with potential application of such descriptors in problems of tissue identification.

Chapter 5 contains an exposition on discrete image representation and how it relates to the implementation of Zernike moments. Important aspect are the polar transformations of discrete spaces which are a big part of Zernike moment calculations. Moreover, we describe different methods of preprocessing an image for calculations. Finally, we describe how geometric transformation like rotation or translation fit into the concept of discrete image spaces and how such knowledge can be useful to Zernike moments.

In the following two chapters we present examples of practical applications of the proposed descriptor. These are the chapters that provide all necessary formulas, experiment setups and results with conclusions. The chapters divide the applications into the problems of image sequencing and the problems of image identification.

Chapter 6 includes the use of Zernike moments and edge histograms in the problem of sequencing of microscope image slides. We include the example of use of edge histograms to solve the problem and a comparison study with a Zernike moment-based descriptor. We also combine those two approaches to improve the outcome. Finally, we show the application of accumulated Zernike moments for a select few image series.

Chapter 7 covers the use of Zernike moments in the problems of image recognition type. We start by proving the scalability of Zernike moments and how it can be applied in further image analysis. Next, we focus on the problem of tissue recognition using the proposed Zernike moment-based descriptor with the support of MSE and neural networks to finalize the identification. We expand this approach to the problem of tissue recognition using random point samples from the tissue. In both of those cases, we can introduce some automatization of the process. Using the previously established pattern recognition algorithms, we can further expand the application to the detection of any images of tissue that do not match the pattern like images containing damaged tissue.

The final chapter contains the summary of the thesis with necessary comments and conclusions.

Chapter 2

Medical Images and Medical Image Registration

This chapter presents the concept of a *medical image* with heavy focus on its subcategory that is a microscope image. Additionally, it contains a brief overview of methods of medical image acquisition, the main problems of this branch of research as well as examples of application.

The chapter starts with the introduction to the subject of medical imaging: common definitions and practices, popular methods of image registration and selected examples of application. Further, we describe common problems that are the subject of research with some examples. Finally, we provide a more in depth description of properties and problems of microscope images that are the focus of this study.

2.1 Medical and Microscope Images

The term *medical image* describes a wide range of images that can differ both on the subject that they represent and the method of its acquisition. The process of acquiring a medical image is called medical imaging. It is a subcategory of biological imaging and refers strictly to techniques and processes that are used to create images of the human body for various clinical purposes such as medical procedures and diagnosis or medical science including the study of normal anatomy and function. Thus, the primary subject of the medical image is the human body [50].

Human body is an advanced organism that is composed of many types of different cells that build into tissues and subsequently into organs. The structure of the components depends on their purpose in the body. Parenchymal tissue of the lung (that is responsible for the oxygen exchange in respiratory system) has different structure and properties than myocardium tissue of the heart (that is responsible for the contraction of the heart) or gray matter of the brain. Any part of the human body can become the subject of a study.

Medical images provide visual representation of the interior of the human body and the function of organs and tissues. What data is contained in the image depends on the origin source and the method of acquisition. The diversity of the subject does not allow for a universal method of analysis. Therefore, most of the methods need to be customized for each case and depend on the properties of the subject and the requirements of the study [33], [53], [3].

There are many methods of medical image acquisition. Some of the most common include radiography, magnetic resonance imaging, medical ultrasonography or ultrasound, endoscopy, elastography, tactile imaging, thermography, medical photography, and nuclear medicine functional imaging techniques as positron emission tomography (PET) and single-photon emission computed tomography (SPECT). Each method is different and provides a specific set of data. Methods like medical photography provide a surface-level view of the human body while methods like MRI provide an in-depth look [69], [68].

The image of the same subject may look different depending on the selected method of acquisition. A PET and a MRI scan of the human brain will provide different information even when depicting the same subject. It allows to control the level of accuracy in the image for the given subject and the complexity of the resulted image. Because of the various methods of acquisition, there is no universal method of analysis for medial images. Each type of the image needs to be processed adequately. Therefore, it is important to know the subject before developing analysis tools since algorithms working on MRI scans may not work for PET scans and so on. Most problems in the fields of medical images requires custom-made methods of analysis [74], [106].

Biomedical tissues are a very diversified group that covers a wide variety of subjects. The structure of the tissue differs both on microscopic and macroscopic levels. It covers very complex and elaborate structures. Therefore, the scope of images can cover variety of different subjects from MRI scans of human brain and CT scan of abdomen to section images of lung tissue from electron microscopy. The accuracy of the acquisition method impacts the complexity of the image content. While radiography scans may provide a simple view on the subject, more advanced methods like PET or MRI scans return a more detailed image.

Medical images are used widely within healthcare for diagnosis, planning treatment, guiding treatment and monitoring disease progression. In many cases, multiple images are acquired from subjects at different times and with different imaging modalities. There is also a notion of comparing images obtained from patient cohorts in place of single subjects imagined multiple times [50], [128].

Medical imaging finds applications throughout many steps of the clinical track. It takes part in clinical diagnosis, treatment planning, consummation and evaluation of medical procedures. During medical proceedings multiple images are acquired. Many times information contained in two separate images can cover the same subject or it is of complementary nature, therefore it is desirable to develop methods that can integrate this information. The process falls under the term medical imaging [75].

Microscope images are a subcategory of biomedical images. The subject of microscope images usually consists of biological tissue. The study of the microscopic anatomy of biological tissue is called histology or microscopic anatomy [48]. The focus of this study can be organs (organology), cells (cytology) or tissues (histology). The branch that deals with diseases is called histopathology.

There are many points of study and many ways to analyze microscope images. In most cases, standard methods of signal processing are applied. Other means include statistical methods or artificial intelligence [77]. In recent years, microscope images become a subject to multimodal imaging and more often they are not only limited to 2D methods of imaging, but 3D models are also in use [15], [124].

2.2 Medical Image Registration Methods

The first step of processing information that is contained into two separate images is to bring those images into spatial alignment. This process is called registration. In the next step it is necessary to perform a fusion of information in order to display the data in the integrated format [78]. Any combination of image registration and imaging can benefit the medical assessment process.

An example of such approach can be present in radiotherapy treatment planning, where the integration of information form MRI and CT scans can prove very useful. While MRI provides a better tissue contrast and can be used for dealienation of tumor tissue, CT is necessary for accurate computation of the radiation dose [61], [54].

Medical image registration (MIR) is a crucial step in medical image processing. It is a discipline that combines medical imaging and image registration for the purpose of medical image analysis devoted to image registration. In the process of aligning two or more input images into a single image that provides more information. Registration part describes the optimal transformation that best aligns the objects of interests in the images. The input image that gets transformed (rotated, translated, scaled or deformed) is called the source image. The transformation happens in relation to a fixed input image that is referred to as the target image [33], [80].

A medical image can refer to various types of images that posses very different underlying physical principles and very different applications. It covers images varying from microscope images of histological sections to video images used for remote consultation.

Image registration is the process of aligning multiple images representing the same scene that were imagined at a different time or by a different set of modalities. The purpose behind such actions is caused by the possible movement of the object in the image, e.g. motion of the patient, cardiac motions, soft tissue deformations or structure growth [**?**], [35]. Acquiring multiple images with the same modality, but at the different time points serves to mitigate that. When images of the same object come from different modalities it is possible to combine them in registration to provide a broader picture of the object.

Information contained in a single image is usually not enough to form a proper diagnosis. When the information is obtained from a single modality, at different time-frames and from different angles it still needs to be integrated to be of sufficient use. Retrieving such information from multiple image datasets obtained from different types of modalities and at different time-frames is an even harder task [126].

MIR methods can be divided into distinct categories. According to [116], [75] we can derive nine separate categories. The criteria cover dimensionality, nature of registration basis and transformation, domain of the transformation, interaction, subject and object. Each of these categories can in turn be divided into each own subcategories. The ensemble of some subcategories is covered in

The **dimensionality** category describes transformation of coordinate system or between an image and physical space between the source image and the target image. The important distinction is for the number of spatial dimensions and the registration of time series. The number of dimensions depends on the structure of data that is processed. We can differentiate a few most commonly used combinations: 2D/2D, 2D/3D and 3D/3D registrations. The registration of two tomographic images is an example of the 3D/3D registration. Two separate slices of data from a tomographic image fall under the 2D/2D registration. The dimensionality of the image influences the volume of data and the time to process it making the 3D/3D registration more complex and time-consuming than the 2D/2D registration. The 2D/3D registration is somehow a separate category that is usually applied to the direct alignment of spatial data to projective data or the alignment a single tomographic slice to spatial data, e.g. a pre-operative CT image to an intra-operative X-ray image. Because of the usual field of application (operating theater and radiotherapy setting) the 2D/3D registration is time-constrained with focus on speed computation and optimization [93], [14], [47].

1. Dimensionality
    - Spatial dimensions
    - Time Series
2. Nature of registration basis
    - Extrinsic
    - Intrinsic
3. Nature of transformation
    - Rigid
    - Affine
    - Projective
    - Curved
4. Domain of the transformation
    - Globa
    - Local
5. Modalities involved
    - Mono-modal
    - Multimodal
    - Modality to Model
    - Modality to Patient
6. Optimization procedure
    - Direct
    - Search-oriented
7. Interaction
    - Interactive
    - Semi-Automatic
    - Fully automatic
8. Subject
    - Intra-subject
    - Inter-subject
    - Atlas
9. Object
    - Head
    - Thora
    - Abdomen
    - Pelvis
    - Limbs
    - Spine

Figure 2.1: Classification of medical image registration methods.

Time series is a subcategory that expands the dimensionality with the time parameter. Time series are usually used to register occurring changes in the image in time intervals, e.g. post-operative monitoring of healing (short intervals), monitoring of tumor growth (medium intervals) or monitoring of bone growth in children (long intervals).

The registration based on the **nature of registration basis** can be *extrinsic* or *intrinsic*. In the case of extrinsic registration, a foreign object is usually introduced to the imagined space. The object is meant to be easily detectable within the scope of a modality to allow fast and easy registration. However, the approach requires introducing external objects i.e. artificial markers or frames attached to patient's body in the pre-processing stage making the approach very intrusive. Because of the pre-processing means the method can be automated since the necessary parameters are known beforehand and need not be optimized during the image acquisition. The aim of this approach is to acquire more efficiency, accuracy and reliability by analysing corresponding features in the images.

Image information generated directly from the patient is intrinsic. It is a process where features and anatomical information from the patient's image are extracted and mapped accordingly. It is a very common approach and there are many methods of acquisition that rely on patient-generated image content. At its core the registration is performed through different geometric means such as points, curves or principle axes. It can be performed using landmarks that consist of a limited set of identified points in the image. Segmentation-based methods are another way to register and rely on the alignment of segmented binary structures like object surfaces. The registration can also be performed directly from the image gray values. Compared to extrinsic method, intrinsic methods are non-invasive. This group of methods is also considered flexible and reliable.

Interesting point to highlight is that image registration can be non-image based and is usually performed in the form of coordinate system calibration. Example of application cover ultrasound scans or registration of position of medical tools during an operation.

The **nature of transformation based** category of image registration is about mapping input image into the target image. It is performed using geometric transformations where one set of points from source image is mapped into a fixed target image using various transformation methods. This transformation can be performed on *rigid* or *non-rigid* coordinate systems. Standard geometric transformations like translation or rotation are considered rigid. In this transformation the shape of the image and angles and distances between points remain the same. Non-rigid transformation utilize more parameters. In affine transformation parallel lines are mapped onto parallel lines. This transformation allows for scaling, shearing, translation and rotation. Projective transformation takes place when lines are mapped onto lines. This type of registration is performed on geometric objects. When lines are mapped onto curves it is curved or elastic transformation. It is used in deformable registration. Geometric transformations can occur as singles or complex compositions of more than one. This type of registration is usually described with matrices, vectors and polynomials [47], [43].

The **domain of the transformation based** registration operates on the domain of the image. In this case the transformation is performed on the image's domain. The points from the domain of the source image are directly transformed into the domain of the target image. The purpose of this operation is to obtain more detailed and significant information compared to the initial data. When the transformation of points from one domain to another results in fractional points in another domain, the new value is assigned based on adjacent points in the image [79], [56]. In this type of registration the transformation can be performed on the entire image or only on parts of this image. The registration is *global* when the transformation is performed on the entire image and *local* when it is performed on the selected features of the image. Transformation on the local level affect local geometric features and influence the deformation in the region. In global transformation any change of any parameter affects the whole image.

Registration based on **interactions** is described by three levels of autonomy of registration: interactive, semi-automatic and automatic. In interactive registration the process is assisted by the user who in turn is aided by visual software. It is a process that is performed in several steps. It starts with obtaining image from a scanner (PET, MRI, etc.), in the next step the user selects a region of interest (ROI). Then, intra-operative images are obtained and registered to preparative image which allows for the dynamic localization and tracking of ROI. The semi-automatic registration covers two approaches: the user initializes the start of the algorithm, rejecting/accepting the proposed registration hypotheses or the user steers the process along. In the automatic registration, the user only needs to supply the registration algorithm with the image or some information on the acquisition method. The methods can be semi-automatic in selection of ROI. However, interested or similar regions from pre-operative and intra-operative images can be detected without user interaction.

In image registration that is based on **optimization procedures** the transformation between the source image and the target image is performed iteratively. The distance between the similarity of the target image and the source image is estimated with each step until the final registered image is obtained. The main factor is the repetitiveness in the process of optimization of the transformation parameters until the final image is acquired. The purpose of optimization is the maximization of the similarity and the minimization of cost between the source and the target image. The optimization utilizes a cost function that estimates the results of each iteration; the target is minimization of this function. The goal of optimization is to estimate and adjust the differences in parameters between the source and the target image, so the cost function has the smallest possible value. A similarity metric needs to be deployed to estimate the accuracy of the image mapping. There are two approaches to image registration with optimization procedures: computation of parameters and search for parameters. In the first approach the value of the parameters can be directly computed from the available data. In the second approach, the parameters need to be searched for, e.g. by finding an optimum of some function within the parameter space.

In image registration **modalities** are means of image acquisition. Depending on how many modalities are involved the registration is divided into monomodal and multimodal. Monomodal registration occurs when the mapping is performed for two or more images that come from single modality. When the images come from different types of modalities, e.g. PET and CT, it is multimodal registration. Depending on the way the acquisition is performed there is *modality to model* and *patient to modality* approach. In these approaches there's only one image and the other modality is the mathematical model or the patient themselves. All these types are used to describe the registration task that needs to be performed.

Registration based on **subject** describes the patient whose images are to be registered. This method can be divided into: *intra-subject*, *inter-subject* and *atlas*. This type of registration aims to gather data on multiple patients' anatomy for statistical, cross-referential, visualization and analysis purposes. In intra-subject registration all acquired images come from the same patient. In intra-subject registration two or more images come from two or more different patients or a patient and a model. Having similar anatomical images of different patients provides a referential image database that can aid in diagnosis and illness progress and tracking. Atlas registration refers to one image acquired from a patient while the other image is constructed from the image database of many subjects. This type of registration can be used for automatic detection or lesion localization.

Registration based **object** refers to the imaging areas of interest that in MIR apply to parts of human anatomy. It is a broad field of study that covers many venues. Major areas of interest are head, thorax, abdomen, pelvis and spine. Examples of more detailed object registration are images brain, eye or dental imagining for the head, e.g. kidney and liver for the stomach, e.g. arms and legs for the limbs or spine and vertebrae.

2.3 Applications of Medical Image Registration

Medical image registration plays an important role in medical image analysis. It provides distinct and essential information of the patient. It has many applications in diagnostics and in therapeutics [53]. Some general applications of medical image registration include fusion of anatomical images, intervention and treatment planning, computer-aided diagnosis and disease following-up [64], surgery simulation, atlas building and comparison or computational model building. Some of these applications are sought-after in radiation therapy [27], cancer detection [94], template atlases or image-guided surgery [59], [105], [58].

Medical image registration plays an important role is cancer detection. Most notably in cancer detection and in monitoring of cancer treatment [28]. In the beginning stages image registration is used as means to analyze the tissue and detect potential changes [21]. In the case of cancer detection, image registration is used to translate segmented ROI from one type of image to another, e.g. from the haematoxylin and eosin (H&E) image to the infrared (IR) [67]. The difficulties with the detection are caused by low contrast between the two types of tissue: normal and cancerous in MRI and CT images. In this case images obtained from PET and SPECT scans are more useful. This type of image registration can be enhanced by using image fusion where the data from two sources is combined [32]. Such approach can lead to easier detection and improve the accuracy of the diagnosis. Cancer detection with image registration is proved to be effective with prostate cancer, liver cancer, breast cancer and head and neck cancer [11], [76], [94].

Radiation therapy is a medical therapy that utilizes ionizing radiation. It is often used in oncology for cancer treatment or as a method to alleviate pain during the treatment of disseminated cancer, e.g. during metastasis. It allows for a controlled dose of radiation to target the tumor while minimizing the dose to the surrounding healthy tissues [98]. In radiation therapy image registration is used to detect and verify patient position as well as treatment planning and assessment. In this case it is rigid and deformable transformations. In the case of rigid transformation it is rotation and translation of object, e.g. for CT or MRI image registration when the position of the patient's body changed, but no anatomical changes occurred. When critical structures are close to the tumor, a slight positional error may also lead to inadvertent radiation of the normal organs [10]. The deformable transformation is applicable when anatomic changes in the body occur which is the case when tumor grows or shrinks, there is a weight loss or organ shape variation [120]. The main application of deformable transformation is automatic segmentation, dose accumulation, mathematical modeling and functional imaging. More in-depth look at the content of images is achieved through radiomic features that describe the structural heterogeneity of tissues that is useful in detecting tumors [96].

Atlas database of medical images is another application of medical image registration. It contains a wide array of images depicting human organs, tissues and other. Atlas database is an accumulation of multiple images that come from many patients. The subjects obtained from individuals can differ in shape and size. Therefore, it is necessary to design a model for medical images that accounts for this variability. Medical atlas provides a template for potential image analysis. Image registration is responsible for mapping images into the atlas as well as providing new content for the models [25]. It is a way of addressing the diversity and variability of the obtained images. Atlas can be used as tool for image analysis and its derivatives like evaluation and interpretation of data or for referencing [29], [52], [16].

Image registration plays vital role in image-guided surgery (IGS). In the process, the preoperative images are registered with intraoperative patient data. Image registration maps similar anatomical structures in the preoperative and intraoperative images. During the procedure images are obtained multiple time: to extract regions of interests (ROI), at different time frames or from multiple scanners. The task of the registration process is to improve the alignment between the obtained images [19], [60]. This approach improves the accuracy of the information and allows surgeons to make more informed decisions. This field of application requires is not as well-developed as others [59].

Some applications of biomedical images may not be medical. The use of medical images for identification and authentication of individuals is well documented [5], [121]. The most notable is their use in biometrics, e.g. in authenticaction using retinal recognition [23], [107] or even electricardiograms [102].

2.4 Issues of Medical Image Registration

Modern medical image registration boasts advanced data scanning devices and imaging techniques. However, they do not come without any challenges. Important factors are computational efficiency and acute registration techniques that can be achieved in clinically acceptable time-frame. Registration techniques applied in medical field should be reliable and robust and the detection of ROIs should provide atomicity. Using automatic detection of ROIs in registration, especially for multimodal registration can be laden with error [58].

It can be observed in the case of complex and high volume functional and structural images like PET-CT scans. Other difficulties arise from non-linear nature of images or the unavailability of sufficient features. Accurately estimating mutual information in subregions during automatic registration of ROIs shows high sensitivity to noise, especially when there is no sufficient statistical information to back it up. Complex nature and non-linear relationship between overlapping regions impact most registration techniques. Other impacting factors include intensity in-homogeneity, blurred-object-boundaries or presence of artifacts. Therefore, a lot of techniques still utilizes manual or pre-defined registration with parameters that turns out to be slow and time-consuming.

The most important goal of MIR is the best performance through accuracy of registration, computational efficiency and robustness and reliability. These factors are important, especially in sensitive applications of MIR like IGS where timely response with accurate alignment is always required [4]. Registration of medical images carry a lot of issues that need to be accounted for. Images are often affected by organ movement or noise and blur effects. Errors occurring in the images can be of actual or timely variety. The content/quality of images may suffer from intensity variations or missing data. Various types of errors are an indispensable part of the medical images. Therefore, robustness and consistency should be a priority and devised registration techniques should be able to handle small amount of changes happening in input images.

Medical images contain different characteristics and features that make correct alignment of those images difficult. Proper alignment of multiple features gets more difficult when we take into consideration the differences in spatial resolution that come with images obtained from multiple modalities. It is important that image registration works properly with different types of organ images [22], [92]. Apart from the problems with spatial resolution and differences in features, multimodal MIR brings the problems of pixel intensity that varies between images. The dependence between intensity values of corresponding pixels is more often not straightforward. In such cases mapping of single intensity value from one image to multiple values in corresponding images can become quite complex. Especially if we consider the potential absence of identifiable features in some images while present in another that can affect the accuracy of this estimation.

The goal of successful registration is the estimation of the optimal transformation between the source image and the target image. The effectiveness of the transformation is measured with a pre-defined similarity criterion. There are many ways of measuring this similarity. Among the popular ones are mutual information (MI), sum of square difference (SSD), correlation coefficient or peak signal-to-noise ratio (PSNR) [88]. Big concern for these measurements is the presence and the absence of objects between images. These outliers can affect the information provided by the mutual information measures [88]. Counter measures need to be employed to mitigate the impact of the outliers such as consistency tests [8], gradient-based asymmetric multifeature MI [112] intensity transformation, joint saliency map (JSM) & normalized gradients [88], [112] and graph-based multifeature MI [112]. It is important to enhance the robustness of available similarity measures towards outliers in further development of MIR.

Optimization methods help in the process of MIR. They are vital in accurate extraction of landmarks and searching of similarity measures (like calculating mutual information in sub-images). But optimization in MIR has its downside. Most notable is the decrease of registration accuracy for the sake of local maxima of similarity measure. It is very prominent in the case of the elastic transformation where these local maxima can lead to inaccurate extraction of landmarks [125]. Therefore, key aims of optimization methods are to avoid local maxima and improve similarity measures. Such approach can lead to improvement of optimization techniques.

Multi-modal registration is a difficult target for optimization since it can cause problems for the mapping of contrasting information from the sources [36]. It is the main source of difficulties for the process in image guided surgery (IGS), where the patient's organ needs to be scanned several times with different scanners for proper diagnosis [4]. Proper identification of the location and orientation of the patient with different imaging systems is a challenging task. The goal is to eliminate the differences in patient position and map corresponding information from different types of images.

There are many components in medical images that need to be taken into consideration like points, curves and landmarks. They are often necessary for accurate detection and alignment of the images. The goal of MIR is the detection of the corresponding parameters in the images and their proper alignment [24].

We can derive two models of image association: structural and functional. In structural association, the equivalent anatomical structures are mapped, while in functional association, the same functional regions are aligned. The most desired outcome for MIR is to detect maximum number of related parameters that would aid in accurate diagnosis. However, this approach decreases the efficiency of computation due to the high number of searched parameters. MIR methods that use rigid and affine transformations usually apply minimum number of parameters to achieve correspondence, e.g. [44]. This approach decreases the computation load and increases efficiency. In the case of non-rigid registration, a maximum number of parameters is used for correspondence. That in turn leads to slow in computation compared to more rigid registration. Other aspect of non-rigid registration is the asymmetry of transformation which can cause difficulties in mapping of the landmarks and points in corresponding regions of the images.

2.5 Microscope Image Registration

Microscope image registration is a branch of biomedical processing that focuses on the data obtained from a microscope.

The most commonly applied approaches to MIR are 2D and 3D imaging. In 2D imaging the focus is on acquisition of the most accurate depiction of the microscopic sample. There quite a few things to take into consideration like the brightness and contrast of the image, the level of noise and other aberrations in the image or the position and the angle of the sample in the image. In 3D imaging the focus is on the series of images that are set in a fixed position, but at different focal depths. This approach allows for digital 3D reconstruction of the original sample

Histological sections provide useful information for the diagnosis or the study of a pathology. The 3D reconstruction from serial sections may lead to numerous applications at both the microscopic and the macroscopic levels [82]. On the microscopic level it can provide a new and more accurate histological and cytological parameters, such as the tumoral angiogenis in oncology, the fibrosis development in hepatitis or the cellular distortions in prion diseases. On the macroscopic level, the 3D reconstruction study allows one to study objects that are too small to be accurately dissected and too large to be analyzed based only on the 2D slices. Having high resolution, 3D representations of cellular structures is an important factor structure function studies in all areas of cell biology [51]. Because of that automatic 3D registration of serial section microscopic images is an on-demand research venue as it allows for a detailed anatomical reconstruction of large biological bodies [119].

Although its wide application in clinical and research studies, histopathologic recognition remains a time-consuming and subjective process. The accuracy of the recognition comes with an inherent operator viability which limits the statistical confidence that we can assign to it [73].

There are many factors to take into consideration when it comes to the content of microscopic images. Objects in the images often have irregular shapes and their internal structure may change between regions of the image. The intensity of the color may differ in different regions of the image. There is also the possibility of rotation, translation or other geometric shift of the object of interest that can occur in the image. The image can be also reflected or flipped. The process of acquiring the data is imperfect and leads to geometrical and pixel intensity-based distortions in the images. Due to the macroscopic levels of magnification (less than 100) we can restrict the rigid registration of images.

Microscope image registration has many applications. Despite focusing only on the microscopic aspect of biomedical imaging it provides means of analysis and problem-solving for variety of research. Its impact on the medical area of study can be quite profound and in a lot of cases serves as the basis of analysis and diagnosis [31]. Some practical applications of the microscope image registration cover such problems as automatic 3D reconstruction of thick tissue blocks from 2D histological sections of mammary gland tissue [26], algorithm for non-rigid elastic registration of images of a serially sectioned whole rat brain [122], realignment of several datasets from rat brain and from a rhesus monkey's brain [82], the problem of aligning histological sections for 3D reconstruction and analysis of MRI of a rat brain [9].

In [30], spectroscopic imaging of tissue microarrays with statistical pattern recognition is used for histopathologic characterization of prostatic tissue. Image texture analysis using the gray level co-occurrence matrix to extract image features is a subject of [95].

Microscope image registration comes with its own serving of problems that impact them in terms of general image registration, but also in more specific ways connected to working on microscopic level. We can group more subject-related problems into a few categories that concern the complexity of histological sections, the process of acquisition and the problem of large data management.

The problems of complexity of histological section describe among many others such cases as the lack of 3D imaging methods to simultaneously capture the morphology of the object and the phenotype of its constituent cells [26], spare number of 3D imaging methods that compare to the higher level of specificity and higher resolution properties of 2D imaging methods [9] or the interrelationship between the three-dimensional structure of the object (macroarchitecture) and its cellular composition (microarchitecture).

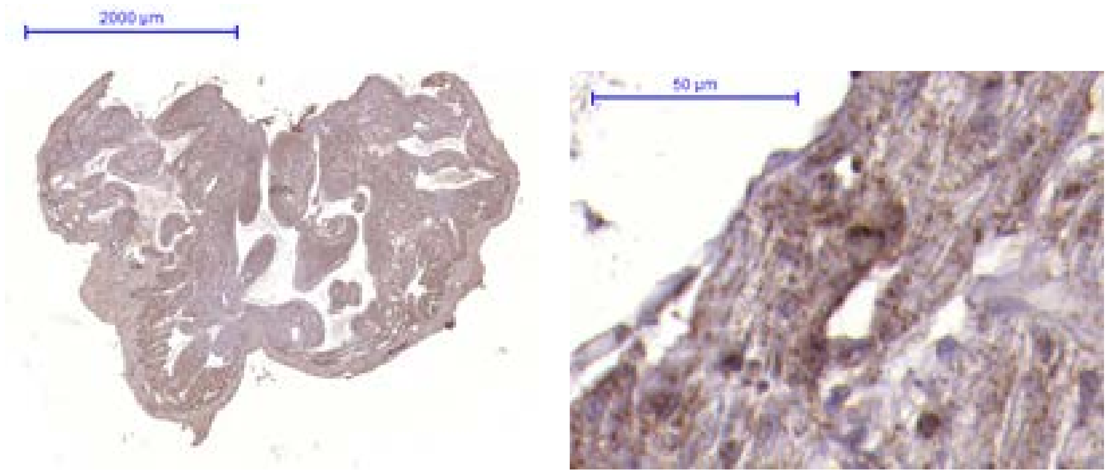

(a) Object at magnification 1X. (b) Object at magnification 40X.

Figure 2.2: One of the problems of microscope imaging is the lack of proper methods that both encapsulate the macro- and microlevel depictions of the tissue samples.

For the process of acquisition the problems center around the methodology and technologies that are used that can be inadequate to fully represent the subject at hand. The issue that come from this are that the acquisition of images is performed independently for each section which leads to a series of consecutive and unaligned images. There are deformations that come from the sectioning and the staining processes and artifacts like wrinkles, cracks and loss of tissue. All of these make a superposition of all consecutive slices looking fuzzy and coherent areas no longer fit [122]. Because of that if the data of the biologic material contains disturbances like distortions it must be processed adequately in order to visualize structures of interest.

A commonplace problem of microscope image registration is large data management. In some cases fully automatic registration of histological slices and reconstruction of 3D volume are necessary when manual registration using interactive alignment is non-reproducible and user dependent, and it cannot be used if the number of slices is large or when manual selection of the best reference slice (BRS) uses qualitative measures and ignores the image information content. In make optimum smooth 3D volume reconstruction not guaranteed [9]. Because of that it can be only suitable for small tissue volumes that do not cause data management and analysis issues.

Chapter 3

Zernike Polynomials and Moments

This chapter contains a brief introduction to Zernike moments and polynomials. We focus on their key properties that are useful to our thesis. The main core of the overview consists on the review of previous works on Zernike moments by [86], [62], [18], [38] and selected examples of their application [110], [72].

Zernike polynomials are a finite set of polynomials that are orthogonal in a continuous fashion within the unit disk. They were introduced by Fritz Zernike in 1934. They have many properties that found application in image registration and analysis. We can highlight their orthogonality [86] as well as a simple way of obtaining their rotational invariance [61].

This chapter is organized into three sections. The first part covers the major definitions and properties of Zernike polynomials. It is followed by a similar breakdown of Zernike moments and their relation to Zernike polynomials. Finally, we present a selected few examples of practical application of Zernike moments and polynomials.

3.1 Zernike and Radial Polynomials

A Zernike polynomial of order n and repetition m, denoted as V_{nm}, is defined as

$$V_{nm}(\rho, \theta) = R_{nm}(\rho) \exp{(jm\theta)}. \tag{3.1}$$

Here, ρ is the length of the vector from the origin to the point (x, y). θ is the angle between the vector and the x-axis. θ is the angle calculated counterclockwise from the x-axis. This set of dependencies can be summarized as follows

$$\begin{cases} \rho = \sqrt{x^2 + y^2} & \text{with } 0 \leq \rho \leq 1, \\ \theta = \tan^{-1}\left(\frac{y}{x}\right) & \text{with } 0 \leq \theta \leq 2\pi \quad \left(-\frac{\pi}{2} \leq \theta \leq \frac{\pi}{2} \text{ for tan}\right), \\ x = \rho \cos\theta, \\ y = \rho \sin(\theta). \end{cases} \tag{3.2}$$

A graphic depiction of these dependencies is shown in Figure 3.1

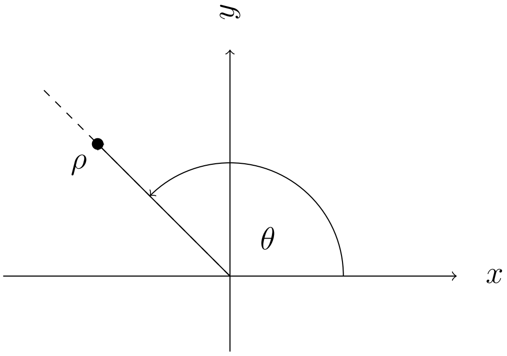

Figure 3.1: A coordinate set for a Zernike polynomial.

In 3.1 n is a positive integer and m is any integer that are subject to constraints

$$\begin{cases} |m| \leq n \\ (n-|m|)/2 \text{ is even.} \end{cases} \tag{3.3}$$

R_{nm} is a polynomial in ρ of degree n that contains no power of ρ lower than $|m|$. $R_{nm}(\rho)$ must be even when m is even and odd if m is odd [86]. The Zernike polynomial V_{nm} is split into the real part R_{nm} and the imaginary part $exp(jm\theta)$.

The explicit expression of a radial polynomial $R_{nm}(\rho)$ of order n is described with

$$R_{nm}(\rho) = \begin{cases} \sum_{s=0}^{(n-|m|)/2} (-1)^s \frac{(n-s)!}{s!(\frac{n+|m|}{2}-s)!(\frac{n-|m|}{2}-s)!} \rho^{n-2s} & \text{for } n-m \text{ even} \\ 0 \quad \text{for } n-m \text{ odd.} \end{cases} \tag{3.4}$$

The index s is a positive integer or zero. Since the absolute value of m is used in the equation, we can establish that

$$\begin{aligned} R_{nm}(\rho) &= R_{n(-m)}(\rho) \\ R_{nm}(-\rho) &= (-1)^m R_{nm}(\rho). \end{aligned} \tag{3.5}$$

The first few non-zero radial polynomials are showcased in Table 3.1.

The even and odd Zernike polynomials can be combined with sines and cosines instead of complex exponential functions. In such cases, we obtain

$$\begin{aligned} V_n^{-m} &= R_{nm}(\rho)\sin(m\theta) \\ V_{nm} &= R_{nm}(\rho)\cos(m\theta). \end{aligned} \tag{3.6}$$

$(\mathbf{n},\mathbf{m})$	$\mathbf{R_{nm}}(\rho)$
$(0,0)$	1
$(1,1)$	ρ
$(2,0)$	$2\rho^2-1$
$(2,2)$	ρ^2
$(3,1)$	$3\rho^3-2\rho$
$(3,3)$	ρ^3
$(4,0)$	$6\rho^4-6\rho^2+1$
$(4,2)$	$4\rho^4-3\rho^2$
$(4,4)$	ρ^4

Table 3.1: The first few non-zero radial polynomials $R_{nm}(\rho)$ (from [18]).

3.1.1 Properties of Zernike Polynomials

Among the important properties of Zernike polynomials are their orthogonality on the unit disk, simple rotation invariance and invariance in form for each pair of (n, m) [86].

The orthogonality of Zernike polynomials V_{nm} relies on the orthogonality of the radial polynomials $R_{nm}(\rho)$. That property for $R_{nm}(\rho)$ is expressed as

$$\int_0^1 R_{nm}(\rho)R_{n'm}(\rho)\rho\ d\rho = \frac{1}{2(n+1)}\delta_{nn'}, \tag{3.7}$$

where $R_{nm}(1) = 1$. In this case the orthogonality of a Zernike polynomial V_{nm} presents as

$$\int_0^{2\pi}\int_0^1 V^*_{nm}(\rho,\theta)V_{n'm'}(\rho\theta)\rho\ d\rho d\theta = \frac{\pi}{n+1}\delta_{nn'}\delta_{mm'}, \tag{3.8}$$

where δ_{ab} is the Kronecker delta that is 1 when $a = b$ and 0 otherwise.

Additionally, Zernike polynomials have simple rotational symmetry properties [38]. This means that the form of the polynomial does not change after rotating the coordinate system by an angle. For this, the polynomial is expressed as a product of the radial term $R(\rho)$ and the function of angle $A(\theta)$

$$R(\rho)A(\theta), \tag{3.9}$$

where $A(\theta)$ is a continuous cyclic function that repeats itself every 2π. Thus, rotating the coordinate system by the angle $\alpha \in [0; 2\pi]$ does not change the polynomial's form because

$$A(\theta+\alpha) = A(\theta)A(\alpha) \quad \text{where } A(\theta) = \exp(\pm im\theta). \tag{3.10}$$

A Zernike term is a single number or described with parameters n and m that are positive or zero values. For symmetry with respect to point reflection at the center of coordinates this translates to

$$V_{nm}(\rho,\theta) = (-1)^m V_{nm}(\rho,\theta+\alpha). \tag{3.11}$$

Other type of symmetry occurs with respect to the reflection along the x-axis [CITATION]. It is the result of the constituent trigonometric functions that are used in Zernike polynomials. That property is marked as

$$\begin{aligned} V_{nm}(\rho,\theta) &= V_{nm}(\rho,-\theta) \quad \text{for } m \geq 0, \\ V_{nm}(\rho,\theta) &= -V_{nm}(\rho,-\theta) \quad \text{for } m < 0. \end{aligned} \tag{3.12}$$

The radial polynomials $R(\rho)$ are even when m is even and odd if m is odd. The radial function must be a polynomial in ρ of the polynomial's degree n and contain no power of ρ less than m. Based on order n or m that dependency can be expressed as

$$R_{nm} = (-1)^n R_{nm}(-\rho) = (-1)^m R_{nm}(-\rho). \tag{3.13}$$

The radial polynomials can be derived as a case of Jacobi polynomials [86].

3.2 Zernike Moments

Zernike moments are a type of orthogonal complex moments. The kernel of the moment is composed of a set of Zernike complete orthogonal polynomials that are defined over the interior of the unit disk. A two-dimensional Zernike moment A_{nm} of order n and repetition m is defined as

$$A_{nm} = \frac{n+1}{\pi} \int\int_D f(x,y) V^*_{nm}(x,y)\, dx dy, \tag{3.14}$$

Here, $f(x,y)$ is the continuous function and $V^*_{nm}(x,y)$ is a complex conjugate of Zernike polynomial $V_{nm}(x,y)$. The disciple D for the unit disk is defined as

$$D = \{(x,y) : x^2 + y^2 \leq 1\}. \tag{3.15}$$

The parameters n and m are both integers where m is a complete number (positive or negative) that falls under the set of conditions that $n - |m|$ is even and $|m| \leq n$ from (3.3).

The Zernike moment's definition using polar coordinates and the coordinate transformation from the Zernike polynomial's formula (3.1) takes the following form

$$A_{nm} = \frac{n+1}{\pi} \int_0^{2\pi} \int_0^1 \widetilde{f}(\rho,\theta) R_{nm}(\rho) \exp(-jm\theta) \rho \; d\rho d\theta, \tag{3.16}$$

where $\widetilde{f}(\rho,\theta) = f(\rho\cos\theta, \rho\sin\theta)$. If we make a few additional assumptions where

- the point of origin of $f(x,y)$ lays in the center of the image,
- the area boundary of $f(x,y)$ is removed from the center symmetrically in every direction θ along the x- and y-axis
- $f(\rho\cos\theta, \rho\sin\theta)$ is an even function of θ,

then the equation (3.16) transforms into [86]

$$A_{nm} = \int_0^{2\pi}\int_0^1 \widetilde{f}(\rho,\theta)R_{nm}(\rho)\cos(m\theta)\rho\ d\rho d\theta. \tag{3.17}$$

In this case the Zernike moment A_{nm} is a real number.

Order	**Moments**	**No. of moments**
1	A_{11}	1
2	A_{20}, A_{22}	2
3	A_{31}, A_{33}	2
4	A_{40}, A_{42}, A_{44}	3
5	A_{51}, A_{53}, A_{55}	3
6	A_{60}, A_{62}, A_{64}, A_{66}	4
7	A_{71}, A_{73}, A_{75}, A_{77}	4
8	A_{80}, A_{82}, A_{84}, A_{86}, A_{88}	5
9	A_{91}, A_{93}, A_{95}, A_{97}, A_{99}	5
10	$A_{10,0}$, $A_{10,2}$, $A_{10,4}$, $A_{10,6}$, $A_{10,8}$, $A_{10,10}$	6

Table 3.2: Zernike moments A_{nm} and their corresponding number of features in n-th order listed from $n = 1$ to $n = 10$.

3.2.1 Properties of Zernike Moments

Zernike moments have plenty of properties that find application in many disciples. However, this section focuses on the properties that make them useful in image description.

One of the key properties of the Zernike moments is that they are rotation invariant under proper conditions and in some cases they can also be made translation and scale invariant. Rotation invariance is obtained through the magnitude of the Zernike moment. In such case, let us have the rotated image $f^{Rot}(\rho,\theta)$ that is rotated by the angle α by the original image $f(\rho,\theta)$. That relationship can be summarized as

$$f^{Rot}(\rho,\theta) = f(\rho,\theta-\alpha). \tag{3.18}$$

After inserting the image $f^{Rot}(\rho, \theta)$ into Equation 3.16 that equation becomes

$$A_{nm}^{Rot} = \frac{n+1}{\pi} \int_0^{2\pi} \int_0^1 f(\rho, \theta - \alpha) R_{nm}(\rho) \exp(-jm\theta) \rho d\rho d\theta \tag{3.19}$$

and after substituting $\theta' = \theta - \alpha$ it goes like this

$$\begin{aligned} A_{nm}^{Rot} &= \frac{n+1}{\pi} \int_0^{2\pi} \int_0^1 f(\rho, \theta') R_{nm}(\rho) \exp(-jm(\theta' + \alpha)) \rho d\rho d\theta \\ &= \left[\frac{n+1}{\pi} \int_0^{2\pi} \int_0^1 f(\rho, \theta') R_{nm}(\rho) \exp(-jm(\theta')) \rho d\rho d\theta \right] \cdot \exp(-jm(\alpha)) \\ &= A_{nm} \exp(-jm(\alpha)). \end{aligned} \tag{3.20}$$

Thus, rotation invariance of the magnitude of a Zernike moment is

$$\begin{aligned} |A_{nm}^{Rot}| &= |A_{nm} \exp(-jm(\alpha))| \\ &= |A_{nm}(\cos(m(\alpha)) - j\sin(m(\alpha)))| \\ &= |A_{nm}| \end{aligned} \tag{3.21}$$

In the case of reflection in the image function, defined as $f(-x, -y)$ in accordance with the original image function $f(x, y)$ defined on the unit disk, the invariance presents as

$$A_{nm}^{Refl} = A_{nm}^{*} \exp(-j2n\beta), \tag{3.22}$$

where A_{nm}^{*} is the moment's conjugate and the image is reflected across a line rotated by the angle β ([86]).

Scale and translation invariance requires some form of image normalization before being subjected to Zernike moments [62]. Translation invariance is achieved by moving the center of the image from its origin point to the center of the mass of the image. For this purpose, we can refer to geometric moments. A geometric moment $M_{pq}^{(f)}$ of image $f(x, y)$, using a standard power basis, has the following formula

$$M_{pq} = \int_{-\infty}^{\infty} \int_{-\infty}^{\infty} x^p y^q f(x, y) dx dy, \tag{3.23}$$

where p, q are non-negative integers that define the order of the moment as $r = p + q$. Using the definition from (3.23), we can derive some moments of low orders [34]. Thus, M_{00} is a total mass of the image, moments M_{01} and M_{10} define the center of gravity or centroid of the image. We calculate the center of the mass of the image using a set of moments (M_{00}, M_{01}, M_{10}) [86]

$$(x_c, y_c) = \left(\frac{M_{10}}{M_{00}}, \frac{M_{01}}{M_{00}} \right). \tag{3.24}$$

We can describe the translation by the center of the mass of the image as

$$f^{Transl}(x,y) = f(x - x_c, y - y_c), \tag{3.25}$$

where (x_c, y_c) is the calculated center of mass of the original image $f(x,y)$ from (3.24).

Scale invariance requires some alternations of the content of images. In this approach, the area of the object in the image needs to be stretched to reach a common quota. The measure of this expansion is the predetermined value b and the point of reference for the object's area is the geometric moment M_{00}. The whole dependency can be summarized as

$$f^{Sc}(x,y) = f\left(\frac{x}{b'}, \frac{y}{b'}\right), \quad \text{where } b' = \sqrt{\frac{b}{M_{00}}}. \tag{3.26}$$

Since both scale and translation invariance occur before calculating Zernike moments and involve image transformation in Cartesian coordinates they can be combined into one dependency as follows

$$f^{Sc}(x,y) \otimes f^{Transl}(x,y) = f\left(\frac{x}{b'} - x_c, \frac{y}{b'} - y_c\right). \tag{3.27}$$

The discrete implementation of the images may require interpolation of the missing pixel data for the scaled and translated images.

Zernike moments' orthogonality allows for their invariants to be calculated independently to high orders without the need to recalculate low order invariants.

3.2.2 Discrete Zernike Moments

As in the case of Zernike polynomials, Zernike moments are described over a continuous space as well. Therefore, discrete Zernike moments need to be approximated to achieve the desired output. In such case Equation 3.14 for a discrete image takes up the form of

$$\hat{A}_{nm} = \frac{n+1}{\pi} \sum_x \sum_y f(x,y) V^*_{nm}(x,y), \tag{3.28}$$

In order to calculate the Zernike moment the image $f(x,y)$ needs to be mapped to the unit disk using polar coordinates. The center of the image should be positioned in the origin of the unit disk. Any points of the image that do not fit within the disk are omitted from the calculations. The dependencies between the Cartesian coordinates (x,y) and the polar coordinates (ρ, θ) are already summarized in Equation 3.2.

Because Zernike polynomials are orthogonal only in a continuous fashion, applying them over a discrete set of data points in general leads to the loss of orthogonality. The loss occurs due to the discretization of the integral area and the subsequent loss of continuity that leaves the equation (3.8) unfulfilled. In such case $\hat{A}_{nm} \neq A_{nm}$ [86].

3.2.3 Image Reconstruction with Discrete Zernike Moments

The idea of image reconstruction using orthogonal moments appears in [110]. The general idea is that knowing all orthogonal moments up to a given order n_{max} of a Cartesian function $f(x, y)$ allows to reconstruct a discrete function $f(\hat{x}, y)$ using that discrete function's moments that match those of the original function $f(x, y)$ up to order n_{max}. The accuracy of the reconstruction improves as n_{max} approaches infinity.

Image reconstruction with Zernike moments is mentioned in [62]. It relies on multiplying every moment by its basis function and then summing the products together. Using radial coordinates the reconstruction is described as

$$\hat{f}(\rho, \theta) = \sum_{n=0}^{n_{max}} \sum_{m} \frac{n+1}{\pi} A_{nm} V_{nm}(\rho, \theta) \tag{3.29}$$

where $\hat{f}(\rho, \theta)$ is the reconstructed image and n_{max} is the max value of order n used in reconstruction. Parameters n and m are still subjected to constraints $n - |m|$ is even and $|m| \leq n$ from 3.3. Examples of reconstructed images are in Figures 3.2 and 3.3. Since Zernike moments are complex values, the reconstructed image has both real and imaginary values. How the number of Zernike moments impacts the process of reconstruction is presented more broadly in [72].

3.3 Some Practical Examples of Application of Zernike Moments and Polynomials

In [49] the Zernike and Orthogonal Fourier-Mellon (OFM) moments are used in representation and recognition of printed digits. The moments were chosen due to their invariance properties with scale, translation and rotation. The images used were grayscale images.

Zernike polynomials are an important component in the expansion of a wavefront function for optical systems with circular pupils [109]. It is the reason why they are applied in various optics branches, eg. for detection of optical aberrations [20], [38], [13]. Table 3.3 shows some application of Zernike polynomials in mod-

(a) $f(\rho, \theta)$ (b) $Re\{\hat{f}(\rho, \theta)\}$ (c) $|\hat{f}(\rho, \theta)|$

Figure 3.2: An example of a reconstruction of the image from a set of discrete Zernike moments. We drop the imaginary part of the reconstructed image from the display.

(a) $f(\rho, \theta)$ (b) $Re\{\hat{f}(\rho, \theta)\}$ (c) $|\hat{f}(\rho, \theta)|$

Figure 3.3: An example of a reconstruction of the image from a set of discrete Zernike moments. We drop the imaginary part of the reconstructed image from the display.

eling of optical aberrations. Here, ρ describes the normalized pupil radius with $0 \leq \rho \leq 1$ and θ is the azimuthal angle around pupil with $0 \leq \theta \leq 2\pi$.

n	**m**	$\mathbf{Z}_{\#}$	**Polynomial**	**Optical aberration**
0	0	Z_0	1	Piston
1	-1	Z_1	$2\rho \sin\theta$	Vertical Tilt
1	1	Z_2	$2\rho \cos\theta$	Horizontal Tilt
2	-2	Z_3	$\sqrt{6}\rho^2 \sin(2\theta)$	Oblique astigmatism
2	0	Z_4	$\sqrt{3}(2\rho^2 - 1)$	Defocus
2	2	Z_5	$\sqrt{6}\rho^2 \cos(2\theta)$	Vertical/Hor. Primary Astigmatism
3	-3	Z_6	$\sqrt{8}\rho^3 \sin(3\theta)$	Vertical trefoil
3	-1	Z_7	$\sqrt{8}(3\rho^2 - 2)\rho \sin(\theta)$	Vertical coma
3	1	Z_8	$\sqrt{8}(3\rho^2 - 2)\rho \cos(\theta)$	Horizontal coma
3	3	Z_9	$\sqrt{8}\rho^3 \cos(3\theta)$	Oblique trefoil

Table 3.3: Example of application of Zernike polynomials in modeling and detecting of optical aberrations. The indexing of $Z_{\#}$ follows OSA/ANSI standard.

The reconstruction of an image from Zernike moments is a viable application [83]. The reconstruction can also serve as a feature extractor [45], [66], [72] or in some cases to detect ROIs related to the objective [89]. Examples of retrieval and reconstruction of objects from images with the use of Zernike moments can be seen in Figures 3.2 and 3.3. Other common applications of Zernike moments include such problems as classification [7], [40], [108] or recognition [41], [101].

Chapter 4

Proposed Method of Image Identification and Classification with Zernike Moments

In this chapter, we introduce our approach to Zernike moment-based image descriptors. We propose two methods of constructing an image descriptor using Zernike moments. Additionally, we expand the approach to provide a model of a class prototype that finds application in classification and identification problems related to image analysis.

The chapter contains descriptions of a Zernike moment-based image descriptor and its shortened variant with accumulated Zernike moments. It includes definitions, properties and potential applications of the descriptors. The final section covers a construction of a class prototype that utilizes Zernike moment-based descriptors and its application to classification and similar problems. This section presents the proposed approach to image description using Zernike moments. The basic premise is to use sequences of Zernike moments as image descriptors.

Image descriptor is a set of parameters that can be used to describe an image. The most common approach to describe the image is to use a two-dimensional or - in the case of RGB images - a three-dimensional numeric matrix. Each cell contains a numeric value of a pixel in the image that emulates the actual intensity of the source image in this point. Such descriptor while provide a good visual representation of the image in the digital space do not lead to easy identification in numerical computations. Therefore, developing alternative methods of image description is often necessary. An example of alternative approach may be a label or a pattern that describes or identifies some aspect of the image. Having a set of parameters that identify various image features allows to build an easily-indefinable representation of that image. However, such descriptors contain a limited amount of information that provides a limited or very specialized scope of application.

A well-tailored image descriptor should contain enough details and information to unambiguously identify the image for the given scope of the identification problem.

4.1 Zernike Moments in Image Descriptors

Zernike moments have a history of application in image identification and analysis [62], [72], [70], [101]. Expanding on this topic, we propose an approach to this problem that relies on building sequences of Zernike moments. This ordered sequence, in a form of a vector, serves as an image descriptor that can unambiguously identify the image. Additionally, the method is very flexible and allows for customization in terms of the precision of description as well as the selection of features.

An image can be described with any sequence of Zernike moments. However, the number and the type of Zernike moments in the sequence decide on how accurate of a representation it is and what features of the image are highlighted. The accuracy of representation raises with the number of moments used in the creation of the sequence. A detailed sequence also allows for a fairly accurate reconstruction of the original image 3.29.

However, the number of the moments in the sequence is often limited by the computational parameters of the hardware which is used in calculation. The formulas of Zernike moments of higher orders become more elaborate and require more sophisticated implementation and processing power. For these reasons, it is necessary to truncate the number of Zernike moments to a finite set that can be implemented. However, the data reduction lowers the accuracy of the image description and, depending on the number of Zernike moments in use, a reliable reconstruction of the original image may no longer be possible [71].

However, such approach brings a lot of flexibility to the descriptor. First and foremost, it allows us to define a preferred level of accuracy for the descriptor by selecting the number of Zernike moments to use in its construction. Precise control over the type and the number of Zernike moments in the descriptor allows us also to tailor it to perform specific tasks like feature extraction or cutting off unwanted features for a class of images [45], [63], [108], [90].

Zernike moments have many properties that make them useful for various pattern recognition problems from identification and feature extraction of script languages [90] to recognition of human faces [45]. One of the valuable characteristics of Zernike moments that stems from their orthogonality is that subsequent moments do not carry duplicated information [86]. This property makes the information in each moment unique. Moreover, there is no redundant information passed between the moments which greatly reduces the amount of information to process during calculations. Additionally, Zernike moments are particularly robust to image distortions and noise [86].

Moreover, it allows us for a better control and management of information in the descriptor by choosing which moments to use. Since a Zernike moment can be used to describe or extract a certain feature from an image [109], [20], it is possible to tailor the descriptor to perform a desired function using selected moments. We can obtain rotation invariance of a descriptor by using the module of a Zernike moment as presented in chapter 3.1.1.

The proposed image descriptor is an ordered sequence of Zernike moments. The number of moments in the sequence as well as their lower and upper range are selectable parameters that can be adjusted to serve a specific purpose. The order of the sequence is important to properly compare descriptors of two different images as subsequent values are not interchangeable.

The basic element of the sequence is a Zernike moment. In our model, a Zernike moment of order n and repetition m is denoted as A_{nm}. The image descriptor is build out of many Zernike moments arranged into a sequence. Let us denote a Zernike moment descriptor as D and define it as

$$D = \{A_{00}, A_{11}, A_{1(-1)}, \ldots, A_{n_{max}m_{max}}, A_{n_{max}(m_{max})}\}. \tag{4.1}$$

Here, n_{max} is the maximum order of a Zernike moment in the sequence and m_{max} is the maximum corresponding repetition value. This model can be easily transformed into an ordered sequence by using a row or column vector in its place:

$$D = \left[\begin{array}{cccccc} A_{00} & A_{11} & A_{1(-1)} & A_{20} & \cdots & A_{n_{max}m_{max}} & A_{n_{max}(-m_{max})} \end{array}\right], \tag{4.2}$$

where n_{max} and m_{max} have the same constraints as in Equation (4.1).

If we use the modules of Zernike moments in the descriptor, we can make the descriptor rotation invariant. This property is mentioned in chapter 3.1.1 in Equation (3.21). In the module of a Zernike moment, $|m| = |-m|$ thus $|A_{nm}| = |A_{n(-m)}|$. This way we can reduce the size of the image descriptor by removing the modules of moments with repetition $-m$ since they contain the same information as the modules of moments with repetition m. Let us denote the repetition invariant module of a Zernike moment as A^R_{nm}

$$A^R_{nm} = |A_{nm}| = |A_{n(-m)}|. \tag{4.3}$$

The new form of a rotation invariant descriptor D^R is as follows

$$D^R = \left[A^R_{00}\ A^R_{11}\ A^R_{20}\ \cdots\ A^R_{n_{max}m_{max}}\right]. \tag{4.4}$$

4.2 Accumulated Zernike Moments in Image Descriptors

In this section we propose another way of using Zernike moments in image descriptors. This approach relies on what we describes as accumulated Zernike moments. In this form, the accumulated Zernike moment is the sum of all Zernike moments of a given order over the repetition.

The biggest benefit of such representation is that it greatly reduces the number of vector components in the image descriptor. However, this approach registers a slight dip in accuracy and looses us the option of image reconstruction from Zernike moments [83], [86]. This is caused by the merge of information in accumulated moments that cannot be reversed and therefore we do not have access to Zernike moments that are necessary for image reconstruction.

However, these new properties allows us to expand the use of the descriptor toward encoding. The accumulated Zernike moments allow us for an unambiguous identification of the image while keeping the source image unobtainable. In some works, Zernike moments has been used as a watermark feature [63].

Despite the reduction of the amount of information in the image descriptor, the aim of the method is to retain a similar level of accuracy for image identification as in the case of the previous descriptor D, while reducing the size of the descriptor.

In this approach, the image descriptor is also a vector. However, the base component is now the sum of Zernike moments of a given order n over the repetition m. We call this form an accumulated Zernike moment. In calculations, we iterate through the repetition part m of the Zernike moment, accumulating the value in each step. The easiest way to obtain the accumulated Zernike moment A_n is to sum all relevant Zernike moments A_{nm} of the same order n. This procedure is summarized by the formula

$$A_n = \sum_{i=m_{min}}^{m_{max}} A_{ni}. \tag{4.5}$$

Since Zernike moments are complex, we can expect complex values in this form as well. We assume that the original properties of Zernike moments carry over to accumulated Zernike moments. Taking all the changes into the account, we can formulate a new descriptor $\hat{D}$ as follows

$$\hat{D} = [\ A_0\ A_1\ A_2\ \cdots\ A_{n_{max}}\ ]\,. \tag{4.6}$$

In order to acquire a rotation invariant descriptor from $\hat{D}$, we use modules of accumulated Zernike moments $|A_n|$. Because of this, we use only Zernike moments with $m \geq 0$ to calculate A_n. The properties of modules of Zernike moments from Equation (4.3) allow us to drop Zernike moments with $m < 0$ preemptively. The rotation invariant descriptor $\hat{D}^R$ is as follows

$$\hat{D}^R = [\ |A_0|\ |A_1|\ |A_2|\ \cdots\ |A_{n_{max}}|\ ]\,. \tag{4.7}$$

There are two methods of calculating accumulated Zernike moments. In the first method, we calculate all required Zernike moments A_{nm}, then, we add them up as proposed in Equation (4.5). The downside to this approach is that it requires multiple prior computations to obtain all necessary Zernike moments A_{nm} before we can obtain A_n.

The second method is to determine the proper mathematical formula for the accumulated Zernike moment A_n that can be used to directly compute the accumulated moment's value. For this, we start with the equation of a discrete Zernike moment from Equation (3.28) for A_{ni} in Equation (4.5). For the radial polynomial R_{nm} from Equation (3.4) and (3.1) we refer to [17] that provides equations of radial polynomials for subsequent Zernike polynomials. The equation for accumulated Zernike moment A_n is a shortened form of the sum of all subsequent Zernike moments A_{nm}.

The advantage of this approach is that it does not require prior computation of moments from us and that the value of the accumulated moment is calculated with a single directive. The major difficulty of this approach is that we need to find the equation for each accumulated Zernike moment we want to include in the descriptor.

Accumulated Zernike moments deliver a new method of image description. In this form, they retain most of the properties of Zernike moments like the rotation invariance of the module of the moment. They also allow us to unambiguously identify the original image. However, accumulating Zernike moments does not allow us to reconstruct the original image from moments as is the case for Zernike moments. However, these properties make accumulated Zernike moments a viable data encoder that carries enough information to identify the source image, but not enough data to retrieve that image, making it unreadable to third parties.

4.3 Zernike Moment-based Image Descriptors in Classification and Similar Problems

Image descriptors D and $\hat{D}$ can be used on a wider scope as descriptors for classes of images. The basic premise is that images of similar objects have similar values of Zernike moments. Since different images within the same class can have some variations in their appearance, we can expect some differences in the values of Zernike moments as well. However, the presence of those differences should not cause the value of Zernike moments to diverge too much from the general pattern.

Therefore, using descriptor D as a template we can create a more generalized descriptor for the entire class.

Let us name this generalized descriptor of a class as a class prototype C. We build the class prototype C using descriptors of images from the given class as building blocks. The strategy of generating the class prototype can be a simple average of descriptors of every image or a more elaborated weight system. In order to get a reliable class prototype, it is important to use an image database that contains a varied selection of images of the given class. Using the most diverse database helps create a robust class prototype that reflects the characteristics of the class. The class prototype relies primly on the notion that images of the same class share similar values of Zernike moments. This property allows us to create a generalized pattern for the image descriptor that can serve as a classification pattern for this class of images.

Since our thesis covers two types of image descriptors using Zernike moments, denoted D for a vector with the modules of Zernike moments (Equation (4.2)) and $\hat{D}$ for a vector with the modules of accumulated Zernike moments (Equation (4.6)), the class prototypes are referred to as C and $\hat{C}$ respectively. In our thesis, we foremost rely on descriptors with accumulated Zernike moments $\hat{D}$.

The class prototype C is built using image descriptors with Zernike moments D. It is calculated across a set of images of the same class. The number of images used in the construction of the class prototype is denoted with K. The equation for C is as follows

$$C = \left[\bar{A}_{11}, \bar{A}_{20}, \ldots, \bar{A}_{n_{max}m_{max}}\right], \tag{4.8}$$

where $\bar{A}_{nm}$ is an average of modules of Zernike moments for K number of descriptors

$$\bar{A}_{nm} = \frac{1}{K} \sum_{k=1}^{K} A_{nm}^{(k)}. \tag{4.9}$$

We use the modules of Zernike moments here to make the class prototype rotation invariant. This property is previously mentioned in Equation (4.3) and is used in descriptor from Equation (4.4) to make it rotation invariant as well.

The class prototype $\hat{C}$ is built the same way as C, but uses descriptor $\hat{D}$ with the modules of accumulated Zernike moments as its building blocks. The equation for $\hat{C}$ is

$$\hat{C} = \left[\bar{A}_1, \bar{A}_2, \ldots, \bar{A}_{n_{max}}\right]. \tag{4.10}$$

Here, $\bar{A}_i$ is an average value of modules of accumulated Zernike moments for the i-th component of the image descriptor $\hat{D}$ (Equation (4.7)):

$$\bar{A}_i = \frac{1}{K} \sum_{k=1}^{K} A_i^{(k)}, \tag{4.11}$$

where $A_i^{(k)}$ is the i-th component of the descriptor vector $\hat{D}$ of (k)-th image and K is the size of the image set that is used to calculate the class prototype.

The class prototype $\hat{C}$ is a vector of the same size as the image descriptor $\hat{D}$. In our approach, we build $\hat{C}$ by calculating the average value for each subsequent components of $\hat{D}$ using sample images from the class database. Taking into consideration the slight variations between the values of the descriptors of different images that can occur, we need to include some deviation margin for the generalized pattern. Therefore, we additionally define the acceptable upper and lower margin of values for every component of the vector $\hat{C}$. This range defines the limits to the acceptable deviation of value for the given component of the descriptor. The exact range limits depend on the standard deviation value of the elements of $\hat{D}$ and the selected multiplication coefficient. This addition makes the class prototype more robust.

The role of the deviation margin is to set a limit boundary that allows us to classify the image as belonging to the class. Images that have similar values of $\hat{D}$, but do not fall into deviation bounds are discarded. As in the case of the descriptor $\hat{D}$, we can construct a vector that contains the values of deviation boundaries for each component of $\hat{D}$. Let us denote this vector as d:

$$d = [d_1, d_2, \ldots, d_{n_{max}}] \,. \tag{4.12}$$

Deviation margin d is calculated individually for each element of the descriptor's sequence using the standard deviation formula σ [2]:

$$d_i = p{\cdot}\sigma_i = p{\cdot}\sqrt{\frac{1}{N}\sum_{i=1}^{N}(\hat{D}(i) - \hat{C}(i))^2} = p{\cdot}\sqrt{\frac{1}{N-1}\sum_{i=1}^{N-1}(A_i - \bar{A}_i)^2} \quad \text{for } i = 1, \ldots, N, \tag{4.13}$$

where N is the size of vector $\hat{D}$. The coefficient p is a constant value that controls the total size of the limit boundary. The bigger the value of p, the more tolerant it is of images that differ from the general pattern of the class. It usually falls within the range $[1, \ldots, 3]$ [87].

This way we can expand our class prototype $\hat{C}$ to include d in order to make it more robust. With this addition the class prototype $\hat{C}$ is as follows

$$\hat{C} = \left[\bar{A}_1 \pm d_1, \bar{A}_2 \pm d_2, \ldots, \bar{A}_{n_{max}} \pm d_{n_{max}}\right] . \tag{4.14}$$

The calculations of the acceptable deviation margin for the class prototype C are the same as in the case of the class prototype $\hat{C}$ and its final form can be summarized in the equation:

$$C = \left[\bar{A}_{11} \pm d_{11}, \bar{A}_{20} \pm d_{20}, \ldots, \bar{A}_{n_{max}m_{max}} \pm d_{n_{max}m_{max}}\right] . \tag{4.15}$$

However, not all images fit into the bracket completely. Because the margin is based on standard deviation, some of the deviations of the descriptor, like the maximum deviation value, may cross the acceptable threshold. Thus, the proposed approach is not accurate on the full scope of the image class.

The proposed approach can be used to solve some image classification problems. In such case, we use the class prototype $\hat{C}$ (or C) in a classification criterion like the mean square error (MSE). The image, described with $\hat{D}$, is assigned to the most fitting class, described with the class prototype $\hat{C}$, according to the minimum value of MSE:

$$\min_{\hat{C}} \text{MSE}\{\hat{C}, \hat{D}\} = \frac{1}{n_{max}} \sum_{n=1}^{n_{max}} (\hat{C}(n) - \hat{D}(n))^2. \tag{4.16}$$

We can use classifiers other than MSE to make classification decisions like neural networks or support vector machines that work well with a vector-based descriptor.

However, this is not the case of a classic classification problem since we do not classify all images. The method relies more on excluding images that do not fit the class prototype C or $\hat{C}$. This makes it an open-class problem. The excluded images are relegated to new class, and out-class or discarded completely.

Properties of Zernike moments (presented in Section 3.1.1) make them a useful tool in image analysis. The moments are very robust against small distortions or noises in images. Moreover, the modules of Zernike moments are rotation invariant. Different moments describe different features of the image which allows us to highlight or select required features from the image. For this purpose we construct a vector descriptor for the image that contains many Zernike moments. It gives us a better control of what features we want to focus on or discard in our image analysis.

Expanding on this idea, it is possible to apply Zernike moments as image descriptors on a broader scale to other fields that rely on pattern identification or analysis. One of such uses can be the problem of image classification. Assuming that images of the same class have similar patters of descriptors, it should be possible to classify them using the proposed class prototypes C and $\hat{C}$.

Chapter 5

Discrete Image Preparation and Processing

This chapter covers the numerical model of the discrete image that is used as the input data in our image calculations for this thesis. We provide the related nomenclature and methods of indexing images. We briefly cover the topic of polar coordinates, the Cartesian-to-polar coordinate transformation and their application in this thesis. Further, we present a selection of standard geometric transformations that serve as additional tools in our image analysis.

Proper image representation in discrete spaces is important in Zernike moment calculations. Zernike moments are continuous and in order to use them in numeric calculations they need to be discretized. We present one such method of discretization in Equation (3.28). However, in discrete computations not only the Zernike moment's equation needs to be discretized, but also the image for which the Zernike moment is calculated. There are many ways of preparing an image for the Zernike moment's calculations. Therefore, this section covers also a brief summary on discrete image preparation and processing in the context of Zernike moments.

The chapter starts with the presentation of the discrete image model relevant to this thesis. Then, we follow with the short description of polar coordinate system and its application in the proposed image descriptors. Finally, we present an overview of standard geometric transformation and their application to discrete image models.

5.1 Discrete Image Representation and Zernike Moments

A digital image is a numeric representation of an image that is composed of picture elements (pixels). A pixel is a basic unit of the digital image that expresses its intensity or gray level in a finite, discrete quantity [37]. Therefore, digital images are also discrete images. The abstract/general distribution of pixels across a discrete image space is shown in Figure 5.1.

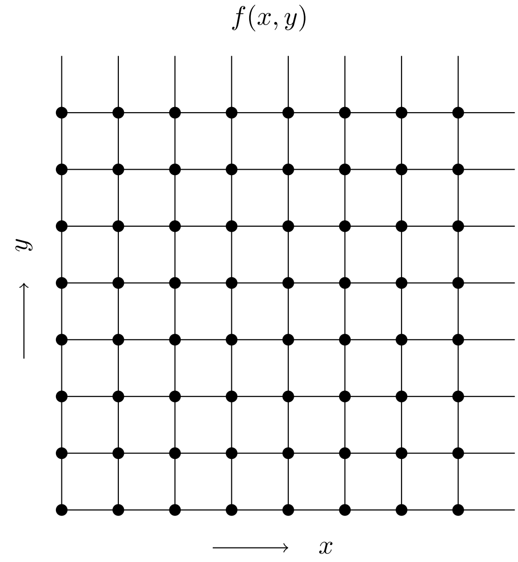

Figure 5.1: The abstract/general distribution of pixels in the discrete image space.

In Zernike moment calculations, we assume that the input image is a two-dimensional and discrete function f that is spread over a limited point grid in the Cartesian space. We denote this two-dimensional, sampled function as $f(x, y)$, where (x, y) is a pair of Cartesian coordinates attached to a numerical value of the corresponding pixel in the image $f(x, y)$. The discrete set of coordinates is indexed as $x = 1...N_1$ and $y = 1...N_2$, where N_1 and N_2 are finite numbers that denote the width and the height of the image in pixels.

This method of indexing the image is shown in Figure 5.2. It is important to note that images usually use the same method of index notation as matrices. In such case, the notation of image's indexes on y-axis is in reverse order to the standard Cartesian coordinate notation. The indexes on x-axis are in the same order as the standard Cartesian coordinate notation. Indexing of images usually starts in top left corner. The order and the distribution of pixels in the discrete space informs us about the orientation and the position of the image in this space.

Therefore, it is important to maintain the correct indexing order since the lack of it can have a major impact on the outcome of the calculations.

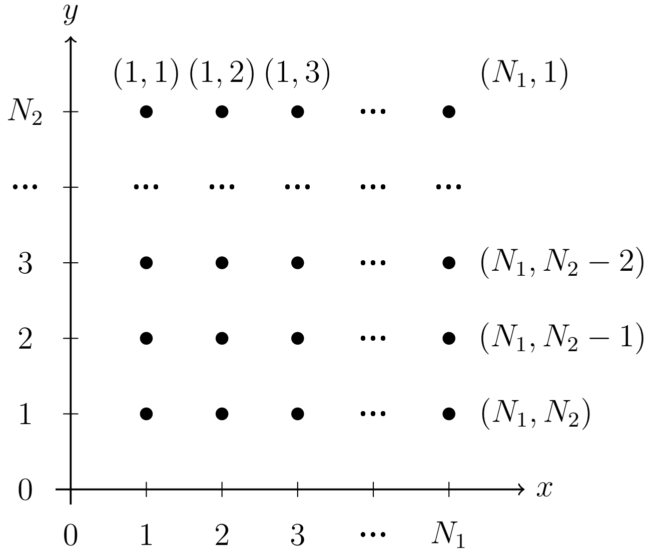

Figure 5.2: A general method of indexing pixels in an image.

Zernike polynomials are radial polynomials continuous over a unit disk [86]. These properties of Zernike polynomials are described in section 3.1 of this thesis. They are summarized by the following set of dependencies (3.2)

$$\begin{cases} \rho = \sqrt{x^2+y^2} \quad \text{with } 0 \le \rho \le 1, \\ \theta = \tan^{-1}\left(\frac{y}{x}\right) \quad \text{with } 0 \le \theta \le 2\pi \quad (-\frac{\pi}{2} \le \theta \le \frac{\pi}{2} \text{ for tan}), \\ x = \rho\cos\theta, \\ y = \rho\sin(\theta) \\ x^2+y^2 \le 1. \end{cases} \tag{5.1}$$

For this reason both Zernike polynomials and Zernike moments often use polar coordinates in their notations (3.1), (3.16):

$$V_{nm}(\rho,\theta) = R_{nm}(\rho)\exp{(jm\theta)}. \tag{5.2}$$

Meanwhile, discrete images are usually spread across a rectangular space in the Cartesian coordinates. In order to calculate Zernike moments, it is necessary to convert image $f(x,y)$ from Cartesian to polar coordinates and map it into the unit disk. We refer to such image as $f(\rho,\theta)$. The conversion of an image from Cartesian to polar coordinates serves to match the image more accurately to the scope of a Zernike polynomial.

The common method of image indexing positions the image in the quadrant I of the Cartesian system as shown in Figure 5.2. Since the unit disk is positioned in all four quadrants by default, keeping the image with the old set of coordinates leaves a lot of space unused. Therefore, to increase the amount of the image data in use, it is often necessary to translate and scale the image to fit it into the unit disk. The transformed image is usually positioned within the unit disk with the origin point of the image located in the center of the coordinate system at $(0, 0)$. It is important to note that after transformation, the image's indexes may move to non-integer values while the image remains discrete. It is the result of the transfer of the image's center to the origin point of the unit circle that in some cases requires estimation of the new position of the image's pixels within the unit circle which may return non-integer values to fit the new criterion.

Two operations on an image's indexes are required to transfer that image into the unit disk: translation and scaling. Translation moves the image's indexes so that the center of the image is positioned at the center of the coordinate system in $(0, 0)$. Scaling is used to resize the index range of the image so that it fits within the boundaries of the unit disk. The number of pixels and the value of pixels in the image remain the same throughout all operations.

We use the model from Figure 5.2 as a reference for this procedure. In the first step, an image is relocated from its original position to the center of the coordinate system. We assume that an image is centered when its origin point, denoted (x_c, y_c), overlaps with the origin point of the coordinate system at $(0, 0)$. This goal is reached by translating the image's indexes using a proper translation vector.

For an image of size $N_1 \times N_2$, the initial position of the origin point (x_c, y_c) is:

$$(x_c, y_c) = \left(\frac{N_1 - 1}{2}, \frac{N_2 - 1}{2} \right). \tag{5.3}$$

The -1 part of the equation accounts for the offset of the image's original indexes that start at $(1, 1)$ and not $(0, 0)$.

Having the value of (x_c, y_c) it is easy to derive that the required translation vector is the negative distance between the origin point of the image and the center of the coordinate system. Therefore, the required translation vector (x', y') is defined as:

$$\begin{cases} x' = x - \frac{1}{2}(N_1 - 1) \\ y' = y - \frac{1}{2}(N_2 - 1) \end{cases} \tag{5.4}$$

This allows to move the center of the image to $(0, 0)$. The pixels after the translation are indexed $x' = -\frac{1}{2}(N_1 - 1), -\frac{1}{2}(N_1 - 1) + 1, \ldots, \frac{1}{2}(N_1 - 1) - 1, \frac{1}{2}(N_1 - 1)$ and $y' = -\frac{1}{2}(N_2 - 1), -\frac{1}{2}(N_2 - 1) + 1, \ldots, \frac{1}{2}(N_2 - 1) - 1, \frac{1}{2}(N_2 - 1)$. Depending on the size of the image N_1 and N_2, the indexes may be assigned integer or non-integer values. It does not change the discrete nature of the image as the arrangement and the number of pixels remain the same regardless of the new position of the image in the coordinate system. The centered notation is presented in Figure 5.3.

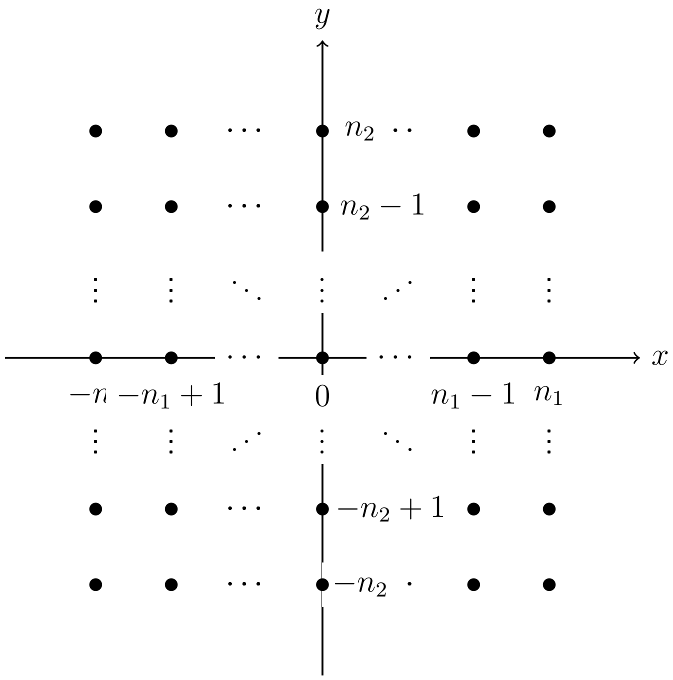

Figure 5.3: Indexing the image's values with the offset that puts the image at the origin point of the coordinate system. Here, $n_1 = \frac{1}{2}(N_1 - 1)$ and $n_2 = \frac{1}{2}(N_2 - 1)$.

Discrete images are usually stored in the form of a rectangle of the size $N_1 \times N_2$ with values $N_1, N_2 > 1$. For this reason we cannot fit them into the unit disk without a loss of some data. In order to use as much image data in calculation it is often necessary to properly scale and position the image in regard to the unit disk.

The original size of the image $N_1 \times N_2$ often puts the border regions of the image beyond the circle of the unit disk. Since the unit disk follows the directive that $x^2 + y^2 \leq 1$, the range of the image's indexes needs to be rescaled so that the border values of the indexes are not greater than 1 so that the image can fit fully within the disk or cover it as tightly as possible.

Depending on the desired outcome, we can decide to position the image within the unit disk with four corners of the image touching the unit circle or to place the image over the unit disk so that the rectangle's sides connect to the unit circle at the poles. The first approach leaves spaces within the disk that do not contain any image data while the second approach leaves some part of the image data outside the scope of the unit disk. The method of data fitting should depend on the content of the image as each approach carries its pros and cons. Positioning the image over the unit disk delivers a fully mapped disk, but looses us the information located in the corners of the image. Fitting the whole image into the unit disk retains all the image data, but leaves areas within the disk that are blank (have null value). Because blank areas do not contain any information it is necessary to assign them a default value which may weight in any future calculations. Both approaches are depicted in Figure 5.4.

Fitting an image which is already positioned in the center of the coordinate system according to Equation (5.4) can be achieved by scaling the values of indexes x' and y' to the interval $[-1, 1]$:

$$\begin{cases} x'' = x'/N \\ y'' = y'/N, \end{cases} \tag{5.5}$$

where N is a scaling constant which value depends on the strategy selected to fit the image into the unit disk. When the objective is to fit a whole image into the unit disk the value of N is:

$$N = \begin{cases} \sqrt{n_1^2 + n_2^2} & \text{for } N_1 \neq N_2 \\ n_1\sqrt{2} & \text{for } N_1 = N_2. \end{cases} \tag{5.6}$$

In this case, we use $n_1 = \frac{1}{2}(N_1 - 1)$ and $n_2 = \frac{1}{2}(N_2 - 2)$ from the centered indexes x' and y' (5.4) as the most distant points in the image. For non-centered indexes x and y, we should use N_1 and N_2 instead of n_1 and n_2 respectively. For covering the unit disk with the image, constant N needs to be:

$$N = \begin{cases} n_1 & \text{for } N_1 \leq N_2 \\ n_2 & \text{otherwise.} \end{cases} \tag{5.7}$$

This is the case for indexes of a centered image x' and y'. For unaligned indexes x and y the scaling constant is $N = N_1$ or $N = N_2$ depending on the case.

Scaling image's indexes so that the image fits with the unit disk is important if we want our calculations of Zernike moments to be as precise as possible. A proper method of scaling image indexes allows us to utilize the most out of the image's data in such cases.

5.2 Cartesian to Polar Coordinate Image Transformation

In polar coordinates the rotation is transformed into a shift. In the case of two-dimensional complex moments, this shift causes a change of phase that can be eliminated by the multiplication of proper moments [34]. This property makes Zernike

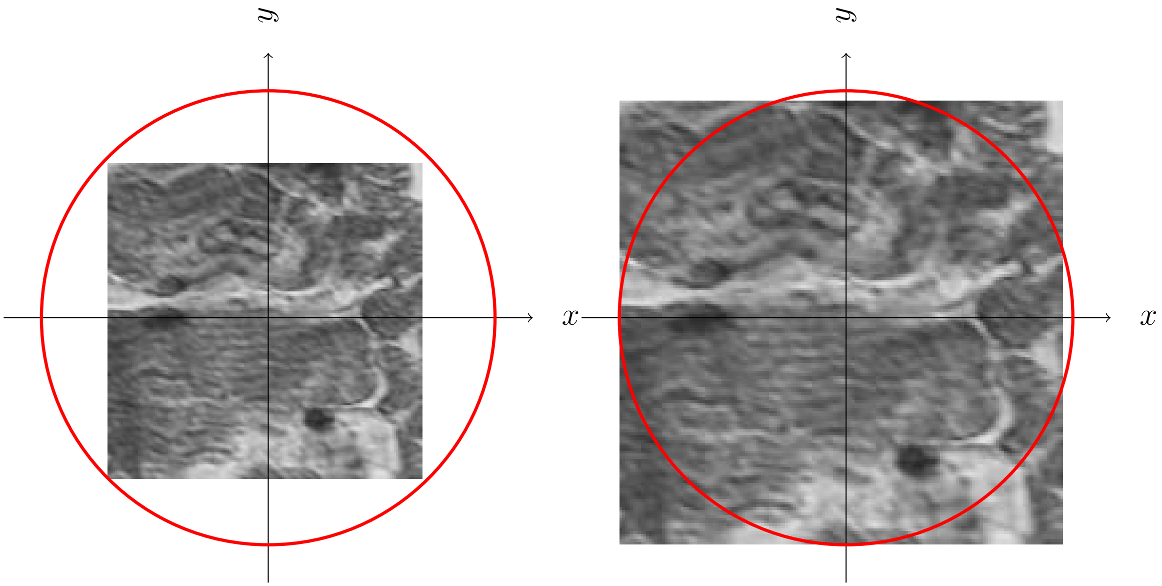

image: a cardiac muscle tissue sample

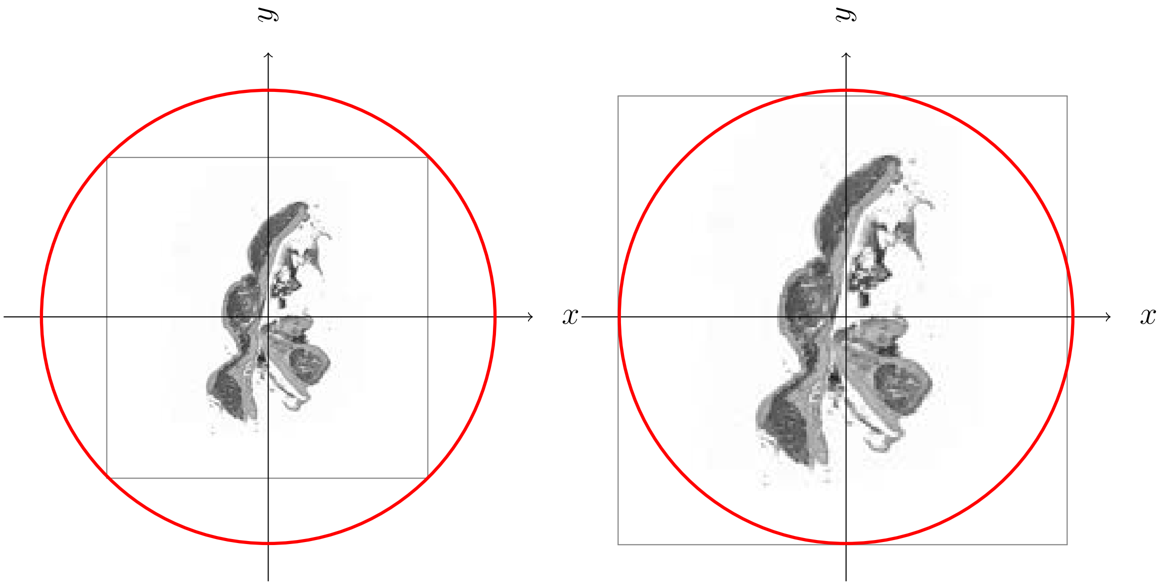

image: an undefined vein slice sample

Figure 5.4: Two methods of fitting an image into a disk: within the area of the disk and over the area of the disk. The application depends heavily on the content of the image.

moments predisposed toward polar notation. Since images are usually provided in Cartesian coordinates it is a good practice to align the image into polar space to make it compatible with Zernike moment calculations. Therefore, Cartesian to polar coordinate transformation of an image is one of the pre-processing steps in calculations of Zernike moments.

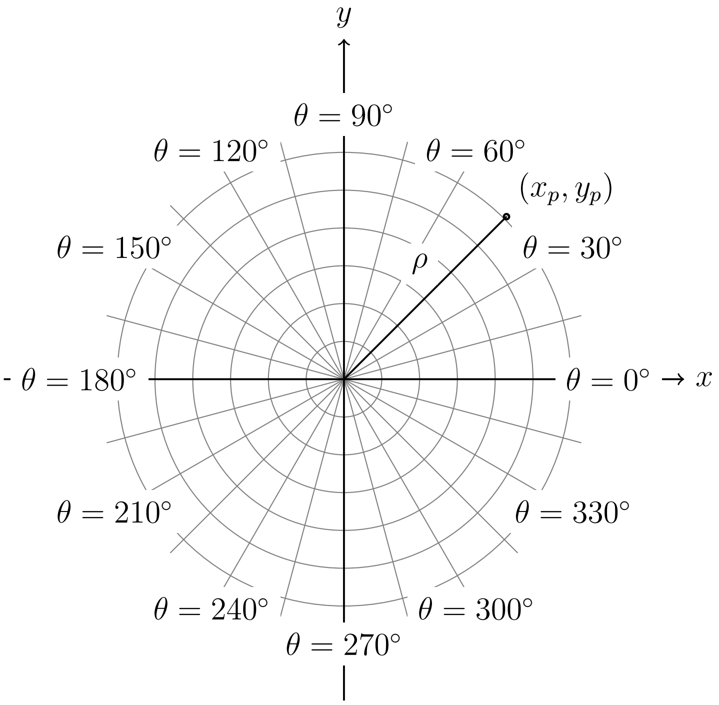

Figure 5.5: Indexing image values in polar coordinates.

Let us use the definition of a discrete image $f(x, y)$ of size $N_1 \times N_2$ from section 5.1, where x and y are indexed according to rules in (5.4) and (5.5). In the polar coordinate system, ρ is the length of the vector from the origin to the point (x, y). θ is the angle between the vector and the x-axis. θ is the angle calculated counterclockwise from the x-axis. This relationship is presented in Figure 5.5.

The conversion of a point (x, y) from Cartesian coordinates to a set (ρ, θ) in polar coordinates goes as follows

$$\rho = \frac{\sqrt{(x - x_c)^2 + (y - y_c)^2}}{\rho_{max}}, \tag{5.8}$$

where ρ_{max} and θ are calculated as

$$\rho_{max} = \sqrt{\frac{M_{00}}{2}} \sqrt{\frac{N_2}{N_1} + \frac{N_1}{N_2}}, \tag{5.9}$$

$$\theta = \arctan\left(\frac{y - y_c}{x - x_c}\right) \tag{5.10}$$

with two-dimensional geometric moment M_{00} being the mass of the image from definition in (3.23). It is assumed that the center of the rotation lies in the center of the mass of the image as referenced in (3.24). In its place, a simple center of the image can be used, where

$$(x_c, y_c) = ((N_1 - 1)/2, (N_2 - 1)/2) \tag{5.11}$$

and in the place of the geometric moment M_{00} we may use the product $N_1 N_2$. The reverse conversion from polar to Cartesian coordinates is as follows

$$\begin{cases} x = \rho \cos(\theta) \\ y = \rho \sin(\theta). \end{cases} \tag{5.12}$$

We use the four-quadrant inverse tangent $atan2(y, x)$ to calculate arctangent. Function $atan2(y, x)$ returns the arctangent of the two numbers x and y. The function uses the signs of both arguments to determine the quadrant of the result in distinction to calculating arc tangent of y/x. The complete definition of $atan2(y, x)$ is as follows

$$atan2(y/x) = \begin{cases} \arctan(\frac{y}{x}) & \text{if } x > 0 \\ \arctan(\frac{y}{x}) + \pi & \text{if } x < 0 \text{ and } y \geq 0 \\ \arctan(\frac{y}{x}) - \pi & \text{if } x < 0 \text{ and } y < 0 \\ +\frac{\pi}{2} & \text{if } x = 0 \text{ and } y > 0 \\ -\frac{\pi}{2} & \text{if } x = 0 \text{ and } y < 0 \\ \text{undefined} & \text{if } x = 0 \text{ and } y = 0 \end{cases} \tag{5.13}$$

Function $atan2(y/x)$ represents the four-quadrant inverse tangent and returns angles on the interval $[-\pi, \pi]$ (in contrast, $atan(y/x)$ returns the limited interval$[-\pi/2, \pi/2]$). To achieve the interval $[0, 2\pi]$ required for Zernike moment calculations, it is necessary to add 2π to all negative values of $atan2(y/x)$.

5.3 Fitting an Image into Polar Coordinate System

We can distinguish two approaches to calculating Zernike moments for a discrete image. The two methods differ in the final accuracy of the transformation as well as its calculation cost. In the first approach, we calculate the moments for the exact amount of information available in the source image. The transformation from Cartesian to polar coordinates is straightforward, but the new coordinates do not cover the polar space adequately. Evenly distributed grid in Cartesian coordinate system does not translate into an evenly distributed polar coordinate grid. In the second approach, we start with an evenly distributed polar coordinate grid and when calculating Zernike moments we interpolate the missing pixels' information using the available image data for each set of polar coordinates in the grid. Not all data from the image is utilized in this approach as we rely on interpolated points.

Images described in Cartesian coordinates cannot be directly mapped onto polar coordinates. A simple point-to-point conversion returns an image that is spread unevenly in the polar space with dense concentration of data closer to the center of the unit disk and missing patches of data appearing across the outer regions of the unit disk. This is not the case for the source image stored in Cartesian coordinates where image data is distributed evenly giving us a better insight into the content of the image. One solution to this issue is to interpolate the missing data points of the unit disk using the data available in the source image. Examples of the direct approach to mapping the image from Cartesian to polar coordinates as well as the reverse mapping of the unit disk using interpolation of image data are presented in Figure 5.6.

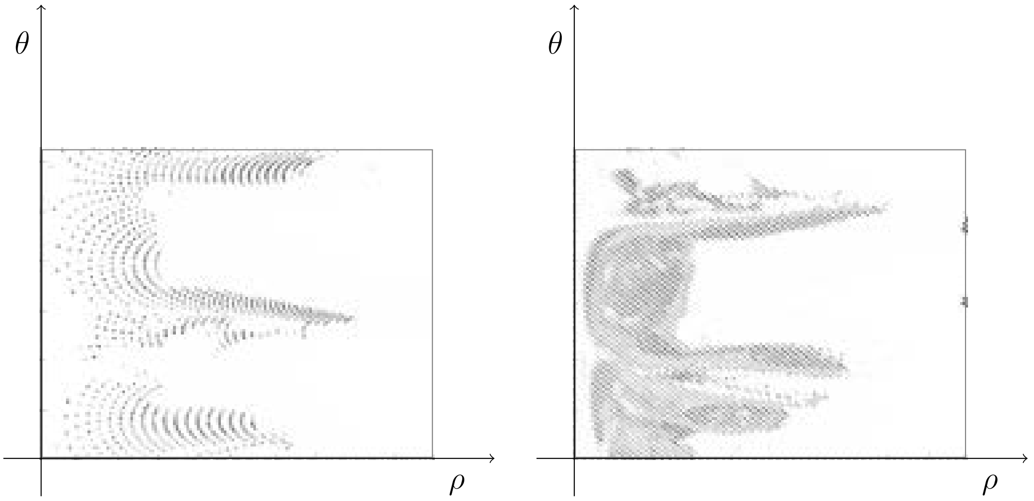

Figure 5.6: Two methods of image conversion from Cartesian to polar coordinates: the direct Cartesian-to-polar coordinate mapping (left image) and the mapping of the unit disk using interpolation of data from the source image in Cartesian coordinates (right image).

Both of these approaches translate to how we can calculate the Zernike moment. In the first approach, the Zernike moment is calculated using the available image data directly. While this approach is easy to apply, the output image in polar coordinates has unevenly distributed data. However, excluding the border pixels of the image, we utilize the majority of the image data, unaltered. The second approach generates an evenly spaced grid of data points within the unit disk. The necessary data points are interpolated from the source image. This approach provides a full coverage of the unit disk. However, this method requires additional calculation load and does not use the source image's data directly. As presented in Figure 5.6, the second approach provides a more complete image of the unit disk in the polar coordinate system.

In Figure 5.8 we show image representation of various types of grids. A Cartesian-type grid is a popular practice of representing a digital discrete image. An image $f(x, y)$ is described by a set of two perpendicular axes x and y. Each point in the coordinate system is assigned a pixel value that contains information on the intensity of the picture it represents. An example of an image in Cartesian coordinates is shown in Figure 5.8b. In the following subfigures, there are examples of images: after direct transformation from Cartesian to polar coordinates Figure 5.8c, after transformation from Cartesian to polar coordinates with interpolation Figure 5.8d, after transformation from polar to Cartesian coordinates Figure 5.8e.

5.4 Geometric Transformations in Discrete Space

One of the aspects of image analysis is the ability to define differences and similarities between images. There are many ways to describe relations between images with different levels of accuracy. Since not every relation can be precisely described due the complex nature of images, a lot of these descriptions are estimations.

There are many factors than can cause differences between images. Some differences are natural and come from two imagined objects being different from each other, because of their inherent nature, e.g. tissue samples originating from two different patients or taken at different points in time. Random, small, noise-induced interference may appear in images distorting the value of some pixels. There are differences in position of objects in images, differences in intensity values of these images and many others. All these differences can overlap in images, making the problem of image registration very complex as there are no universal methods of detecting them.

One way to describe a relation between two images is through transformations. A transformation refers to the mathematical operations or rules that are applied on the image to change its size, shape or orientation. In our context, it describes necessary steps to transform one image into the other. Depending on the nature of transformations we can divide them into rigid and non-rigid transformations. Rigid transformations cover dependencies that can be described with geometric transformations like reflection, rotation and translation. Non-rigid transformations

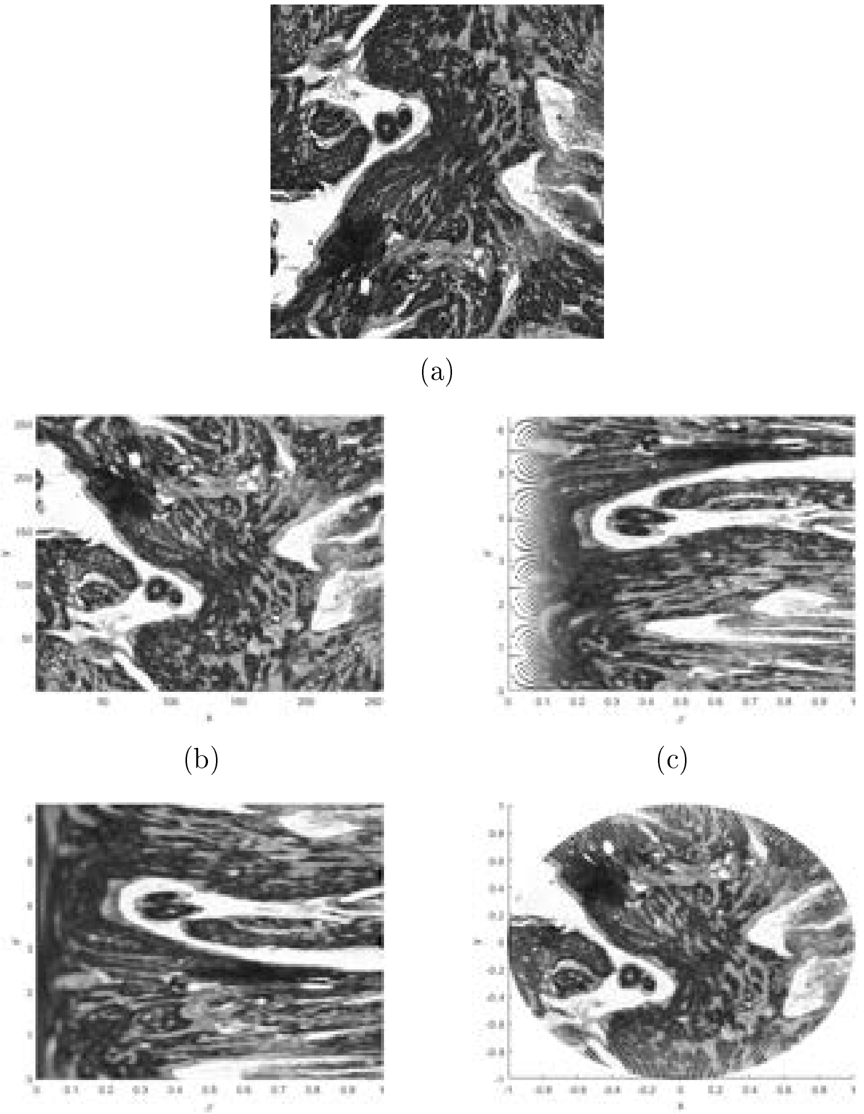

(a)

(b)

(c)

(d)

(e)

Figure 5.7: The compilation of examples of various polar-Cartesian transformations of images sampled with interval = 1px. 5.7a Original image. 5.7b Image in Cartesian coordinates. 5.7c Image in Cartesian coordinates transformed into polar coordinates (no interpolation). 5.7d Image in polar coordinates (interpolated). 5.7e Image in polar coordinates transformed into Cartesian coordinates (no interpolation).

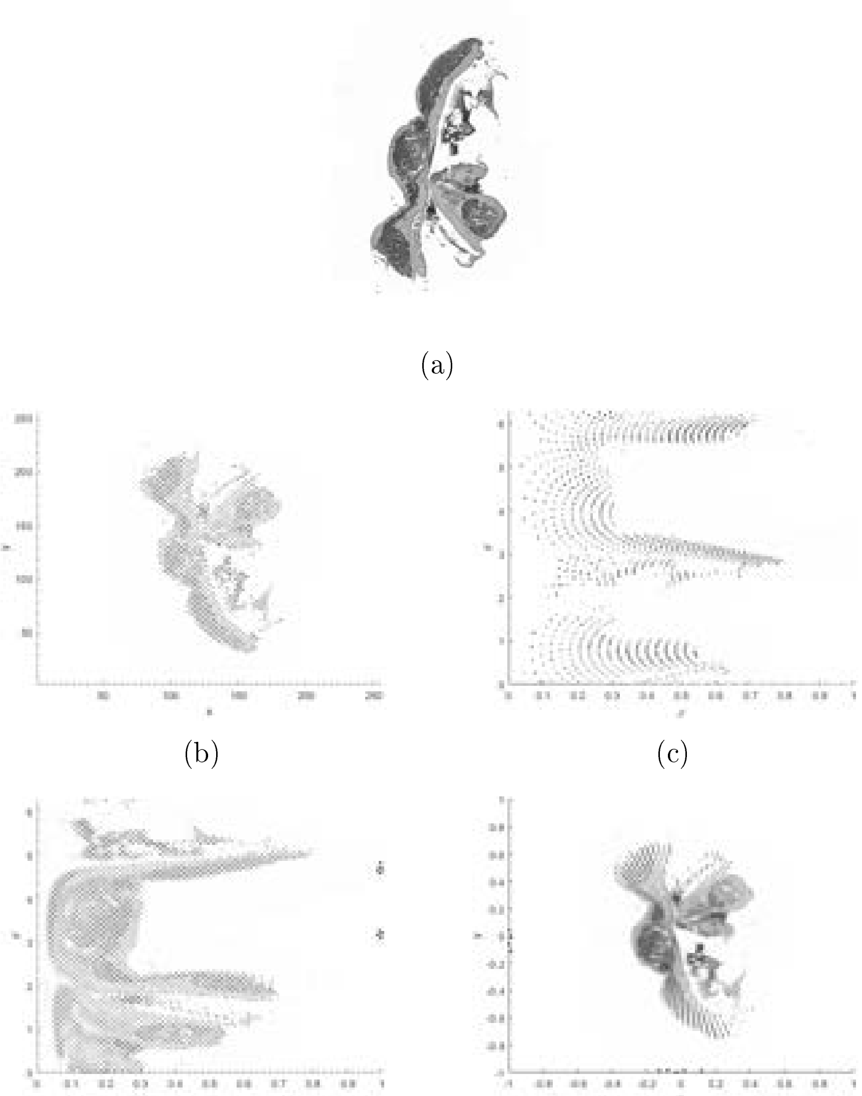

(a)

(b)

(c)

(d)

(e)

Figure 5.8: The compilation of examples of various polar-Cartesian transformations of images sampled with interval = 10px. 5.8a Original image. 5.8b Image in Cartesian coordinates. 5.8c Image in Cartesian coordinates transformed into polar coordinates (no interpolation). 5.8d Image in polar coordinates (interpolated). 5.8e Image in polar coordinates transformed into Cartesian coordinates (no interpolation).

cover transformations which change the size or shape, or both size and shape, of the image. Examples of this type of transformations are operations of dilation and shear. All these types of transformations can occur in various combinations in the image.

In our thesis, we assume that we can describe these relations between images with a set of mathematical equations. The basic idea of modeling dependencies between two images using equations is to find/estimate the position of corresponding pixels in both images [78]. This process is better known as image registration [37]. The equations describe a set of operations necessary to transform a set of coordinates in the first image into their counterparts in the second image. Such approach allows aligning two images into the same coordinate space, making them easier to process and analyze.

Let us assume that images $f(x, y)$ (reference) and $g(x, y)$ (input) represent the same type of objects. We assume that the image $g(x, y)$ is a translated, rotated and reflected replica of the image $f(x, y)$. The difference between these two images can be described by an unknown displacement function $(d_1(x), d_2(y))$ [44]. This relation between two images can be summarized as

$$g(x, y) = f(x + d_1(x), y + d_2(y)), \tag{5.14}$$

$$f(x, y) = g(x - d_1(x), y - d_2(y)). \tag{5.15}$$

The common objective of the image registration is to estimate the affine displacement function $(d_1(x), d_2(y))$. We assume that the displacement can be estimated with a sum of geometrical transformations in a prescribed order: translation, rotation and reflection. We also assume that the final form of displacement $(d_1(x), d_2(y))$ can be obtained by estimating the parameters of its respective composite geometric transformations.

We can establish a general model of a geometric transformation of point (x, y) into point (x', y') as

$$\begin{cases} x' = r_v(x - x_0)\cos\theta + r_v(y - y_0)\sin\theta + x_0 - \tau_1 \\ y' = -r_h(x - x_0)\sin\theta + r_h(y - y_0)\cos\theta + y_0 - \tau_2 \end{cases} \tag{5.16}$$

where

- (τ_1, τ_2) is a translation vector between coordinate systems of f and g,
- (x_0, y_0) is the center of the coordinate system of g,
- θ is the angle of rotation around the point (x_0, y_0) of g,
- r_v and r_h are the coefficients of vertical and horizontal reflection of g respectively.

Each geometric transformation describes an operation that is necessary to align the pixels of image $g(x, y)$ with the pixels of image $f(x, y)$ (the operation can be reversed for image $f(x, y)$). In the following equations, we present the formulas of geometric transformations that are required to move pixel (x, y) to a new, aligned set of coordinates. *Rotation* of image $g(x, y)$ by angle θ around origin point (x_0, y_0) takes the form

$$f(x, y) = g(x_\theta, y_\theta) \tag{5.17}$$

where x_θ and y_θ are given by

$$\begin{cases} x_\theta = (x - x_0)\cos\theta + (y - y_0)\sin\theta + x_0, \\ y_\theta = -(x - x_0)\sin\theta + (y - y_0)\cos\theta + y_0. \end{cases} \tag{5.18}$$

Translation of image $g(x, y)$ by translation vector (τ_1, τ_2) is described as

$$f(x, y) = g(x - \tau_1, y - \tau_2). \tag{5.19}$$

There are two types of reflection transformations. *Vertical reflection* of image $g(x, y)$ about a vertical axis of abscissa x_0 is given by

$$f(x, y) = g(-x + 2x_0, y). \tag{5.20}$$

Horizontal reflection of image $g(x, y)$ about a horizontal axis of ordinate y_0

$$f(x, y) = g(x, -y + 2y_0). \tag{5.21}$$

We can also derive a more general form of reflection of point (x, y) by origin point (x_0, y_0):

$$\begin{cases} \hat{x} = r_v x + (1 - r_v)x_0 \\ \hat{y} = r_h y + (1 - r_h)y_0 \end{cases} \tag{5.22}$$

where r_v and r_h describe parameters of vertical and horizontal reflection respectively. The parameters take up values $r_v = 1$ and $r_h = 1$ if the image is not reflected. For reflection about a vertical axis of abscissa x_0, the parameters take up values $r_v = -1$ and $r_h = 1$

$$\begin{cases} \hat{x} = -x + 2x_0 \\ \hat{y} = y \end{cases} \tag{5.23}$$

and for reflection about a horizontal axis of ordinate y_0 the parameters take up values $r_v = 1$ and $r_h = -1$

$$\begin{cases} \hat{x} = x \\ \hat{y} = -y + 2y_0. \end{cases} \tag{5.24}$$

Reproducible methods of describing differences between images play a big part in image registration. Most importantly, they provide us with numerical tools to express and measure differences between two images. Geometric transformations are one of such methods. They describe one of the most common types of differences that can occur between images (e.g. translation, rotation) using a set of parameterized formulas. It is necessary to note that this approach works for a specific set of problems, where the pair of images depicts similar content, but transformed geometrically in some way. We cannot estimate geometric differences between two unrelated images. The premise of estimating geometric transformations is that the differences in the images are geometric in nature, that means that objects in the images are either rotated, translated, scaled or reflected. Despite these drawbacks, this approach is applicable to the problem of medical image registration where we know that images have similar content that otherwise may have been geometrically transformed during the process of acquisition or somewhere in post-processing.

Chapter 6

Practical Application of Zernike Moments in Microscope Image Sequencing

This chapter covers a selected set of medical image registration problems along with proposed methods of solution. At the center of these problems, we have microscope images of histological sections and tissue samples. It is a subcategory of medical images that consists of big-resolution images which contain a very detailed cell structures of biological tissues taken at varying levels of magnitude. On the basis of goals and requirements, we can group the mentioned problems into the following categories: registration and sequencing of microscope image series, recognition and classification of types of tissue and detection of damage and other aberrations in microscope images.

The sequencing problem revolves around aligning and finding the order of a microscope image series of tissue sections. The actual order of sections is undetermined and custom-designed methods of evaluating it are often necessary. Other issues include misaligned placement of sections in the original images. Before constructing or reconstructing the sequence it is important that all sections are positioned in the same direction. For that reason, some methods of aligning sections must be a part of the solution.

In this thesis, we rely mainly on Zernike moment descriptors, which are our proposed solution to the mentioned problems. We include other methods for comparison purposes like edge histogram descriptors [81]. Previously, the problem of sequencing of microscope slides is included in [104]. However, that approach does not rely on Zernike moments in any way, but uses SOM Kohonen networks to map the transition of slides.

Each of the following sections focuses on one of the problems. Sections are organized into smaller parts that contain a short presentation of the problem, relevant issues and goals as well as the proposed method of solution and examples of use. We cover the use of Zernike moment descriptors in the solution as well as other supporting formulas. We test the usefulness and effectiveness of the approach using an appropriate set of examples for this type of problem. Furthermore, we include the obtained results and their analysis. Finally, we deliver a brief summary and provide conclusions.

6.1 Application of Edge Histogram Descriptors in Microscope Image Sequencing

This section focuses on the application of edge histogram descriptors in the problem of image sequencing. The problem is a popular subject of research [106], [128], [57]. The goal is to construct an ordered sequence out of microscope images of histological sections. Such sequences of images find application in the task of 3D reconstruction of objects from slices among their other uses [6], [46]. However, for this to work all slices must be aligned with each other before reconstruction. Therefore, this problem has two stages: the alignment of all images, so that their content is in the same position and orientation, and the construction of the ordered sequence in preparation for the 3D reconstruction.

The main subject of this problem are tissue samples. Images contain tissue slices placed within the solution. In most cases it is the problem of a dark object on the light background. Here, we focus on aligning the fragments of the tissue in an order that corresponds to the slight changes of the tissue's body between the subsequent slices. We analyze the scenario, where all tissue slices come from the same source material. Some images contain deformed tissue samples, tissue samples with missing fragments or tissue samples with differing levels of intensity. The goal of this image registration is to find the actual order of samples or its most accurate estimation. The constructed sequence would allow us to track the changes across the body of the tissue over a period of time.

The main purpose of edge histogram descriptors is to align the target in the image so that all targets in the image series are positioned in the same way. This allows us to better track the changes of the data in the images and gives us a more precise picture of the state of the tissue, e.g. how it changes along its length or how it changes in time. Edge histogram descriptors have a history of use in image analysis detecting objects in the image [1] or in automatic categorization and annotation of images [111], [117] in both medical [113] and industrial [85], [103] fields. Although in most cases they are supported by other image analysis methods or play the supporting role.

6.1.1 Radial, Vertical and Horizontal Edge Histograms

We assume that differences occurring between two images can be described using rigid transformations like translation, rotation or reflection. We assume that any of these differences can be tracked on point-to-point basis between pixels of two images. Estimating the parameters of rigid transformations serves as means to align two images in the sequence. We can describe the potential dependency between two images as

$$I_1 = Refl(I_2) \otimes Rot(I_2) \otimes Trans(I_2), \tag{6.1}$$

where I_1 and I_2 are images and $Refl$, Rot, $Trans$ describe the geometric transformation of reflection, rotation and translation respectively. The equations for these transformations are described in (5.18), (5.19), (5.20), (5.21). Non-rigid transformation can also occur in images. However, they do not belong to the scope of the thesis.

Using the value and position of pixels in the image to estimate the relative position of the image within a specific space is a popular method of image matching or sequencing. There are many ways to describe the correspondence between the pixels in two images. Some descriptors rely on the shape context of pixels [12], global and semi-local edge histograms [123] or gradient histograms [99].

In this aligning strategy we use edge histogram descriptors (EHD) with horizontal, vertical and complete 1-to-360 degree edge. This approach is well-known from Otsu's work [81] and have been explored many times since then [65], [84], [127], [91].

Edge histograms refer to the concept from the probability theory and statistics of marginal distribution of a joint distribution of a discrete pair of random variables. In the case of EHD for images it is constructed by calculating the sum of pixels across a given pattern, e.g. vertically for each row or horizontally for each column. The purpose of EHD is to estimate the position or in some cases the shape and the size of the object in the image.

In this thesis we use three types of edge histograms. A **radial edge histogram** describes the characteristic of the image by evenly-spaced radius that crosses the centre of the image. It is also used to estimate rotation and reflection in the image. This edge histogram is calculated with

$$H_r(\theta) = \sum_{x=x_c}^{N_1} I((x - x_c)\cos\theta + x_c, -(x - x_c)\sin\theta + y_c) \quad \text{for } \theta = 0, \ldots, 2\pi, \tag{6.2}$$

where x_c and y_c are the center of mass of the image. It allows us to approximate the center of the object in the image. It is important as (x_c, y_c) serves as the rotation point of image rotation and constitutes as the reference point in calculations of radial histograms and estimation of the rotation between images. The N_1 and x in this formula should correspond to the smaller dimension of the image. An example of a radial histogram is in Figure **??**.

The center of the mass (x_c, y_c) is determined using the following formula

$$(x_c, y_c) = \left(\frac{\sum_{x,y} x w(x,y)}{\sum_{x,y} w(x,y)}, \frac{\sum_{x,y} y w(x,y)}{\sum_{x,y} w(x,y)} \right), \tag{6.3}$$

where the weight function $w(x, y)$ is calculated with

$$w(x, y) = a(I(x, y) - m), \tag{6.4}$$

where m is a boosting parameter for either dark or bright pixels in the image that takes up a value $m < \min_{x,y}(I(x, y))$, when $a > 0$ and $m > \max_{x,y}(I(x, y))$, when $a < 0$. Parameter a describes whether the center of the image (x_c, y_c) moves toward bright pixels $(a > 0)$ or dark pixels $(a < 0)$ of the image. Which value of a is used depends on whether the object in the image consists of bright or dark pixels. In practical application $a = 1$ for bright object and $a = -1$ for dark objects. This approach to locating the center of the image comes from van Assen's work [115]. Determining a center of the mass that becomes the point of origin for radius in the radial histogram allows us to keep uniform distribution of the histogram points. It also allows for initial estimation of vertical and horizontal translation.

A **horizontal histogram** describes the characteristic of the image over its columns and is calculated according to

$$H_h(x) = \sum_{y=1}^{N_2} I(x, y) \quad \text{for } x = 0, 1, \ldots, N_1. \tag{6.5}$$

The practical application of a horizontal edge histogram for a simple object in the image is shown in Figure **??**. The purpose of this type of histogram is to estimate the horizontal translation in the image. A **vertical histogram** covers the characteristic of the image over its rows and is calculated with

$$H_v(y) = \sum_{x=1}^{N_1} I(x, y) \quad \text{for } y = 0, 1, \ldots, N_2. \tag{6.6}$$

Analogically to its horizontal counterpart, it is used to estimate the vertical translation in the image. In both formulas (6.5) and (6.6) N_1 and N_2 are the width and the height of the image I respectively.

Two edge histograms allow us to compare two images in a measurable way. Depending on the type of histogram it allows us to determine rotational, vertical

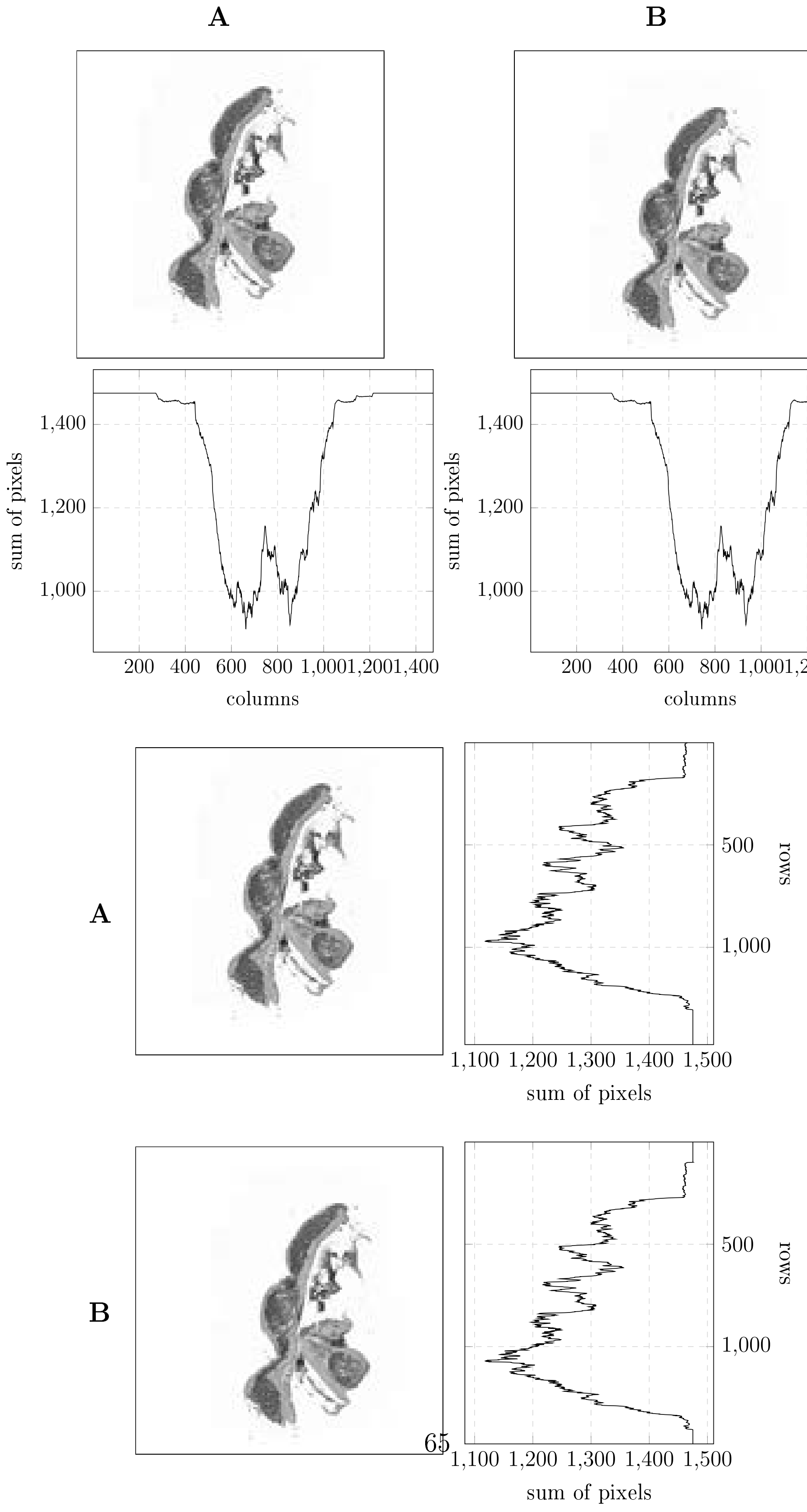

Figure 6.1: First example of horizontal and vertical edge histogram descriptors for a pair of microscope images. Image B is a copy of image A translated by the vector $\tau = (80, 100)$.

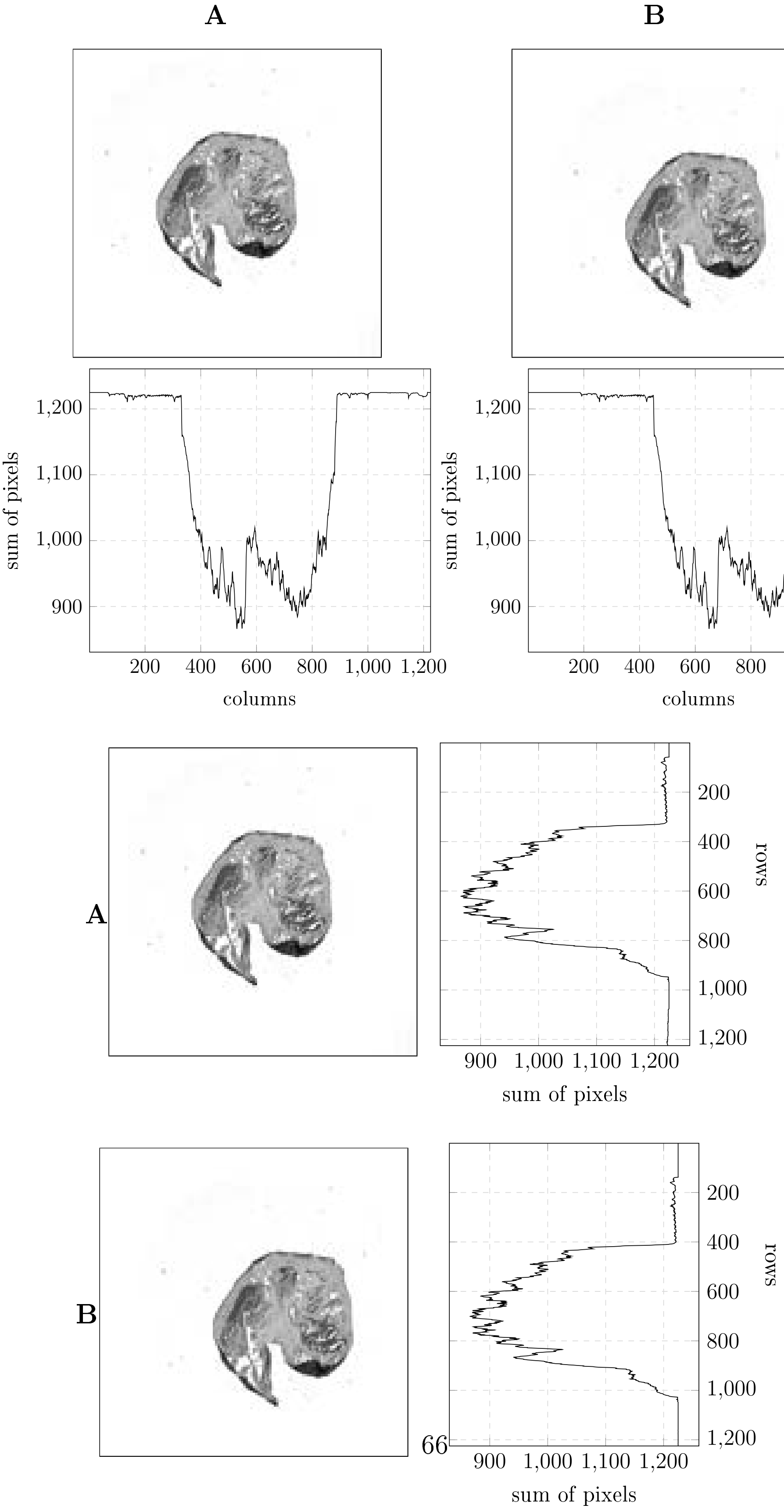

Figure 6.2: Second example of horizontal and vertical edge histogram descriptors for a pair of microscope images. Image B is a copy of image A translated by the vector $\tau = (120, 80)$.

or horizontal shifts between the images. Estimating the difference between two edge histograms of images allows us to estimate the actual difference between the original images. However, this method may not be very accurate when there are many transformations present and overlapping in the image. Any translation in the image affects the central point of rotation, and any rotation in the image skews the vertical and horizontal estimations. These are not the only transformations occurring in the images that can affect the estimation process.

Different levels of intensity in grayscale or binary images influence the final shape of the edge histograms. Edge histograms accumulate values over rows or columns of the image, therefore, it is important to take into the account which type of pixels are representing the object in the image. Dark pixels in the image are represented by values closer to 0, while light pixels move toward 1. Images with dark object on the light background translate to edge histograms with a dip in the values corresponding to the position of the object. In the case of light objects on the dark background, the edge histograms have a hill in the values corresponding to the position of the object in the image. Matching the highs and lows in the histograms of two images allow us to estimate the difference between these images. This difference allows us to estimate the parameters of the geometric transformations needed to align both images so that the target tissue lands in the same position and orientation for both images.

However, these properties of edge histograms disqualify them from describing more homogenous images since they do not have enough distinct features to discern the object from the background. This is not the issue when the goal is oriented on the general shape and position of the object in the image since more detailed descriptions like structure of the cells are not necessary in such cases.

The error criterion that is used for estimation of the displacement is the absolute mean error value of the difference in the histogram levels. The formula for this estimation criterion for radial histograms is as follows

$$\min_{\Delta\theta} \sum_{\theta=0}^{2\pi} |H_{r1}(\theta) - H_{r2}(\theta + \Delta\theta)|. \tag{6.7}$$

The goal is to find such $\Delta\theta$ value that delivers the lowest value of the absolute difference between two histograms. This is the rotation displacement we seek. To check if reflection occurs in one of the images, the formula from (6.7) needs to be slightly modified to:

$$\min_{\Delta\theta} \sum_{\theta=0}^{2\pi} |H_{r1}(\theta) - H_{r2}(2\pi - \theta + \Delta\theta)|. \tag{6.8}$$

$H_{r2}(2\pi - \theta)$ in this case is the inverse (reflected) histogram of $H_{r2}(\theta)$. If the displacement $\Delta\theta$ has a lower value for the inverse histogram it indicates that the reflection is present in the image. Graphic examples of radial edge histogram descriptors for a pair of images are in Figure 6.3 and 6.4.

In the case of vertical and horizontal histograms the model is very similar, but instead of angles we use pixel values

$$\min_{\Delta\tau} \sum_{\tau=1}^{N} |H_{vh1}(\tau) - H_{vh2}(\tau + \Delta\tau)|, \tag{6.9}$$

where H_{vh} is either a vertical or a horizontal histogram, $\Delta\tau$ is the vertical or horizontal displacement and N is appropriately the height or the width of the image.

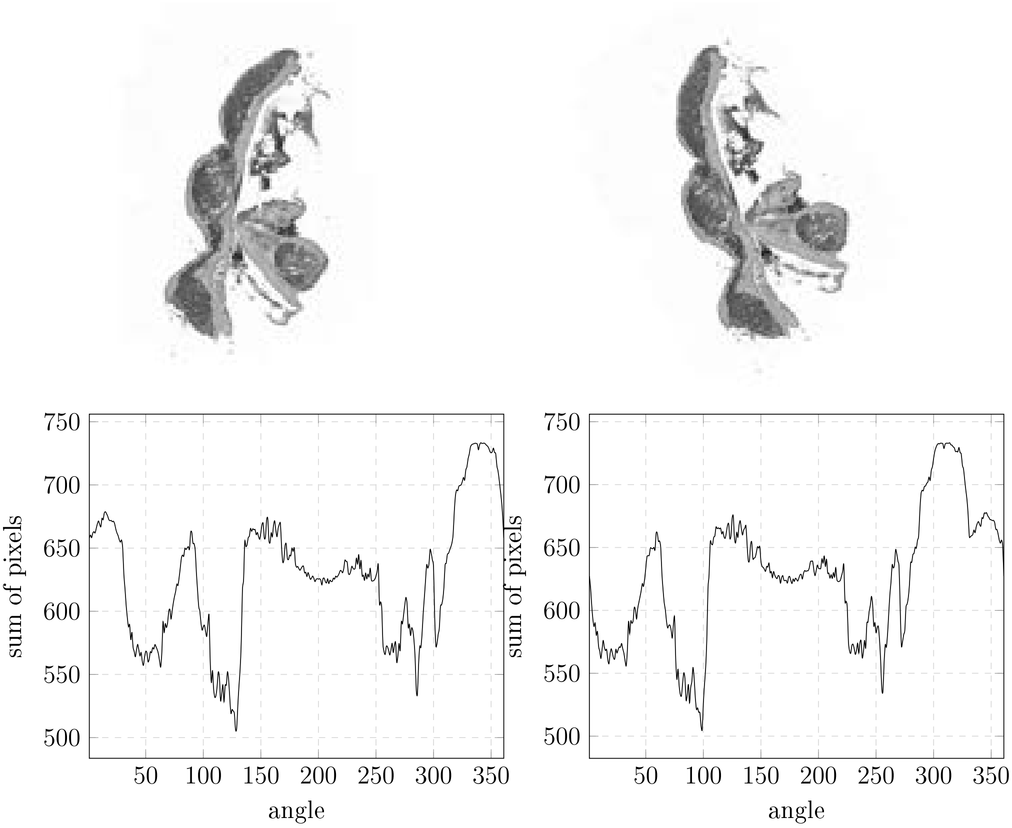

Figure 6.3: First example of radial edge histogram descriptors for a pair of microscope images rotated by the angle $\theta = 30°$.

In theory, the value of the error for a match should be 0. It is the case for artificially generated images or images with artificially generated transformations. However, in most cases we deal with images that have overlapping transformations.

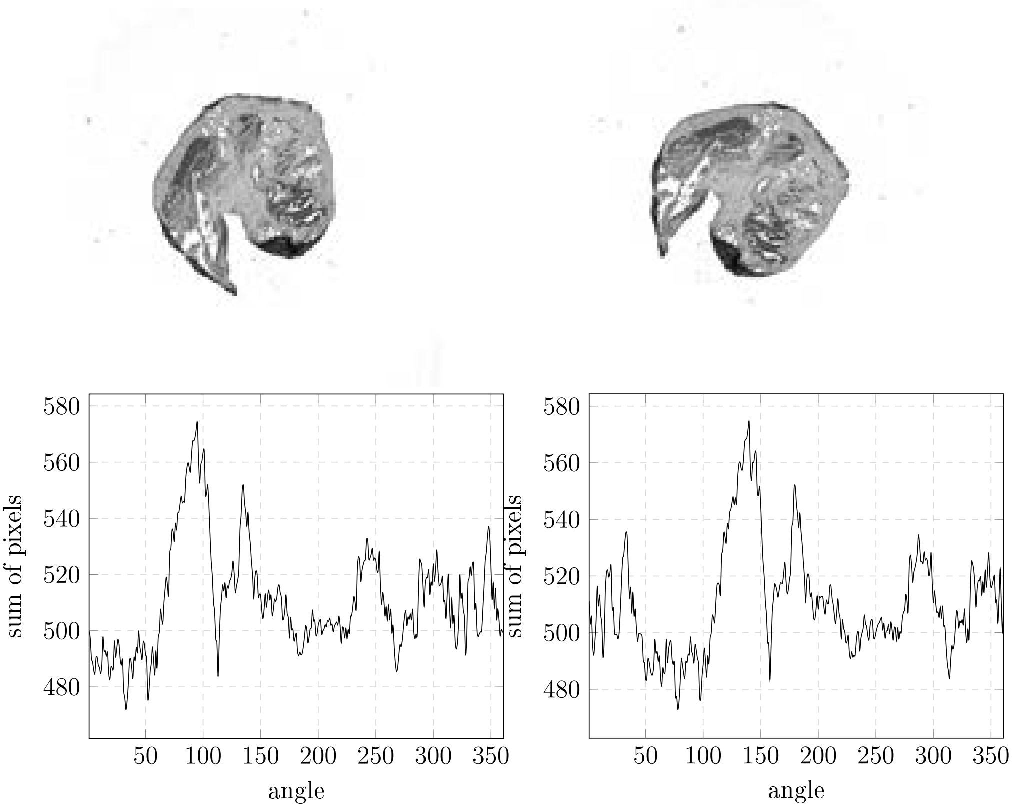

Figure 6.4: Second example of radial edge histogram descriptors for a pair of microscope images rotated by the angle $\theta = 45°$.

There is no effective method of separating different transformations from each other. Multiple transformations interfere with the estimation of parameters, and it is impossible to eliminate their dependencies out of the process. Therefore, there is always some value of error present in the estimation of parameters of these transformations. Since we cannot eliminate the error, we have to minimize it. For this reason, we do not have the exact values of parameters, only their estimations.

6.1.2 Use of Edge Histogram Descriptors in Image Sequencing

In practice, medical images are complex and the differences between images are caused by many types of transformations. The differences can come from random noise in the image, spatial displacement of the object in the image or be a result of the damage done to the image, among many others (chapter 5.4). Many transformations often overlap. Therefore, it is impossible to determine one type of transformation without interference from other types of transformations. Situations where the difference between two images can be described with one type of transformation do not happen in practice and are reserved for more artificial exercises.

Edge histogram descriptors are also subject to this constraint. Reflection, rotation and translation overlap in images, and we cannot estimate one rigid dependency without interference from the other transformations. Therefore, in this approach we aim to minimize the overall error that comes from these dependencies between histograms.

Since we cannot separate transformations, it is important to retain a certain order of estimating the transformations' parameters. The order is constructed in such a way that allows us to minimize the interference from overlapping transformations as we work our way down the estimation process. We start with estimation of the center of the object in the image. It allows us to minimize some dependencies from translation and rotation. It is important that the center of the radial edge histogram lies in the center of the object in the image. This minimizes the interference from translation in rotation estimation at this stage. Then, we determine if any image is reflected using radial histograms using a reflected version of the radial edge histogram. After determining reflection and rotation's parameters the objects in the images should be facing int the same direction. Finally, we can estimate the position of the object in the image and align it across all images.

We assume that three types of rigid transformations can occur in the image concurrently and that the difference between images is caused only by these transformations. In this approach, we choose to ignore differences caused by other factors on the assumption that they do not cause major interference. The rigid transformations in this approach are rotation, translation and reflection. **Rotation** is determined by the displacement on the θ axis between radial edge histograms of two images. The difference is described with $\Delta\theta$. **Translation** is determined by the displacement $\Delta\tau_1$ and $\Delta\tau_2$ on the N_1 and N_2 axis respectively. This pair of values is calculated for vertical and horizontal edge histograms separately ($\Delta\tau_1$ for vertical and $\Delta\tau_2$ for horizontal). **Reflection** requires us to run the estimation of rotation twice. Firstly, with the radial histograms of original images, secondly, with the inverted radial histogram of one of the images. The inversion emulates the reflection of the image. A reflection in one of the images makes it almost impossible to estimate rotation (and translation) correctly. Therefore, the presence of a reflection needs to be determined before further estimation. The presence of the reflection can be deduced from the value of the difference between radial histograms of two images. The pair of images with the lowest value of the difference determines if the reflection occurred in one of the images or not.

The ordered sequence is constructed using EHD. The decision criterion is the minimum value of the sum of all differences between EHDs for the complete sequence of all images. A single difference is calculated for each pair of images positioned next to each other in the sequence. It is the distance between two images in the sequence. The output sum is the sum of all differences. It describes the similarity of images in the sequence. A disordered sequence generates a bigger value of the sum compared to an ordered sequence because distances (and following differences) between subsequent images are bigger.

Since the problem of ordering images in the sequence using EHD relies on minimizing the value of distances between subsequent images we can categorize it as a scheduling problem. In such case the best order in the sequence has the shortest distance between images. This allows us to use methods of solution which work for discrete problems of this type, eg. simulated annealing.

The correct order of the images in the series is estimated using a specified metric. This dependency is described with criterion ϵ

$$\epsilon = \sum_{x,y} |I_1(x,y) - I_2(x,y)|. \tag{6.10}$$

The value of ϵ corresponds to the difference between two images, the lower the value, the more similar are the images. Identical images have the ϵ value at 0. The criterion depends on the differences between corresponding pixels in the image and because of that it can be influenced by the variation of intensity levels in images.

We use an optimization algorithm to determine an ordered sequence with minimum value of discrepancies between consecutive images. Using the data from Table 6.1 it is possible to construct such sequence. The optimization algorithm for this problem is as follows

$$\sum_{i=1}^{length(S)-1} T(S_i, S_{i+1}), \tag{6.11}$$

where T is the fitting table and S is the image sequence. The goal of the optimization is to minimize the joint sum of all errors between each image passage in the sequence.

The main advantages of this approach are that it provides many potential sequences at once (global optimization) and two alternative solutions for every pair of images in that sequence. However, it is quite fragile since a single bad match can disturb the entire sequence. The approach does not support local optimization which may lead to missing best local alignment. The algorithm is easy to modify. Variations of tabu search algorithms that discard some proposed solutions or optimization by minimization of the biggest error in the sequence may be applied in such situations.

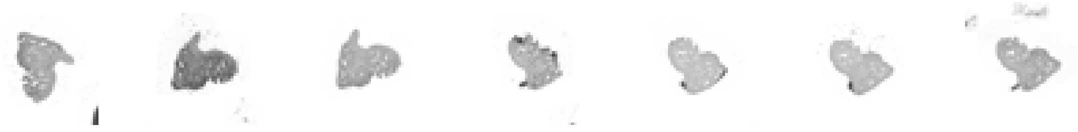

Figure 6.5: Microscope image series S105.

We test the proposed approach on a few series of unmarked microscope images of histological sections. The objects in the images are depicted with dark pixels on the light background and have irregular shapes. Examples of such series are in Figures 6.5, 6.9a and 6.10a. We test if EHDs allow us to align the histological sections. Using a complete survey algorithm we establish an ordered sequence on the basis of the lowest total sum of errors between subsequent images in the series as defined in (6.11). Figure 6.5 contains a series of microscope images of tissue sections that are unordered and unaligned. We can find the necessary steps to align two subsequent images in the series by estimating the values of parameters of geometric transformations differentiating the images. We start by positioning the content of the image at the center of the mass in the image according to (6.3). This step minimizes the impact of the original translation displacement in the estimation of rotation in the following step. It is important to note that both translation and rotation of the section in the image influence each other and can cause some errors in the estimations. Then, we calculate R-EHDs for images using (6.2). R-EHDs have two purposes: to detect whether reflection occurred in the image, secondly, to estimate the rotation between images necessary to align those images. Figure 6.6 shows examples of R-EHDs for a pair of images and

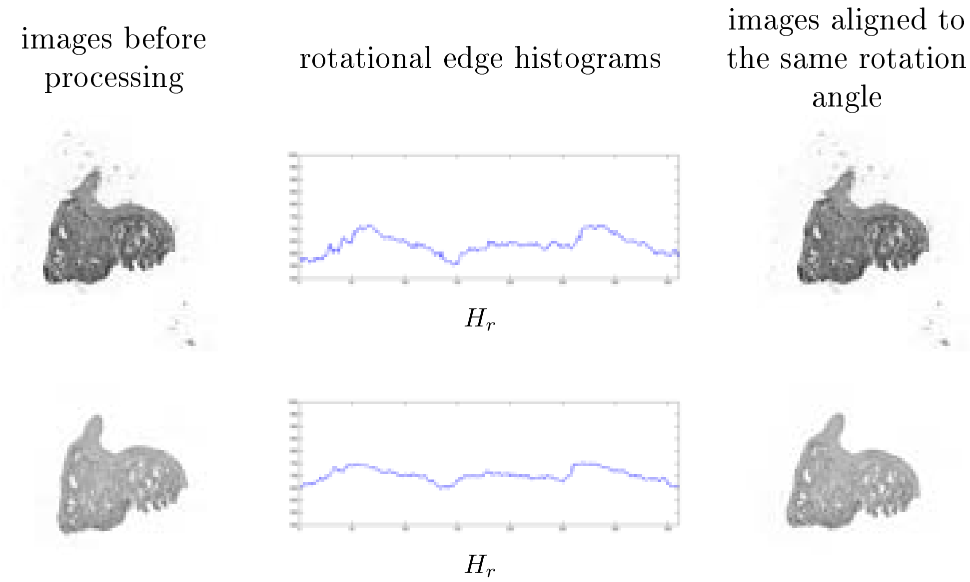

Figure 6.6: An example of comparison of rotation using R-EHDs for a pair of images in series S105.

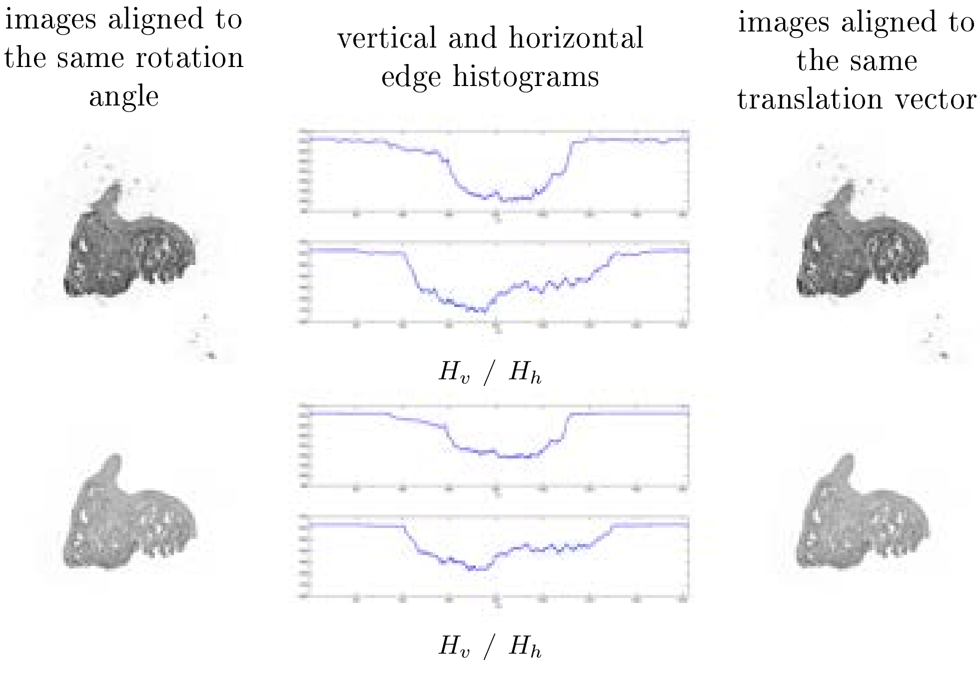

Figure 6.7: An example of comparison of horizontal and vertical translation using HV-EHDs for a pair of images in series S105.

how it translates to aligning both images so that they have the same orientation. The necessary rotation is estimated from the shift between two R-EHDs of two images along their θ-axis as highlighted in (6.7). With images aligned according to detected reflection and estimated rotation we can move on to estimate translation. This approach eliminates to some extent the influence of the rotation occurring concurrently in the images. In the estimation of translation we us two EHDs: a vertical and a horizontal. The histograms are calculated from the formulas (6.5) and (6.6). As in the case of the last estimation, both vertical and horizontal translation is estimated from the shift along the x and y axes of the histograms respectively. This step is shown in Figure 6.7 for a pair of images. The images are once again aligned using the estimated translation. This is the last step of estimation for the pair of images. Afterwards, the process is repeated for the next image in the series which gets to be aligned to the one of the already-aligned images. The algorithm finishes when all images in the series are aligned to the same position and orientation in the image. We expect some minor differences between subsequent images that are the result of the irregular shape of the sections that cannot be perfectly matched.

	I-1	**I-2**	**I-3**	**I-4**	**I-5**	**I-6**	**I-7**
I-1	0.0000	0.0453	0.0307	0.0416	0.0494	0.0498	0.0556
I-2	0.0523	0.0000	0.0410	0.0494	0.0527	0.0520	0.0653
I-3	0.0338	0.0399	0.0000	0.0339	0.0282	0.0276	0.0372
I-4	0.0370	0.0497	0.0355	0.0000	0.0421	0.0433	0.0485
I-5	0.0346	0.0522	0.0280	0.0424	0.0000	0.0204	0.0304
I-6	0.0337	0.0513	0.0276	0.0441	0.0200	0.0000	0.0281
I-7	0.0438	0.0645	0.0386	0.0533	0.0362	0.0355	0.0000

Table 6.1: Fitting table T for sequencing using MSE approach that contains calculated value of ϵ for each pair of images in the microscope series.

In the next stage, we estimate the order of the images in the series using a simple complete survey algorithm to find the sequence with the lowest error as declared in (6.11). However, this approach works only if we have a few images in the series. For bigger image series, we have to use different optimization algorithms like tabu search or simulated annealing. For the complete survey we build a fitting table using error ϵ from (6.10). It describes the difference between each pair of transformed images (positioned and aligned in the same direction). The goal is to find such sequence that the passages between subsequent images lead to the lowest overall sum of all errors. An example of such table for image series S105 is in Table 6.1.

We use three series of microscope images to test the proposed method. Image series are small and constitute of 5 samples for series S5, 10 samples for series S27 and 7 samples for series S105. The content of images consists of tissue sections that have varying orientation and position in the image and in intensity levels. Some samples have deformed structures, most noticeable in fringe regions of the sections. Samples is the series are not exact matches of each other, so there is always some value of the error.

The steps of the proposed approach are already described. Here, we present the results. We focus on the visual representation of both the unordered and ordered sequences for the testing. For series S105 from Figure 6.5, we obtained the following order of images as shown in Figure 6.8. Images are aligned using rotational, horizontal and vertical EHDs. We calculated the value of the difference between each pair of images. This is the data that is required to construct the sequence according to (6.10). It is collected in Table 6.1.

Other examples are shown in Figure **??** which shows ordered sequence of image series S5 from Figure **??** and in Figure 6.10b which shows ordered sequence of series S27 from Figure **??**.

Visual inspection shows that images in the sequence are aligned in the same direction and follow a certain order. Since the actual order of the sequence is not known we are unable to verify how the obtained sequence compares to it. Using mostly the visual confirmation and the selected error criterion we can assume the validity of both the order and the alignment of tissue sections in all sequences. The diverse nature of the samples does not appear to impact the process significantly.

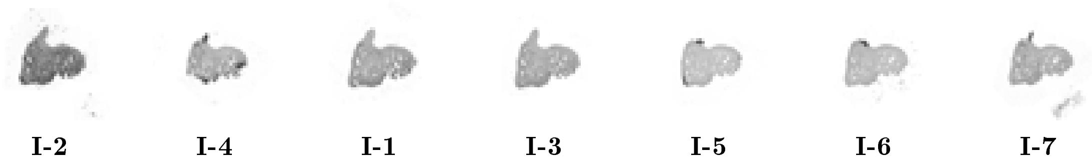

Figure 6.8: Ordered microscope image series S105 using edge histograms and optimization.

In this chapter we cover a two-step algorithm of automatic image alignment and sequencing for series of microscope images of tissue sections. In the first step, we use edge histogram descriptors to estimate parameters of geometrical transformations between images. The second step is sequencing of aligned and transformed images using a simple optimizing algorithm of complete survey and a designed error criterion to obtain a general order of images.

Edge histogram descriptors allow us to estimate the displacement that is in the form of translations, rotations and reflections in images. However, the algorithm is sensitive to intensity levels in the image since it relies on the contrast between the object and the background to properly mark the position of the object in the image. With weak contrast the difference between images may not be detected accurately.

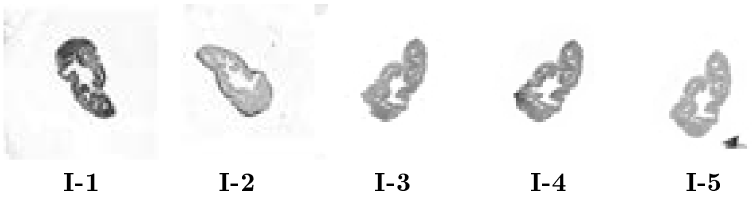

(a) Unordered image series S5.

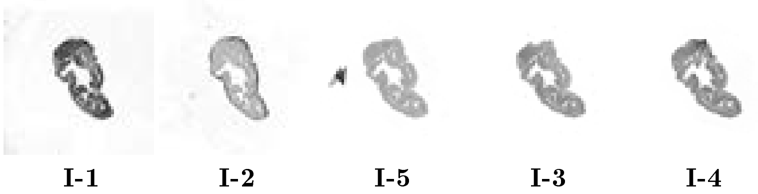

(b) Ordered image series S5.

Figure 6.9: Application of edge histograms and sequencing to image series S5.

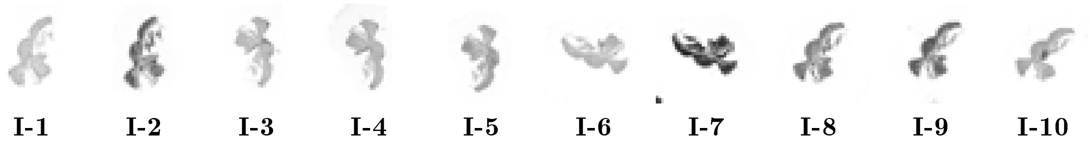

(a) Unordered image series S27.

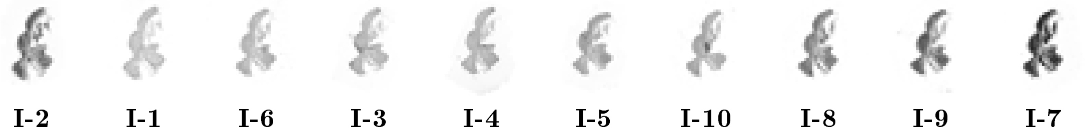

(b) Ordered image series S27.

Figure 6.10: Application of edge histograms and sequencing to image series S27.

Moreover, radial edge histograms have reduced accuracy closer to the edge of the radial circle since sampling there is more sparse. In the case of reflection, we need to run rotation estimation twice using the original and the reflected image, then compare both histograms.

The ordered sequence is constructed using a global fitting algorithm. Such approach allows for a complete survey of all available solutions in search of the best fit. The subsequent images in the ordered sequence are transformed to match the common reference system. Usually, the first image in the ordered sequence is used as the point of reference. This way all the images in the sequence point in the same direction and are easier to analyze. The global match metric does not ensure the quality of the local match and alignment.

The proposed method finds applications in aligning and sequencing of microscope images of histological sections. It allows us to establish the correlation between features in a set of images and to apply transformation models to achieve that correlation of features. This can serve us in constructing an ordered sequence on the basis of similarity and feature correlation of images. The method's use can be expanded further, e.g. in 3D reconstruction of tissue from tissue sections in microscope image series where such order is important.

Some improvements are necessary to make the method more robust. Equalizing the intensity levels of images in pre-processing may lessen their influence on the final outcome. Similarly, differentiating the object in the image or reducing the weight of the background using a threshold or segmentation may improve image processing by removing noise and redundant information from the image. For sequencing and ordering we can use a different error criterion that is better at comparing tissue samples. The sequencing algorithm can be modified so that it takes into the account local and global optima and makes the search less taxing on resources than the complete survey. A better-tailored fitting algorithm for this type of problem is a necessity if the number of images in the microscope image series is extensive.

6.2 Microscope Image Series Sequencing with the Use of Zernike Moments

This section follows up on the problem of sequencing of microscope images of tissue sections. In this case, however, we approach the problem using Zernike moment descriptors as the basis of our solution. For this, we rely on the properties of Zernike moments, mainly, feature recognition and the rotation invariance of the module. Our goal is to recreate a potential sequence of tissue sections for an image series. We achieve it by comparing the calculated Zernike moment descriptors of images in the series and finding the sequence containing the lowest sum of differences between subsequent images. For reference, we also construct image sequences using edge histogram descriptors (mentioned in previous section) as well as a combination of both Zernike moment descriptors and edge histogram descriptors. The main objective is to test the viability of Zernike moment descriptors for the problem of sequencing tissue sections in microscope image series. Our previous approach to this problem included direct on-image calculations which relied on center of gravity and Phase-Only Correlation functions [39].

The sequencing relies on Zernike moment descriptors of images in the series. We calculate a Zernike moment descriptor for each microscope image. The sequence is achieved by analyzing the differences between corresponding values of Zernike moment descriptors for pairs of images and finding the order that returns the smallest value of the total sum of all differences. We assume that the bigger the difference the further apart the images are in the series. For two identical images the difference should be 0. We assume that the sequence with the smallest value of the total sum of all differences between each subsequent pair of images is the optimal order for this image series.

We describe images in the series with Zernike moment descriptors (ZMD). The descriptor is introduced in previous chapter and defined in (7.6):

$$A_1, A_2, \ldots, A_{n_{max}}, \quad \text{where } A_i = \sum_m = A_{im}. \tag{6.12}$$

In this equation n_{max} describes the maximum order of the Zernike moment that we apply in the descriptor. Such versatility allows us to adjust the accuracy of the descriptor as well as focus on the feature of the image that are of importance.

We use the mean squared error to measure the difference between ZMDs of images. For ZMDs this error is calculated as follows:

$$\epsilon = \sum_n^{n_{max}} |A_n^{(1)} - A_n^{(2)}|, \tag{6.13}$$

Here, (1) and (2) describe two images from the pair that is being compared and A_n is n-th element of the ZMD. The sequence is constructed by minimizing the total sum of all errors for each subsequent image pair. To find this value we use standard optimization algorithms. Since the number of images in the series is small, we rely on complete survey to find the best order of images. More sophisticated algorithms are required in the case of larger sets. We compare the results of sequencing with the results obtained for the edge histogram descriptor (EHD) from Section 6.1.

We select 3 microscope image series of tissue sections as input data to test this approach. Series contain groups of tissue sections of the same biological subjects. While the majority of samples retain the same shape across all images, some of them have missing fragments and different intensity levels. Series are unordered which means that we do not know the exact order of sections in the series. The goal of the method is to order images in such a way that the differences between consecutive section are minimal. Image series are labeled using their original notation: S27, S40 and S105. Series S27, S40, S105 are shown in Figure 6.11, Figure 6.12 and Figure 6.13 respectively. The number of images in each series is 10 for S27, 9 for S40 and 7 for S105.

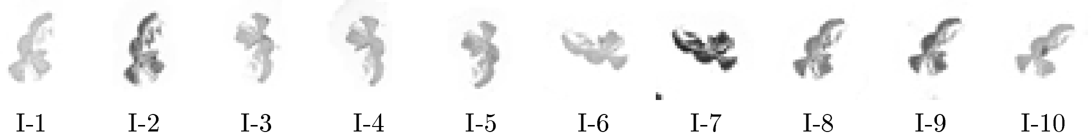

(a) Unordered/original sequence of tissue sections from series S27.

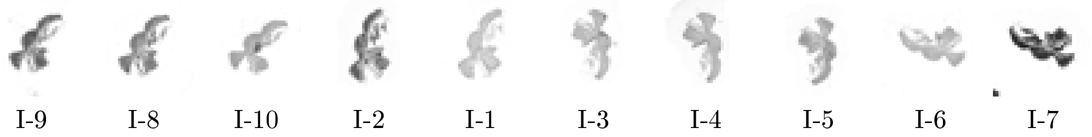

(b) Sequence ordered with Zernike Moment Descriptors (n_{max}=20).

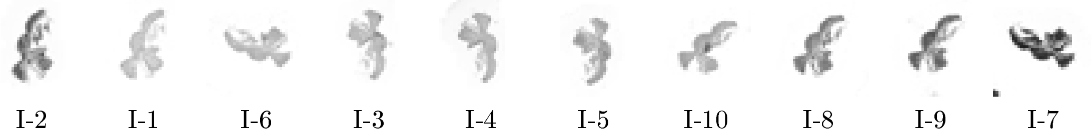

(c) Sequence ordered with Edge Histogram Descriptors.

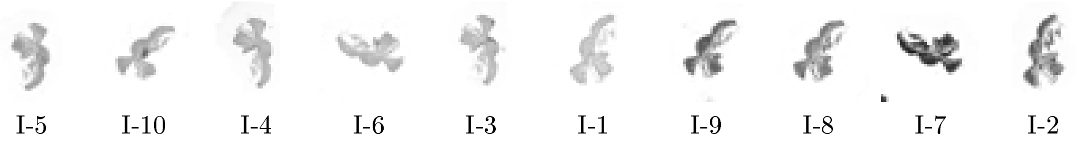

(d) Sequence ordered with EHDs and ZMDs (n_{max}=20).

Figure 6.11: Sequencing of microscope tissue sections using of Zernike Moment Descriptors and Edge Histogram Descriptors for series S27.

We ran initial tests on whether ZMD are viable for the problem of image sequencing and how the number of moments and the size of the image influence

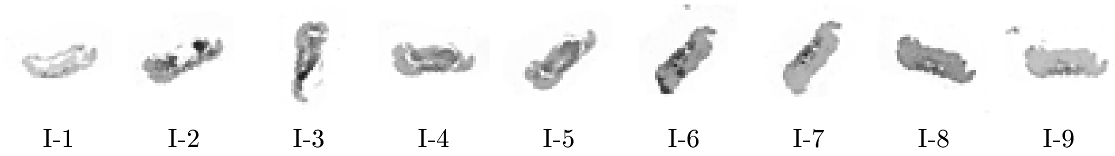

(a) Unordered/original sequence of tissue sections from series S40.

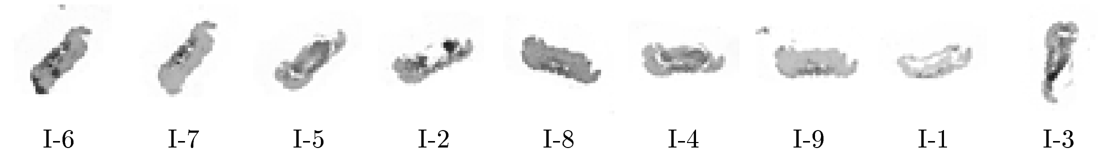

(b) Sequence ordered with Zernike Moment Descriptors (n_{max}=20).

Figure 6.12: Sequencing of microscope tissue sections using of Zernike Moment Descriptors and Edge Histogram Descriptors for series S40.

position	1	2	3	4	5	6	7	8	9	10
original	I-1	I-2	I-3	I-4	I-5	I-6	I-7	I-8	I-9	I-10
ZM	I-9	I-8	I-10	I-2	I-1	I-3	I-4	I-5	I-6	I-7
EHD	I-2	I-1	I-6	I-3	I-4	I-5	I-10	I-8	I-9	I-7
EHD+ZM	I-5	I-10	I-4	I-6	I-3	I-1	I-9	I-8	I-7	I-2

Table 6.2: Summary of the new and original order of tissue sections in series S27 using combination of edge histogram descriptors (EHD) and Zernike moment descriptors (ZMD).

position	1	2	3	4	5	6	7
source	I-1	I-2	I-3	I-4	I-5	I-6	I-7
ZM	I-1	I-4	I-5	I-6	I-7	I-3	I-2
EHD	I-2	I-4	I-1	I-3	I-5	I-6	I-7
EHD+ZM	I-4	I-5	I-6	I-7	I-2	I-1	I-3

Table 6.3: Summary of the new and original order of tissue sections for series S105 using combination of edge histogram descriptors (EHD) and Zernike moment descriptors (ZMD).

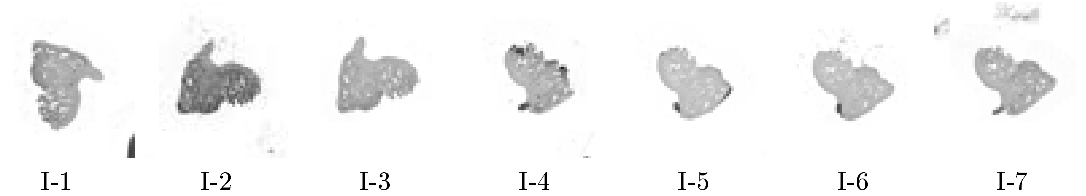

(a) Unordered/original sequence of tissue sections from series S105.

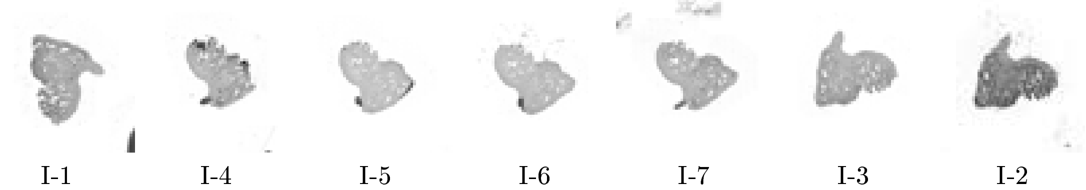

(b) Sequence ordered with Zernike Moment Descriptors (n_{max}=20).

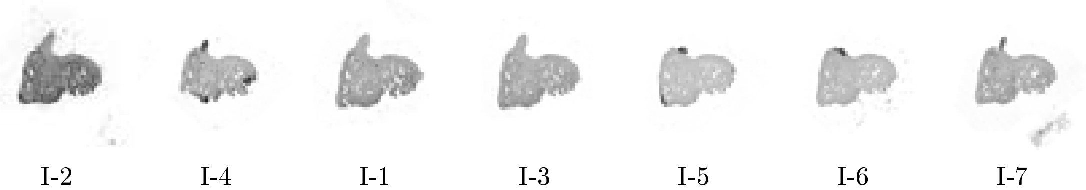

(c) Sequence ordered with Edge Histogram Descriptors.

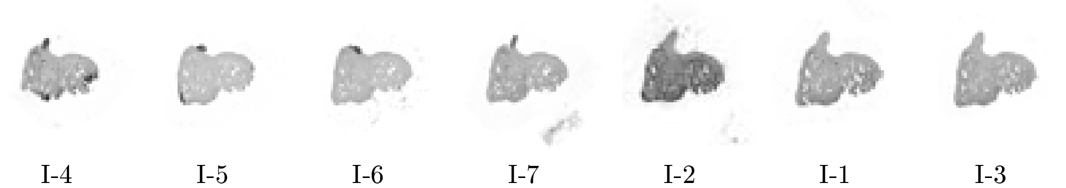

(d) Sequence ordered with EHDs and ZMDs (n_{max}=20).

Figure 6.13: Sequencing of microscope tissue sections using of Zernike Moment Descriptors and Edge Histogram Descriptors for series S105.

the outcome of sequencing. The tests were run for different number of Zernike moments in the descriptors. That is for $n_{max} = \langle 10, 15, \ldots, 45 \rangle$. The size of the image took up the values $N = \langle 128, 255, 512 \rangle$.

As it turned out the size of the image does not impact the outcome significantly. However, it is different with the number of moments. With higher n_{max}, the ZMD gets more accurate in its description of the image. Using moments of a lower order leads us to basic shape-recognition, while moments of a higher order give us more detailed account. Because of the computational restrictions of our equipment, we encountered numerical errors at $n_{max} = 50$. Therefore, the maximum acceptable $n_{max} = 40$. A broader study of the impact of the number of Zernike moments in image reconstruction is shown in [72]. It is established that the higher is the order of a Zernike moment, the more precise is both the error reporting and the reconstruction of the image. In the majority of our cases, we obtained similar results across different sizes of images. However, the number of moments does noticeably impact the computation time of their calculations. These conclusions influenced further testing and allowed us to avoid such sets of calculation parameters that would return us superfluous results.

We summarized the results of each image sequencing in a dedicated table. The data covers three approaches to the sequencing problem: ZMD-only, EHD-only and combining ZMD and EHD. Results for series S27 are in Table 6.2 and for series S105 in Table 6.3. The tables contain the record of new positions of images in the sequence, estimated using each of the proposed methods. Visualization of new sequences from the tables are in Figure 6.11 to Figure 6.13.

As the results show, the positions of images differ between sequences acquired through different methods. Key difference is also that not all approaches return an aligned set of images. In EHD method, the sequence is constructed mostly on the basis of the shape of the tissue section in the image. During this phase the sections are also aligned into the same position and orientation in the image. The rest of the assessment is performed using MSE criterion and complete survey algorithm. In ZMD method, the ordered sequence is built according to the values of ZM in the descriptor. Unlike in the EHD, in this method, we do not need to transform images in any way in order to construct a sequence. Another major difference is that the EHD deals with data directly from the image while the ZMD works with already processed information (ZM). These are the main difference between ZMD and EHD approaches. It is also the reason why we use a combined ZMD and EHD method in the last approach. Here, we use ZMD to determine the order of the sequence and EHD to finally align sections. This approach makes use of the ZMD's data processing qualities and the EHD's ability to align the content of the image to provide an ordered and aligned sequence of microscope tissue sections.

When it comes to ZMDs, the construction of the sequence requires Zernike moments to be calculated for each image only once. The ZMD approach is highly independent of the size of the image used in calculations. Even using a small set of moments of the low order provides good results. With ZM's values previously calculated, the process is easily repeatable. While Zernike moments are rotation and reflection invariant [62], the output sequence does not have image aligned into common direction or position. Necessary translations and rotations have to be done in post-processing. ZMDs are good to describe the similarity between shapes of objects in images which allows us to determine their relative positions in the image sequence. They can further allow us to establish a group similarity which may be useful in classification problems. Translation and scale changes can influence both the value of a Zernike moment and the sequencing process itself further down the line. Therefore, it is often necessary to center the object in the image before performing any calculations of ZM to avoid such influences.

Using sequences from Figure 6.11 to Figure 6.13 as references, we can in a way examine the accuracy and the viability of the proposed approach. Since the actual order is unknown, there is no valid criterion that can ascertain the actual order of sections in the series. Visual inspection does not bring the definitive decision on the effectiveness of each approach. Both the ZMD and the EHD appear to be successful in establishing an ordered sequence of microscope images that follow a certain pattern. However, the advantage of Zernike moments is that they are also applicable in problems where we need to match not only shapes, but also full-image patterns. The downside is that this approach does not return any information on image alignment (in contrast to EHD) and any image alignment has to be done in post-processing.

6.3 Sequencing of Microscope Image Series with Accumulated Zernike Moments

This section follows on the role of Zernike moment descriptors in the problem of sequencing and provides a more in-depth analysis of the method. The focus is on accumulated Zernike moment descriptors, which expand on the concept of Zernike moment descriptors. This approach is introduced in chapter **??**. The main goal remains, and it is to establish an ordered sequence of tissue sections. Additionally, we investigate the distribution of accumulated Zernike moments across the sequence and how individual Zernike moments relate to their position in the sequence. By analyzing the position of the moments in the sequence for different series of images, we can work out how to utilize them to obtain better description results for various image types. We test this approach on image series of tissue sections.

We have a group of image series that can be divided into two categories: artificially generated and natural. The artificially generated sequence is a series of images with established order that is known to us. We artificially created this type of sequence. It is constructed by cloning an image and applying slight modification to it on its consecutive iterations. This way we have a series of images where re-ordering is possible, thus the results can be evaluated accurately. Examples of such sequences are shown in Figure 6.14 and 6.15. The natural sequence describes a series of images, where the order is unknown. This is an image series where we cannot be sure of the actual order of the sequence, only estimate it. Examples of such sequences are shown in Figure 6.16, 6.17 and 6.18.

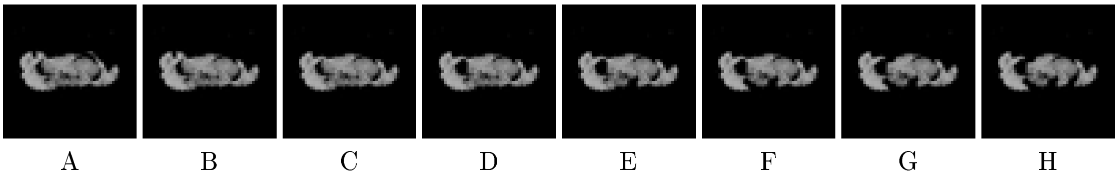

Figure 6.14: Artificially generated series of microscope images S40 (series #1) with contrast background.

Using Zernike moments as the basis of our method, we construct two types of characteristics that work as image descriptors. The first type of the descriptor describes the complete characteristic that consists of subsequent module values of Zernike moments A_{nm} for all subsequent pairs of the order and the repetition (n, m):

$$(n, m) = (1, 1), (2, 0), (2, 2), \dots, (n_{max}, m_{max}), \tag{6.14}$$

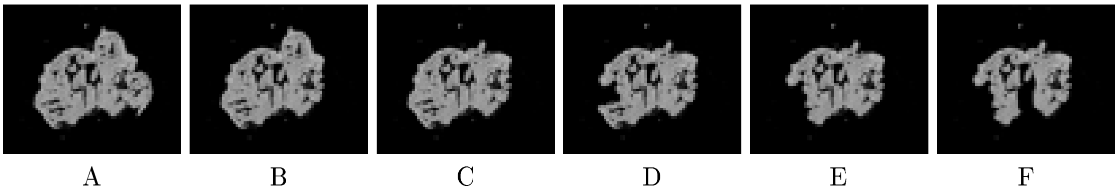

Figure 6.15: Artificially generated series of microscope images S5 (series #2) with contrast background.

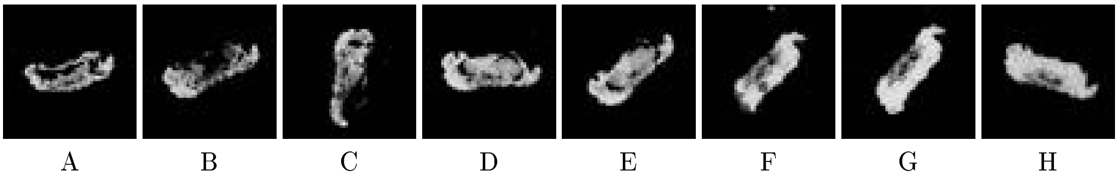

Figure 6.16: Natural series of microscope images S40 (series #3) with contrast background.

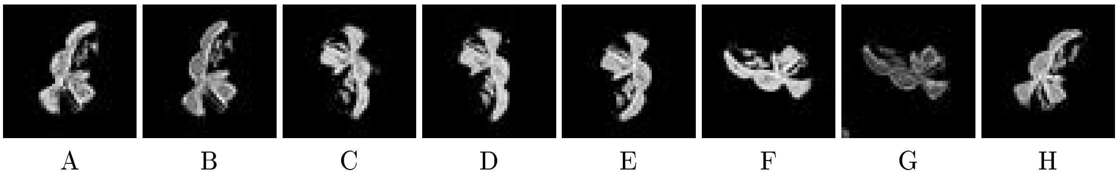

Figure 6.17: Natural series of microscope images S27 (series #4) with contrast background.

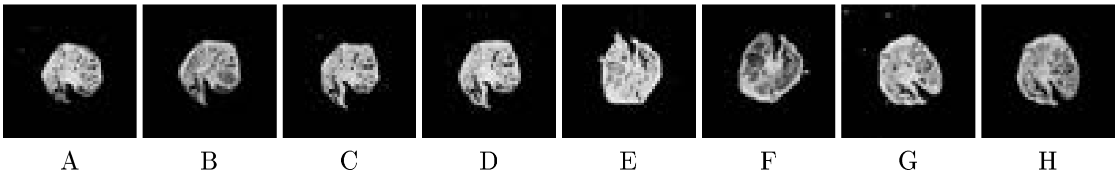

Figure 6.18: Natural series of microscope images S102 (series #5) with contrast background.

where each (n, m) still has to comply with the classic Zernike moment's constraints. The second type of the descriptor is the accumulated characteristic that also consists of modules, but that of the sum of Zernike moments of a given order n.

In the case of the complete characteristic the image can be described with a series of modules of Zernike moments A_{nm} defined by the pair (n, m) and the maximum order of n_{max}. This characteristic can be simplified by grouping and accumulating the values of moments within the given order. Such characteristic is built by adding up all the moments of order n

$$A_n = \sum_m A_{nm}, \tag{6.15}$$

where m is the potential repetition of the order n that fulfills the rules $|m| \leq n$ and $n - |m| = even$.

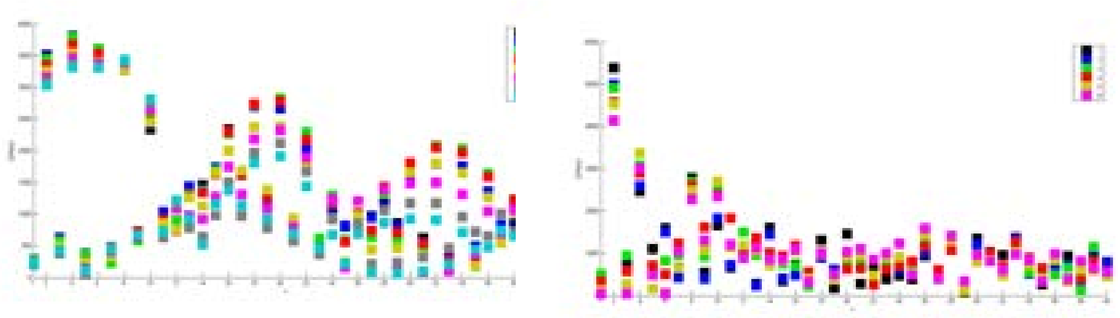

(a) Series 1 - artificially generated series S40.

(b) Series 2 - artificially generated series S5.

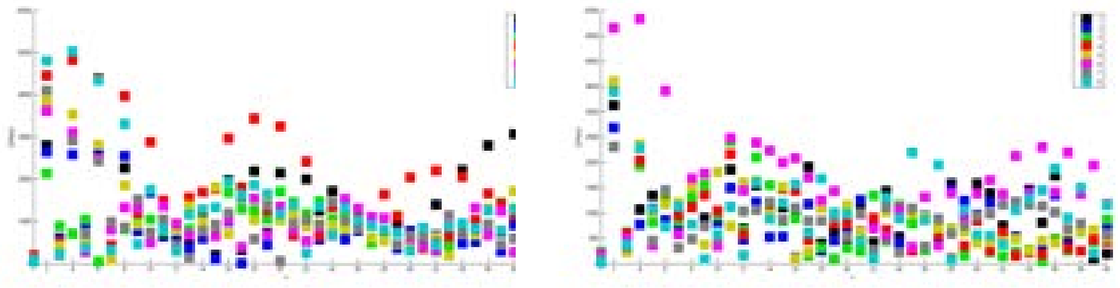

(c) Series 3 - natural series S40.

(d) Series 4 - natural series S27.

Figure 6.19: Estimated order of the image sequence according to each module of an accumulated Zernike moment (where max $n = 40$).

Reducing the number of elements in Zernike moment sequence carries some advantages. It leads to less information to process in further analysis and offers a more general and vague image characteristic. It allows us to relate parts of the image with individual groups of moments since the same modules of Zernike moments in an artificially generated sequence should have similar values. The similarities are the most visible in the Zernike moments of the lower order (up to $n = 4$). Zernike moments of the lower order carry the biggest amount of data out of the information package. However, despite these dependencies, the order in the artificially generated series does not carry over to individual Zernike moments completely.

Therefore, we assume that moments of the lower order reflect the overall characteristic of the image while the moments of the higher order are responsible for a more detailed information. The characteristic depending on the moments of the lower order should show the order of the sequence less accurately. Using more moments of the higher order should let us approach the correct order in the series.

The sum of Zernike moments is calculated as follows

$$S_{nm} = \sum_{i=1}^{n} \sum_{j} A_{ij} \quad \text{where } j \leq i. \tag{6.16}$$

The sum describes the image with one complex value or a module of that value. While this approach minimizes the number of elements in the descriptor and reduces the amount of data circulating in the calculations, it does carry less distinct information about the image. We assume that the Zernike moments follow the top-down rule when it comes to details in image descriptions. Thus, the moments of the lower order give a more general description of the image like the shape of the object in the image, while the moments of the higher order cover more details from the image.

In this approach we rely on neural networks for matching and sequencing. The maximum order of the Zernike moment in our implementation is 40. All images are pre-processed to reduce background presence. The objects in the images retain their shape and pixel composition while background pixels are "erased" (we change their value to 0).

We use 5 microscope image series that contain various tissue fragments. The series can be described as artificially generated and natural. The artificially generated series comes with known and established order as seen in Figure 6.14 and 6.15. These series are built by slightly modifying the content of subsequent images in the series, imitating the tissue changing between consecutive slides. The natural series do not have a known or pre-established order. There is no way to reliably evaluate the accuracy of the proposed sequence, therefore, we have to rely on visual inspection in such cases. Examples of such series are in Figure 6.16, 6.17 and 6.18.

The purpose of these tests is to establish how useful is the proposed method for the problem of image sequencing and if there are any other potential applications.

Test sets are constructed in a way that allows us to track what position of the image in the sequence shows each module of A_n. We can track how the positions change, and when the global and local points of divergence appear. We test it on two sets of image sequences. The ordered sequence for the artificially generated series serves as the point of reference that provides a valid value of error for the effectiveness of the method. The natural series are used to extrapolate on the actual effectiveness of the method compared to the data gathered for the artificially generated series.

The results are grouped into two types of diagrams. The square-point graph from Figure 6.19 and 6.20 shows the position of each image in the sequence according to each element A_n of the accumulated Zernike moment descriptor. Figure 6.21, 6.22 and 6.23 contain the estimated order of the sequence for each image series. The graphs showing distribution of A_n modules are constructed using the data from the estimated sequences.

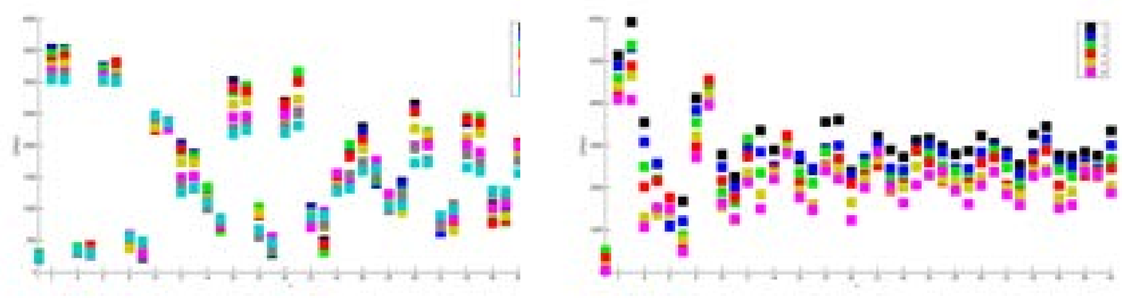

(a) Series 1 - ordered series S40.

(b) Series 2 - ordered series S5.

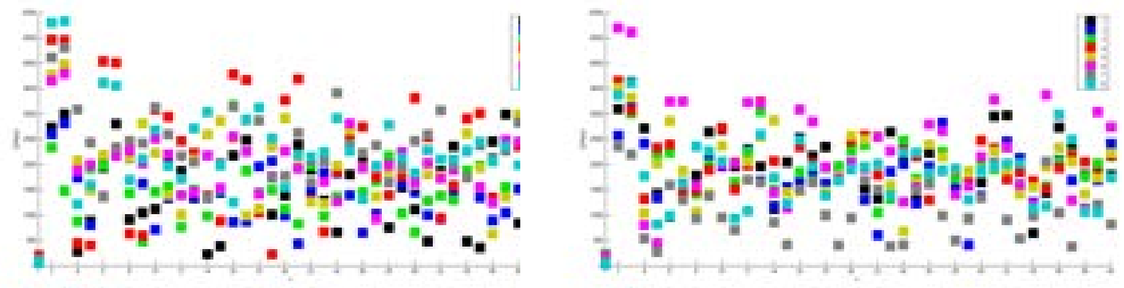

(c) Series 3 - unordered series S40.

(d) Series 4 - unordered series S27.

Figure 6.20: The distribution of modules of accumulated Zernike moments ($n = 40$) in ordered sequences.

In summary, the characteristic built out of Zernike moments of the lower order delivers lower rates of accuracy. The output sequence diverges from the actual order of the images in the microscope series. It is especially visible in the case of image series of which we know the actual order of (Figure 6.14 - 6.15). Adding

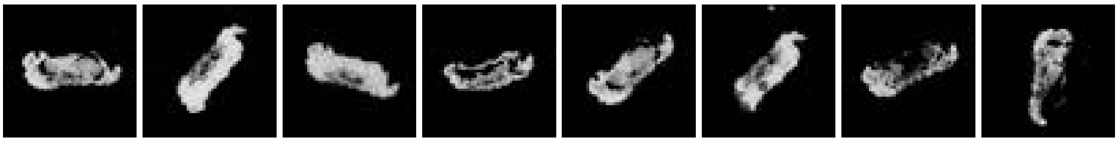

D G H A E F B C

Figure 6.21: The ordered sequences of image series S40 (series #3) as estimated by accumulated Zernike moments ($n = 40$).

F B E D C A H G

Figure 6.22: The ordered sequences of image series S27 (series #4) as estimated by accumulated Zernike moments ($n = 40$).

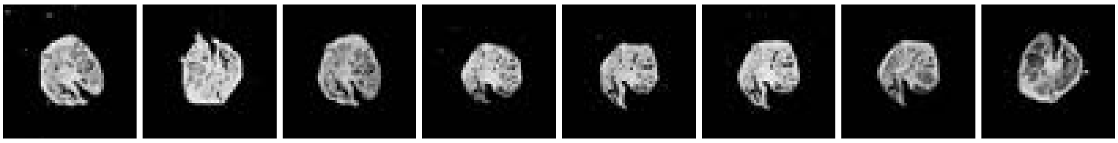

G E H A C D B F

Figure 6.23: The ordered sequences of image series S102 (series #5) as estimated by accumulated Zernike moments ($n = 40$).

more Zernike moments with higher order n results in more accurate estimates. Thus, it is possible to estimate quite closely an actual order of the sequence using a set of Zernike moments of adequately high orders. We can see these properties in Figure 6.20, where the values of modules of A_n of neighboring images from the sequence lay closely to each other.

On the basis of these conclusions, we can say that images containing similar objects share similarities in the distribution of accumulated Zernike moments in the characteristics. Therefore, this type of image characteristic can serve as a useful tool in problems that center on finding similarities between images, e.g. classification. In the proposed method, similarities are most visible between the module values of moments of lower order. These are the moments that describe the general shape of the object. Because of that we can group images into classes using these values alone. Such generalization of images groups allows us to calculate a general characteristic of the group as presented in Figure 6.24. We can see that the averaged values of modules of A_n form patterns that are distinct from each other.

In conclusions, descriptors using modules of accumulated Zernike moments allow us to construct image characteristics that may be used to detect similarities between images. Likewise, they can also be used to differentiate between images, making them a tool in classification problems. Modules of moments of lower orders are more stable than those of higher orders. Which means that for two similar images the differences between the values of modules are less prominent in the modules of lower orders, and more pronounced in the modules of higher orders which are responsible for more detailed description of the image. By choosing to focus on macro- or micro-differences, reflected by Zernike moments of lower and higher orders respectively, we can control the accuracy threshold of the descriptor.

As the results show, this approach is a valid candidate to solving the problem of image sequencing of microscope image series as presented. In the proposed approach the order of the sequence is estimated on the basis of the most resemblance between the modules of moments. According to this criterion, the more similar are objects in the image, the better the match. This approach is easily modifiable as we can choose the level of accuracy of the descriptors by selecting the order of moments or by using more complex methods like assigning weights to modules in order to stir the algorithm in the desired direction or even use neural networks to process the descriptors as a pattern.

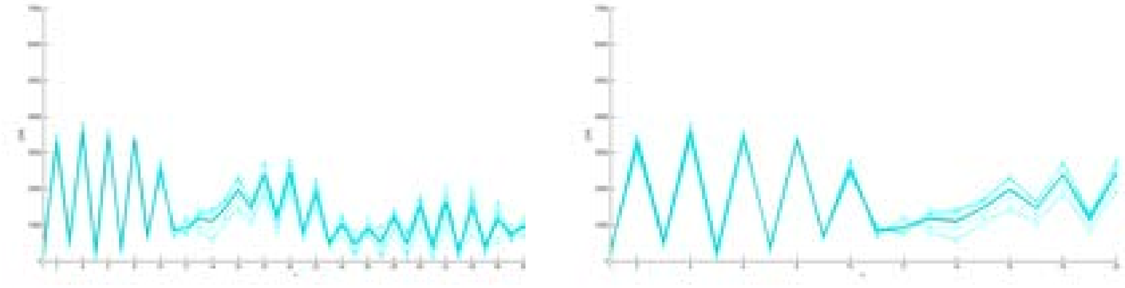

(a) Series 1 - orderded S40

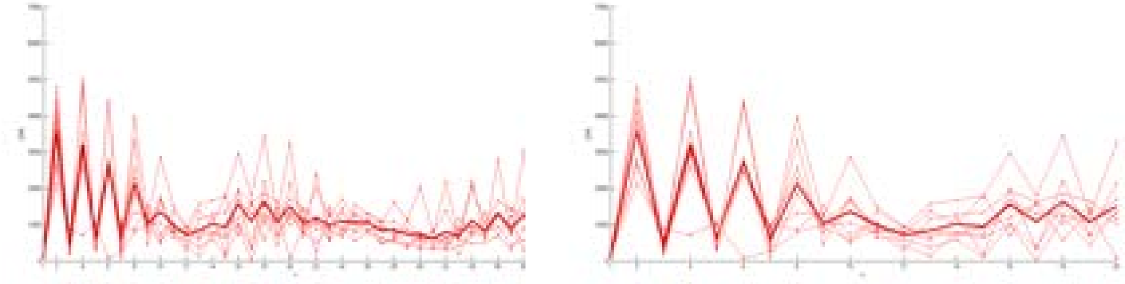

(b) Series 3 - unorderded S40

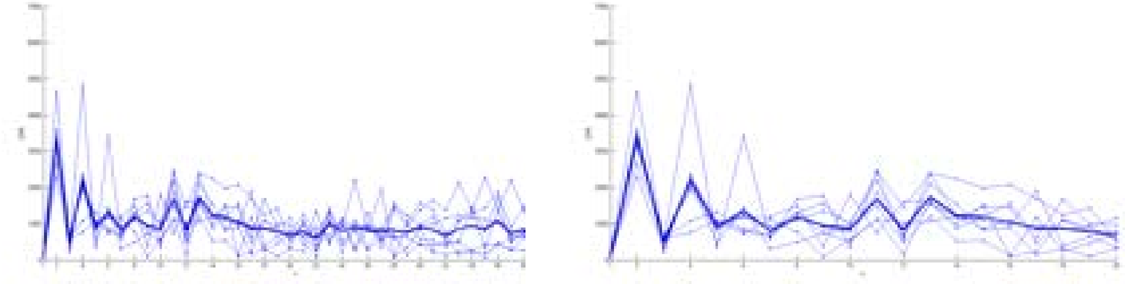

(c) Series 4 - unorderded S27

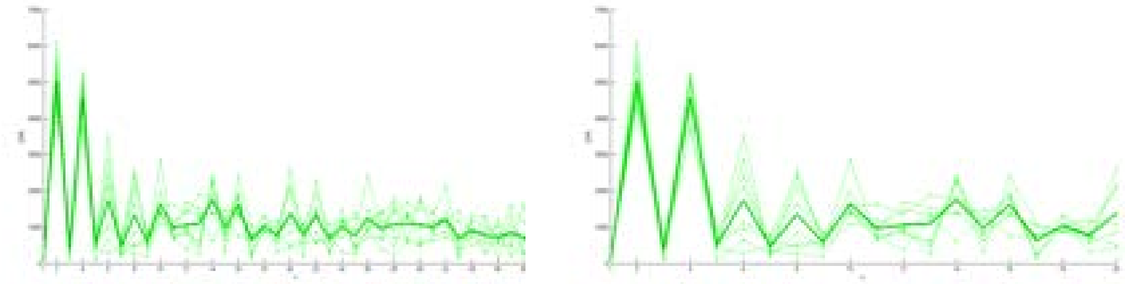

(d) Series 5 - unorderded S102

Figure 6.24: Class characteristics constructed using accumulated Zernike moments. Diagrams contain full characteristics and their close-ups.

Chapter 7

Practical Application of Zernike Moments in Microscope Image Analysis

This chapter follows on the application of Zernike moment-based image descriptors. Its scope covers image registration problems other than image sequencing from the previous chapter. We can include in these new problems various types of classification, identification, recognition and detection problems in microscope images. The proposed Zernike moment-based descriptor is the main component in all presented applications.

Most microscope images carry huge amount of information that is essential in common diagnostics as well as in pathology [128], [118]. The content of the image often consists of elaborate structures in terms of morphology as well as the phenotype of the cells. These properties make up a very complex problem that often demands complex and specialized methods of solution [33].

There are many published papers researching the subject of tissue recognition. In [100], directional fractals and neural networks are used in the analysis and classification of tissue section images of human resistance arteries. In [114], SVM classifier is used to model the derived features to classify the breast tissue density for the purpose of breast cancer research.

The chapter is organized as follows. The first section covers the application of the descriptor in the problem of tissue type recognition. Here, microscope images contain fragments of various types of tissue. This approach relies on building a class descriptor for identification purposes; the evaluation metric is standard MSE. This approach is further explored in the next section, where we use standard classifiers like neural networks and logistic regression to form a multi-classifier tool. The input data for the classifiers is the Zernike moment-based descriptor. In the next section, we replace the multi-classifier with a modified boosting algorithm; the descriptors are still Zernike moment-based. Since most microscope images are of large data format, in the next section, we investigate how the proposed descriptors work with random sampling of data from microscope images and whether it makes the process more robust. Finally, we investigate if the Zernike moment-based descriptor allows us to detect deviations in images for the problem of damage detection in microscope images.

7.1 Scalability of Zernike Moments and Its Application in Classification of Microscope Images

In this section, we explore how scale and size of the image impact the effectiveness of Zernike moment-based image descriptors. This property shall prove useful in future application of this type of descriptors. Both scale and size of the image are important factors in image analysis that can influence the outcome in a major way. This analysis covers such issues as the scalability of Zernike moments, scale-invariance of the moments and whether Zernike moment descriptors can be used to classify objects that differ in scale. In this approach we rely on and utilize the well-known properties of Zernike moments like their orthogonality, invariance and redundancy [62], [86].

We conduct a series of experiments with the purpose to check the effectiveness of Zernike moment-based descriptors. We check the descriptor against microscope images of tissue taken at various levels of magnitude. Furthermore, we check how the actual size of the image impacts the calculations. Finally, we check if the normalization of Zernike moments has any positive influence on the descriptor's capabilities. During the experiments we track the value of the Zernike moment in the descriptor as well as the power of the image.

In the first experiment we use microscope image series of three types of human tissue. The series are numbered in Roman numerals from I to III and contain I - cardiac tissue, II - spindle neuron tissue and III - tendon tissue. Each series includes subsections that are of different level of magnitude. They are further divided into three categories: medium (40X), large (100X) and very large (400X). The X signifies the magnification factor for the actual size of the source tissue. Each series counts 90 images for each level of magnitude which in total makes 270 images (3×90). Some samples for image series I are in Figure 7.1, for series II in Figure 7.2 and for series III in Figure 7.3.

All calculations and sets are done using the module value of Zernike moments. Values of $A_{n,-m}$ could be taken out of the descriptor, because modules $|A_{n,m}| = |A_{n,-m}|$ according to the properties of Zernike moments. The highest order of n in implementation is $n_{max} = 40$, which gives us a sequence of 440 Zernike moments where $m \geq 0$, and the number of accumulated Zernike moments of 40. In computation, we use images of the size of 120px × 120px.

In this experiment, we determine how the size of the objects in the image and how resizing of the image itself impact the values of Zernike moments. The goal is to determine if Zernike moments are scalable and/or are scale invariant. Finally, we test how the scaling of images factors into the problem of classification of tissue types.

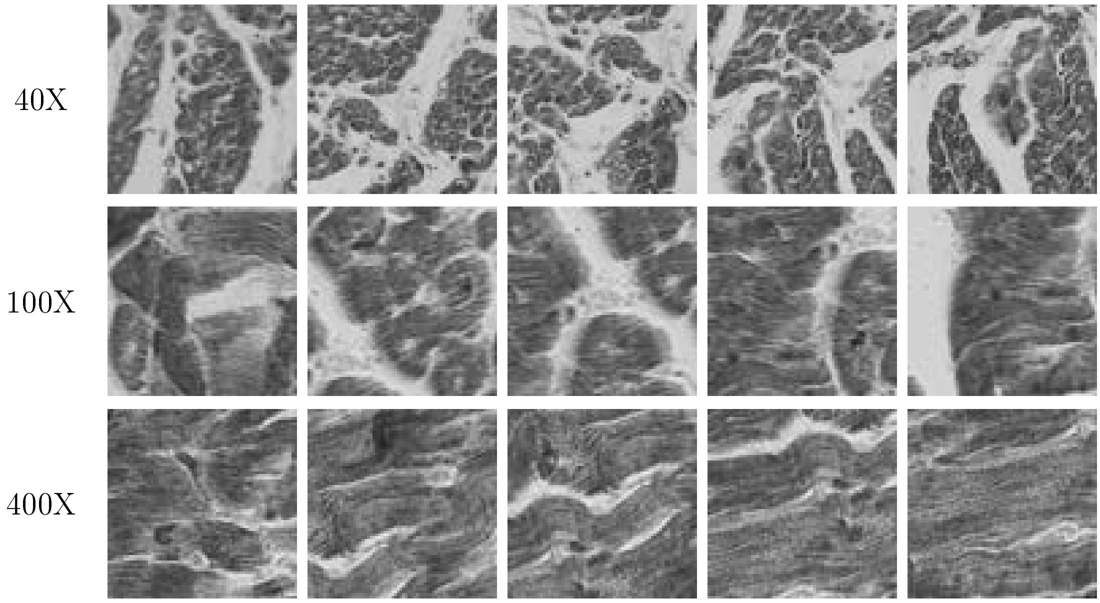

Figure 7.1: Microscope series I containing cardiac tissue at different level of magnitude.

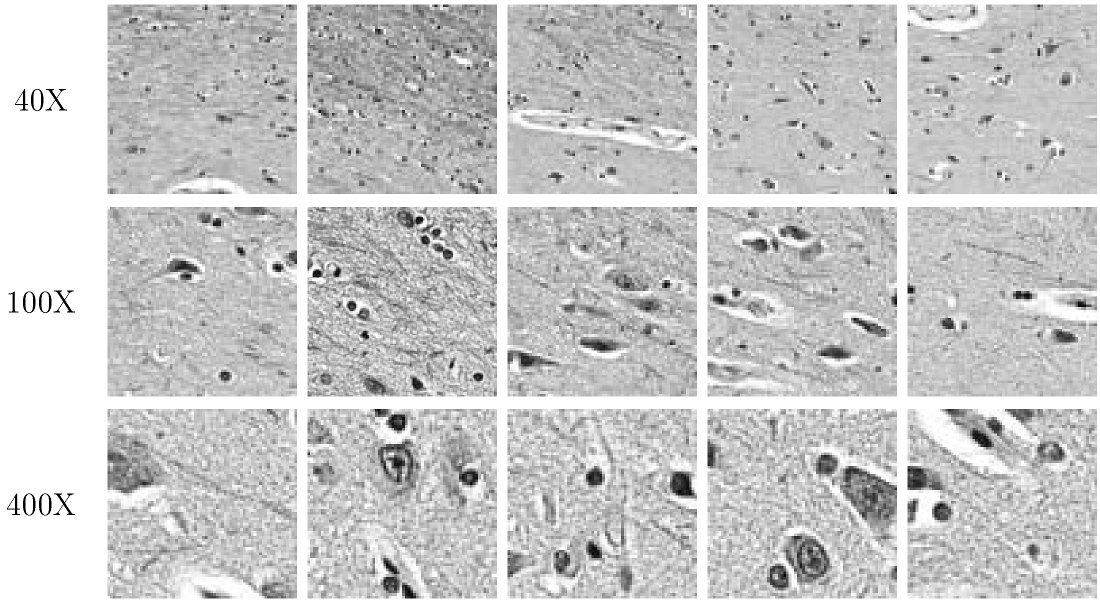

Figure 7.2: Microscope series II containing spindle neurons tissue at different level of magnitude.

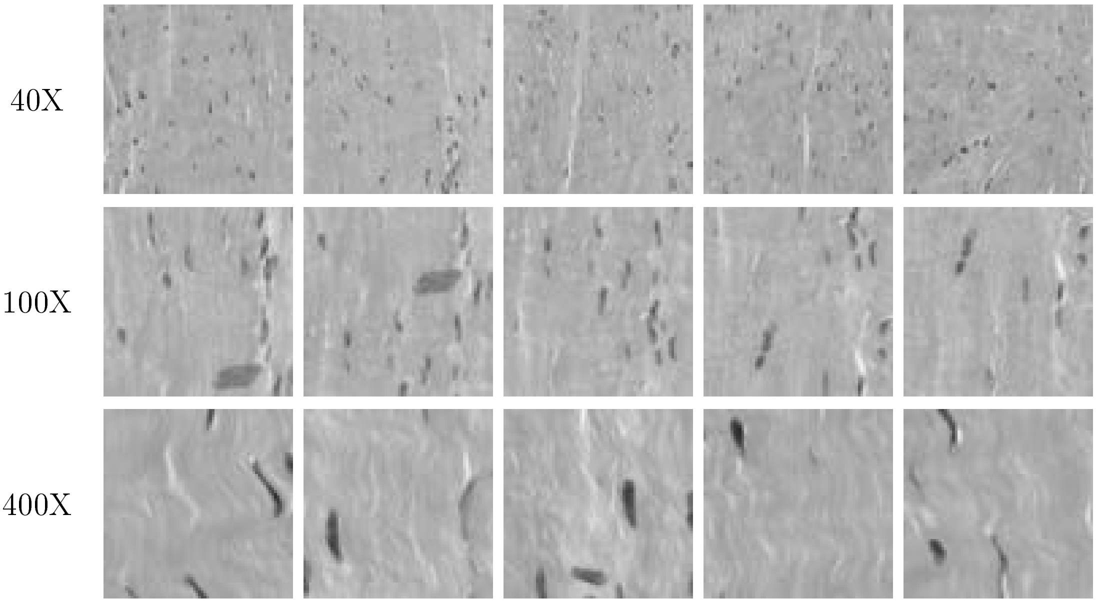

Figure 7.3: Microscope series III containing tendon tissue at different levels of magnitude.

We use a group of test images that depict the same subject, but are of different sizes. Here, the size of the image is 600px, 400px, 200px or 100px. Comparison of square images of every size is shown in Figure 7.4.

We measure how the volume of information changes between each resizing using image power and proportions of image surfaces as the criterion.

Image power is the sum of all pixel values in the image. It informs us of how much information is retained between each resizing. The power of the image (image power, IP) is calculated using two methods. The first one is the overall sum of all pixel values in the image, the second one is the averaged value of all image pixels in the image. The sum is calculated using the formula

$$IP = \sum_{x,y} I(x,y) \tag{7.1}$$

and the averaged value is calculated as follows

$$\overline{IP} = \frac{1}{N \times N} \sum_{x,y} I(x,y). \tag{7.2}$$

The proportion of the image surface is the proportion between the input source image and the derivative output image which is a result of resizing. We assume that this proportion should have similar value for Zernike moments. The surface

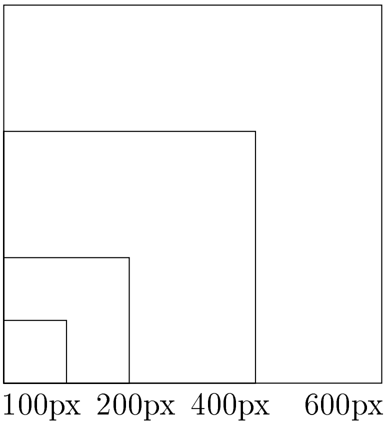

Figure 7.4: Size comparison of square images of sizes 600px, 400px, 200px and 100px.

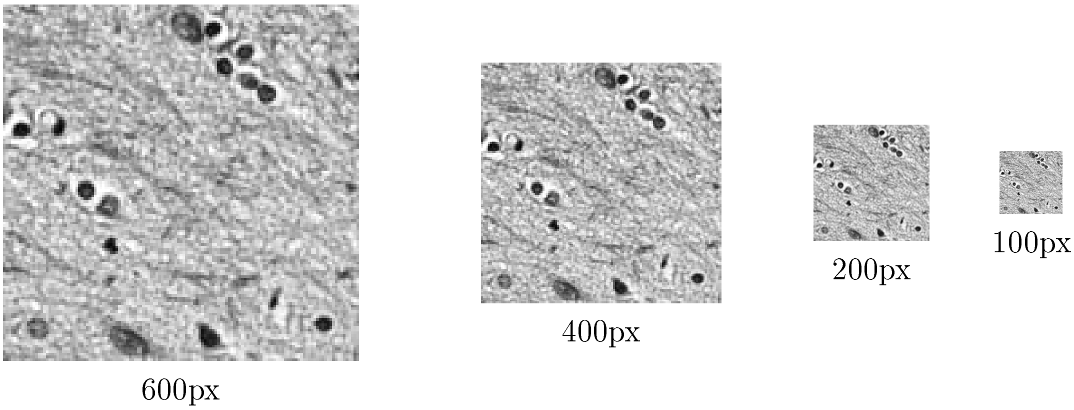
600px
400px
200px
100px

Figure 7.5: Examples of images after scaling

.

image size	**proportion**	**IP (sum)**	**$\overline{\text{IP}}$ (average)**
600px	1.0000	1.6792×10^5	0.4664
400px	0.4444	0.3325×10^5	0.4664
200px	0.1111	0.0209×10^5	0.4662
100px	0.0278	0.0013×10^5	0.4657

Table 7.1: Calculated image power and surface proportion for sample cardiac muscle tissue image (100X).

proportion is defined as

$$S = \frac{N^{(1)} \times N^{(1)}}{N^{(2)} \times N^{(2)}} \approx \frac{A^{(1)}_{nm}}{A^{(2)}_{nm}}, \tag{7.3}$$

where (1) and (2) denote the source image and the derivative image respectively, and N is the size of the image.

If or how the properties of Zernike moments change is tested on microscope images of tissue. Here, we showcase it on the example of two samples. The first image is a cardiac tissue sample. We check how the power of the image changes with the resizing of the image. This data is in Table 7.1. It shows that both the surface proportion and the IP sum change exponentially, but without correlation between them. However, the IP average stays at similar value for the source image and its derivatives. These conclusions and data are used as a point of reference in further computations.

Table 7.2 and 7.3 contain a calculated set of first and last Zernike moments for each image. It shows that the surface proportion is proportionate to the value of Zernike moments of lower order. The correlation weakens with the moments of higher order. This set shows that the value of Zernike moment is scalable to a certain degree and thus scale invariant for certain Zernike moments. The graphic presentation of moments from A_1^1 to A_5^5 is in Figure 7.6, and it shows the scalability of Zernike moments. The same set-up for moments from A_{40}^{20} to A_{40}^{40} is in Figure 7.7. The scalability is not as clear-cut as in the case of moments of the lower orders. The presentation of all calculated Zernike moments is presented in Figure 7.8 and 7.9. It shows that the information is retained throughout all sequences in visible capacity. The calculated data for the sequence of accumulated Zernike moments from A_1 to A_{10} is in Table 7.4. Graphic presentation of this data for moments from A_1 to A_{40} is in Figure 7.10.

To further showcase these properties, the same type of exercises is compiled for another type of tissue. Table 7.5 contains a summary of data of image power for microscope image of spindle neuron tissue. As in previous case, this example shows similar correlation properties for average image power.

image size	**(1,1)**	**(2,0)**	**(2,2)**	**(3,1)**	**(3,3)**	**(4,0)**	**(4,2)**	**(4,4)**	**(5,1)**	**(5,3)**	**(5,5)**
600^2	3739.05	2921.80	2123.09	8338.18	3936.93	3311.50	2659.85	5000.71	672.75	2508.60	2409.01
400^2	1662.03	1302.10	943.02	3704.82	1749.08	1465.80	1182.70	2225.44	298.38	1115.95	1071.98
0.4444	0.4445	0.4456	0.4442	0.4443	0.4443	0.4426	0.4446	0.4450	0.4435	0.4449	0.4450
200^2	415.29	321.97	236.12	926.69	437.18	372.36	295.19	555.69	74.38	279.11	266.55
0.1111	0.1111	0.1102	0.1112	0.1111	0.1110	0.1124	0.1110	0.1111	0.1106	0.1113	0.1106
100^2	103.72	78.59	59.33	232.07	108.87	96.09	73.50	139.72	18.90	70.39	67.91
0.0278	0.0277	0.0269	0.0279	0.0278	0.0277	0.0290	0.0276	0.0279	0.0281	0.0281	0.0282

Table 7.2: Calculated Zernike moments from A_1^1 to A_5^5 for cardiac tissue sample before and after resizing.

image size	**(40,20)**	**(40,22)**	**(40,24)**	**(40,26)**	**(40,28)**	**(40,30)**	**(40,32)**	**(40,34)**	**(40,36)**	**(40,38)**	**(40,40)**
600^2	238.94	1144.61	1194.87	303.04	995.88	735.00	563.15	279.44	868.93	586.24	1007.91
400^2	300.90	502.26	430.80	131.66	482.59	321.60	281.69	113.60	294.35	267.03	578.62
0.4444	1.2593	0.4388	0.3605	0.4345	0.4846	0.4375	0.5002	0.4065	0.3387	0.4555	0.5741
200^2	24.67	132.31	70.90	40.65	107.06	79.30	174.68	35.73	217.48	59.93	72.28
0.1111	0.1033	0.1156	0.0593	0.1341	0.1075	0.1079	0.3102	0.1279	0.2503	0.1022	0.0717
100^2	24.36	37.52	20.76	13.15	26.06	15.39	130.55	10.86	49.59	8.43	45.01
0.0278	0.1019	0.0328	0.0174	0.0434	0.0262	0.0209	0.2318	0.0388	0.0571	0.0144	0.0447

Table 7.3: Calculated Zernike moments from A_{40}^{20} to A_{40}^{40} for cardiac tissue sample before and after resizing.

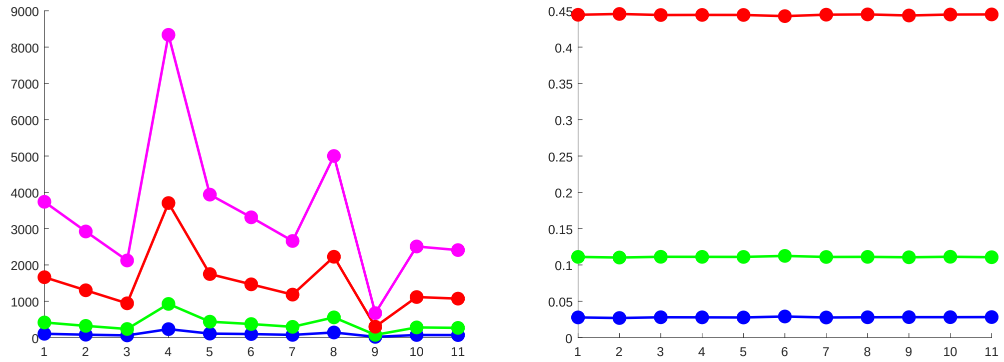

magneta - 600px, *red* - 400px, *green* - 200px, *blue* - 100px

Figure 7.6: Compilation of Zernike moments from A_1^1 to A_5^5 for sample cardiac muscle tissue image. The assigned values are in Table 7.2.

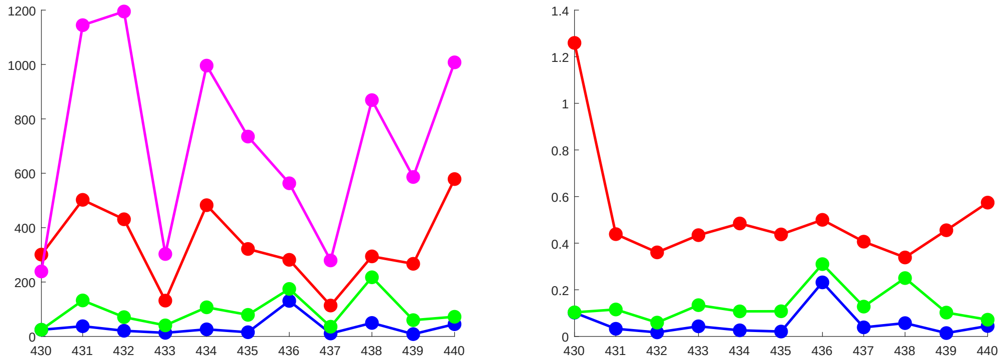

magneta - 600px, ***red*** - 400px, ***green*** - 200px, ***blue*** - 100px

Figure 7.7: Compilation of Zernike moments from A_{40}^{20} to A_{40}^{40} for sample cardiac muscle tissue image.The assigned values are in Table 7.3.

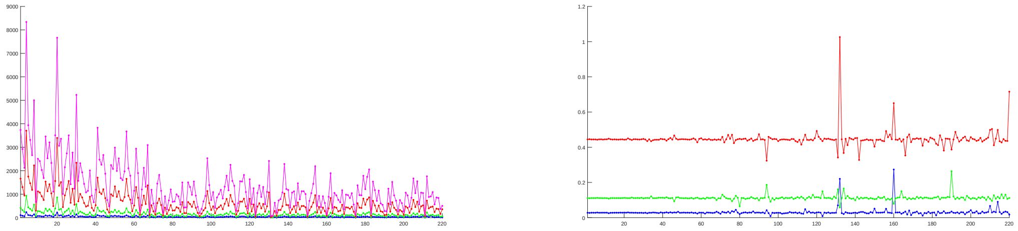

magneta - 600px, ***red*** - 400px, ***green*** - 200px, ***blue*** - 100px

Figure 7.8: Compilation of first 220 out of 440 Zernike moments for sample cardiac muscle tissue image.

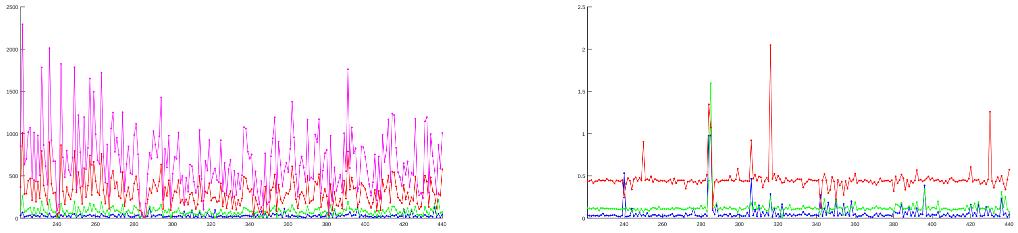

magneta - 600px, ***red*** - 400px, ***green*** - 200px, ***blue*** - 100px

Figure 7.9: Compilation of last 220 out of 440 Zernike moments for sample cardiac muscle tissue image.

rozmiar	**A(1)**	**A(2)**	**A(3)**	**A(4)**	**A(5)**	**A(6)**	**A(7)**	**A(8)**	**A(9)**	**A(10)**
600^2	208.88	3739.05	4944.34	12221.36	8601.01	2747.96	8124.04	1249.80	11945.46	2322.65
400^2	94.29	1662.03	2200.55	5429.77	3827.20	1223.09	3606.83	558.81	5305.92	1033.10
0.4444	0.4514	0.4445	0.4451	0.4443	0.4450	0.4451	0.4440	0.4471	0.4442	0.4448
200^2	22.52	415.29	546.96	1357.83	958.80	304.74	898.64	139.75	1343.86	256.28
0.1111	0.1078	0.1111	0.1106	0.1111	0.1115	0.1109	0.1106	0.1118	0.1125	0.1103
100^2	4.54	103.72	135.11	339.46	245.52	77.02	218.85	35.20	343.83	65.34
0.0278	0.0218	0.0277	0.0273	0.0278	0.0285	0.0280	0.0269	0.0282	0.0288	0.0281

Table 7.4: Calculated accumulated Zernike moments from A_1 to A_1 for a sample cardiac muscle tissue image.

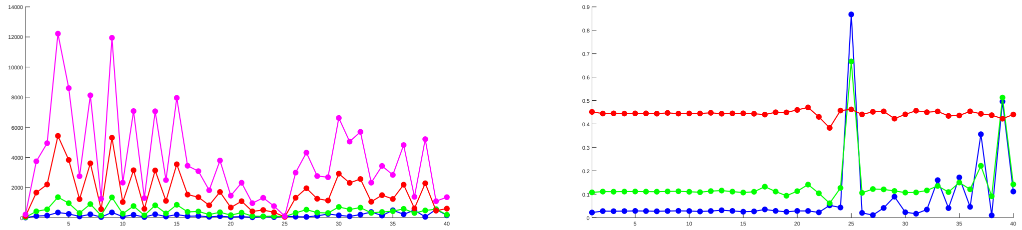

magneta - 600px, ***red*** - 400px, ***green*** - 200px, ***blue*** - 100px

Figure 7.10: Graphic presentation of accumulated Zernike moments data from A_1 to A_{40} for sample cardiac muscle tissue image.

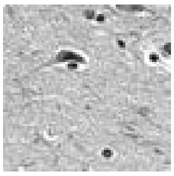

image size	**proportion**	**IP (sum)**	**IP (average)**
600px	——	2.6676 $\times 10^5$	0.7410
400px	0.4444	0.5283 $\times 10^5$	0.7410
200px	0.1111	0.0333 $\times 10^5$	0.7410
100px	0.0278	0.0021 $\times 10^5$	0.7415

Table 7.5: Calculated image power and surface proportion for sample spindle neurons tissue image (100X).

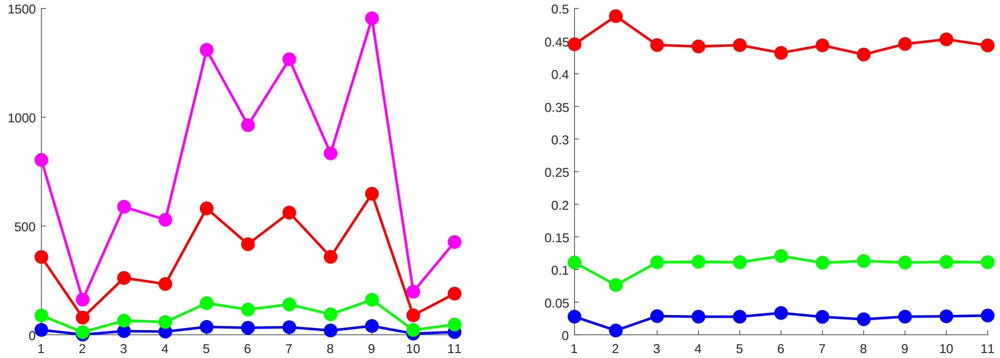

magneta - 600px, ***red*** - 400px, ***green*** - 200px, ***blue*** - 100px

Figure 7.11: Compilation of Zernike moments from A_1^1 to A_5^5 for sample spindle neurons tissue image.

The next set contains calculated edge Zernike moments of the sequence for the image. Moments A_1^1 to A_5^5 are in Figure 7.11 and moments A_{40}^{20} to A_{40}^{40} are in Figure 7.12. The sequences express similar pattern to the previous sequences. The more broad compilation of Zernike moment sequence is in Figure 7.13 and 7.14. Finally, the accumulated Zernike moment sequence is in Figure 7.15. Compared to the previously presented sequence, there are more divergences, but the proportion follows a semi-constant pattern bar few exceptions.

To mitigate the differences that come from the differing levels of scaling in the images we use normalization. The purpose of the normalization process is to equalize the proportion factor between images of different sizes. We use a standard normalization process adjusted to the Zernike moment sequence

$$\overline{A}_{nm} = \frac{A_{nm} - \min_{n,m} A_{nm}}{\max_{n,m} A_{nm} - \min_{n,m} A_{nm}} \tag{7.4}$$

. The normalization of Zernike moments aims to eliminate the differences that come from varying sizes of input images.

To show the effects of normalization we reuse previous two examples. The first table contains the calculated image power for a random sample of cardiac muscle tissue (Table 7.1), the second table contains the same data for a sampled image of spindle neurons tissue (Table 7.5). The normalized Zernike moments from A_1^1 to A_5^5 and from A_{40}^{20} to A_{40}^{40} for sample cardiac muscle tissue are in Figure 7.16. The same data for sample spindle neurons tissue is in Figure 7.17. The compilation of the sequence of normalized Zernike moments for cardiac muscle sample is in Figure 7.18. It also contains the calculated difference between concurrent Zernike moments values to provide some means to evaluate the effectiveness of

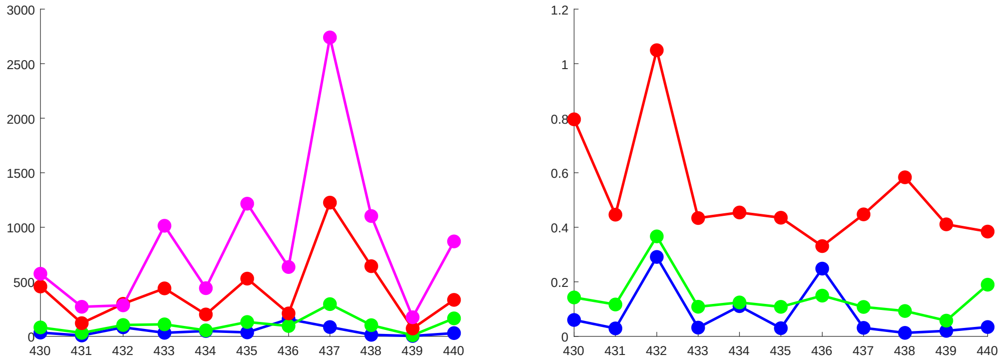

magneta - 600px, ***red*** - 400px, ***green*** - 200px, ***blue*** - 100px

Figure 7.12: Compilation of Zernike moments from A_{40}^{20} to A_{40}^{40} for sample spindle neurons tissue image.

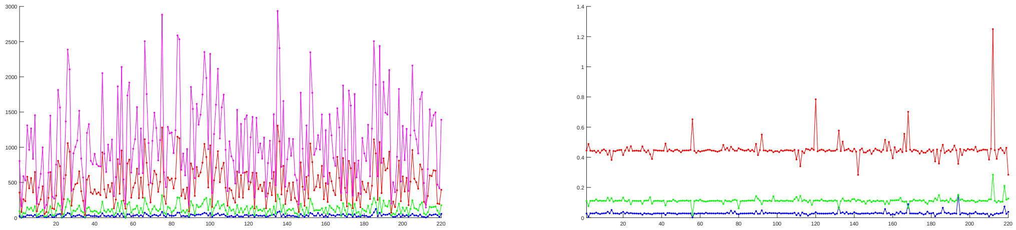

magneta - 600px, ***red*** - 400px, ***green*** - 200px, ***blue*** - 100px

Figure 7.13: Compilation of first 220 out of 440 Zernike moments for sample spindle neurons tissue image.

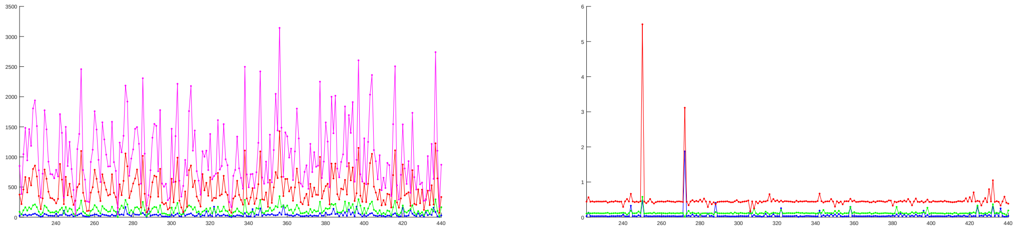

magneta - 600px, ***red*** - 400px, ***green*** - 200px, ***blue*** - 100px

Figure 7.14: Compilation of last 220 out of 440 Zernike moments for sample spindle neurons tissue image.

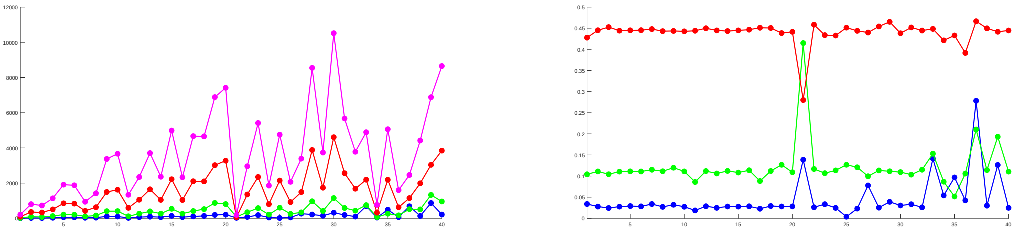

magneta - 600px, ***red*** - 400px, ***green*** - 200px, ***blue*** - 100px

Figure 7.15: Graphic presentation of accumulated Zernike moments data from A_1 to A_{40} for sample spindle neurons tissue image.

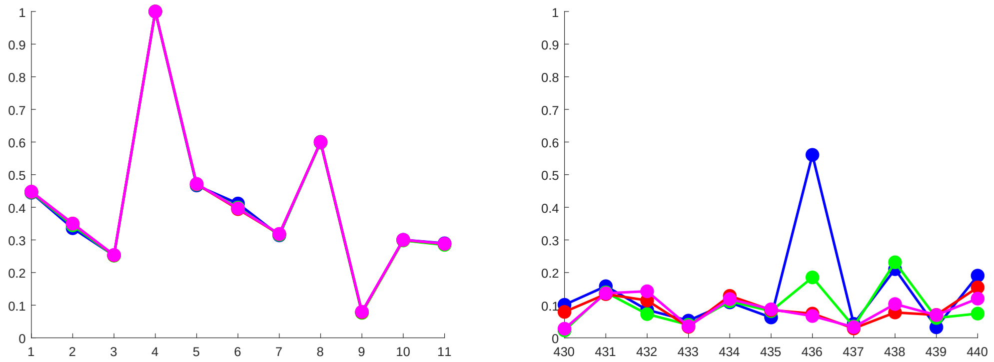

magneta - 600px, ***red*** - 400px, ***green*** - 200px, ***blue*** - 100px

Figure 7.16: Compilation of normalized Zernike moments from A_1^1 to A_5^5 and from A_{40}^{20} to A_{40}^{40} for sample cardiac muscle tissue image. The related values are in Table 7.1.

the normalization process. Similar compilation for spindle neurons tissue is in Figure 7.19. The influence of normalization on accumulated Zernike moments for cardiac muscle tissue is presented in Figure 7.20. The differences between concurrent accumulated Zernike moment values for images after resizing are also there. The same presentation for spindle neurons tissue is in Figure 7.21.

In this part we build characteristics of selected tissue series. The characteristics are devised using unmodified and accumulated Zernike moment sequences. For comparison purposes these sequences are normalized to allow a more accurate profile of the tissue type. We reserved three types of tissue for this experiment at three different levels of magnification: intermediate (40X), high (100X) and very high (400X). The three types of tissue are cardiac muscle (Figure 7.1), spindle neurons (Figure 7.2) and tendon (Figure 7.3). The presentation of Zernike moments before and after normalization for Series I is in Figure 7.22, the accumu-

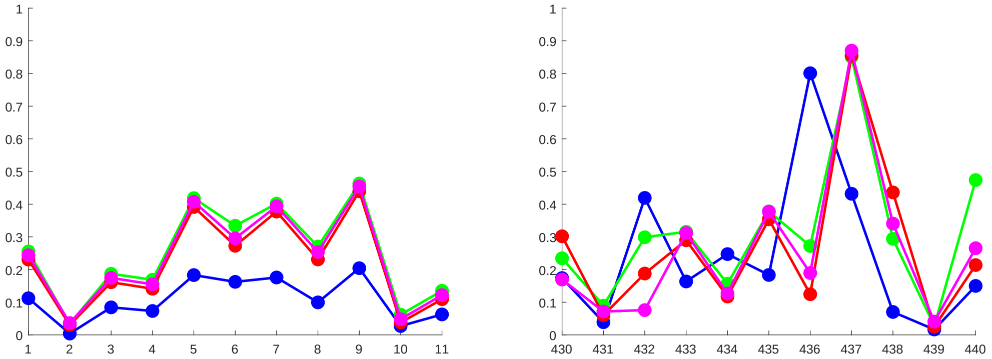

magneta - 600px, ***red*** - 400px, ***green*** - 200px, ***blue*** - 100px

Figure 7.17: Compilation of normalized Zernike moments from A_1^1 to A_5^5 and from A_{40}^{20} to A_{40}^{40} for sample spindle neurons tissue image. The related values are in Table 7.5.

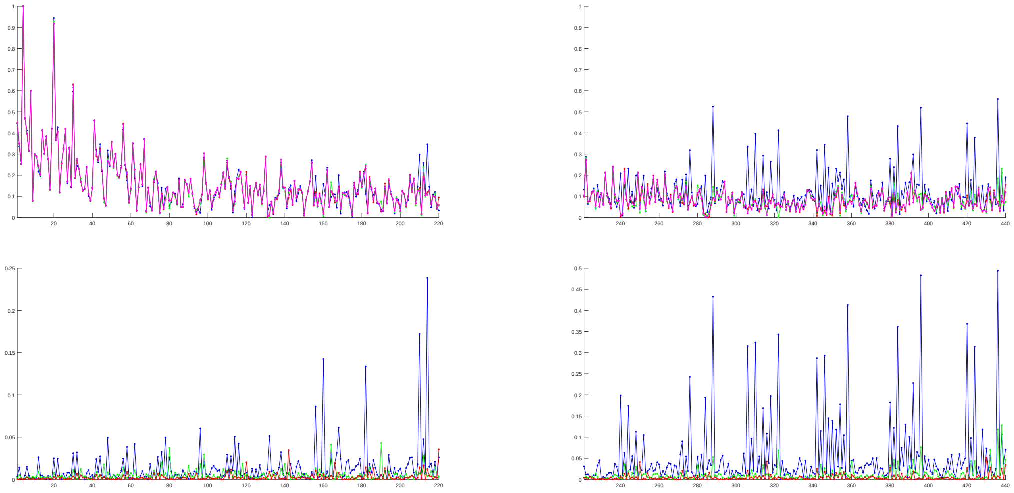

magneta - 600px, ***red*** - 400px, ***green*** - 200px, ***blue*** - 100px

Figure 7.18: Compilation of first 220 out of 440 normalized Zernike moments with their differences for sample cardiac muscle tissue image of various sizes.

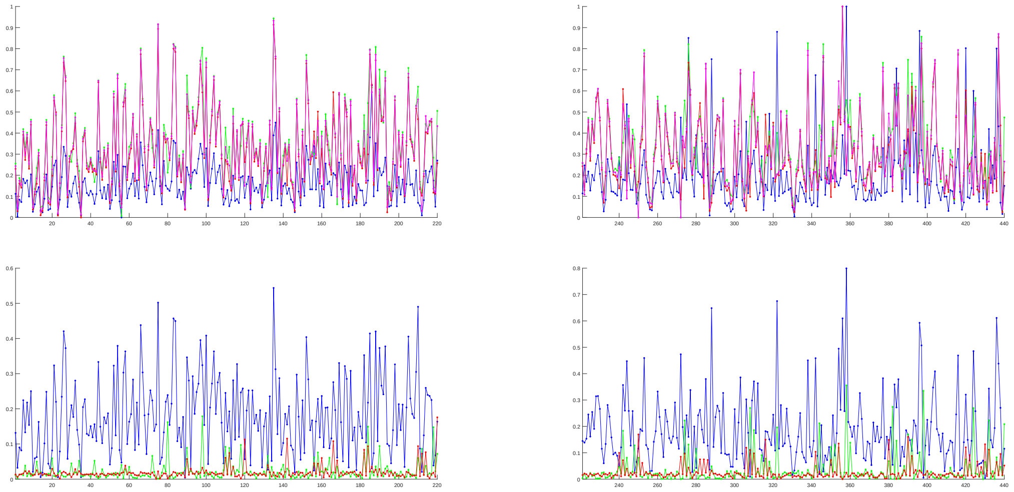

magneta - 600px, ***red*** - 400px, ***green*** - 200px, ***blue*** - 100px

Figure 7.19: Compilation of last 220 out of 440 normalized Zernike moments with their differences for sample spindle neurons tissue image of various sizes.

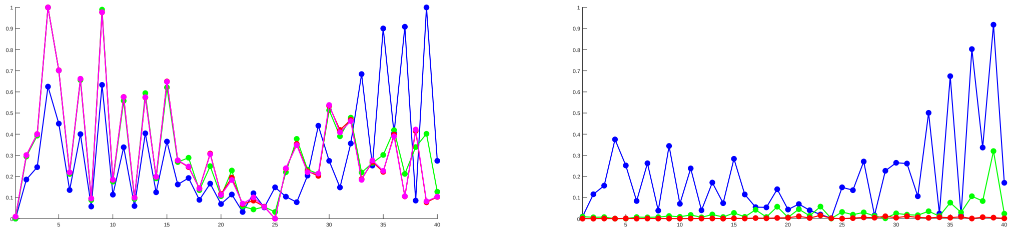

magneta - 600px, ***red*** - 400px, ***green*** - 200px, ***blue*** - 100px

Figure 7.20: Graphic presentation of accumulated Zernike moments data from A_1 to A_{40} after normalization for sample cardiac muscle tissue image.

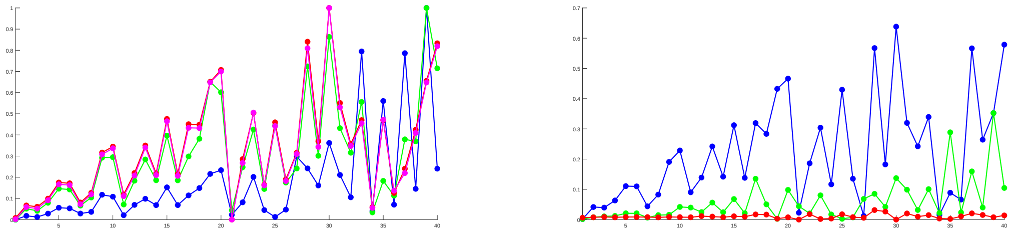

magneta - 600px, ***red*** - 400px, ***green*** - 200px, ***blue*** - 100px

Figure 7.21: Graphic presentation of accumulated Zernike moments data from A_1 to A_{40} after normalization for sample spindle neurons tissue image.

before normalization

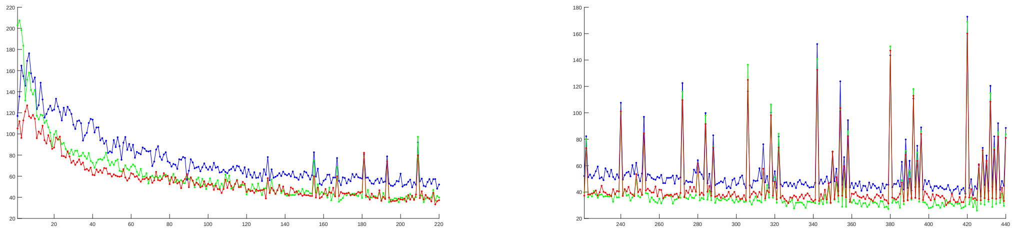

after normalization

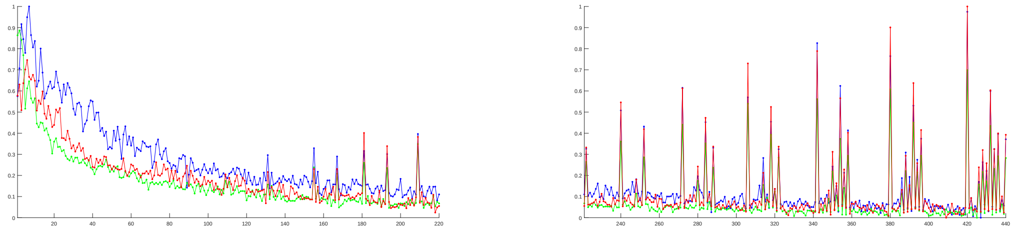

magneta - 600px, ***red*** - 400px, ***green*** - 200px, ***blue*** - 100px

Figure 7.22: Compilation of all 440 Zernike moments before and after normalization for Series I (cardiac muscle tissue).

lated Zernike moment sequence before and after normalization is in Figure 7.23. For Series II, the similar presentations are in Figure 7.24 and 7.25, for Series III, in Figure 7.26 and 7.27.

On the basis of those experiments, we come to a few conclusions. Image resizing affects the value of a Zernike moment. This dependency is proportional and makes Zernike moments scalable proportionally to the value of resizing. Image resizing does not seem to affect Zernike moments of lower orders in a major capacity. More deviations appear in Zernike moments of higher orders (that have the most potential to be laden with numeric error on itself). There is no defined bottom threshold for the scaling factor.

The proposed classification uses the preceding analysis as the point of reference. The proposed classification algorithm is a combination of well-known classification algorithms and sequences of Zernike moments. The sequence is used to build a numerical descriptor of the image (a pattern). In this approach, image classification is performed using sequences of Zernike moments as the input data.

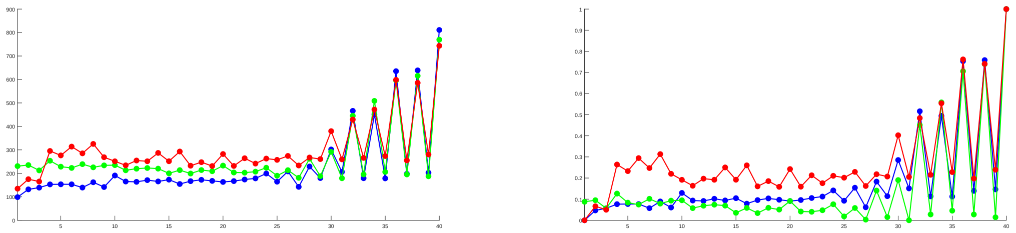

magneta - 600px, ***red*** - 400px, ***green*** - 200px, ***blue*** - 100px

Figure 7.23: Graphic presentation of accumulated Zernike moments data before and after normalization for Series I (cardiac muscle tissue).

before normalization

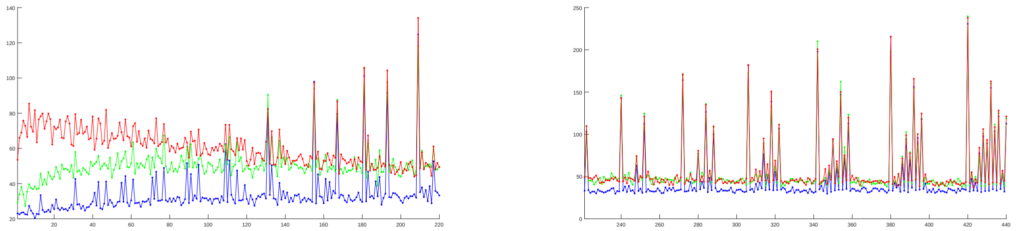

after normalization

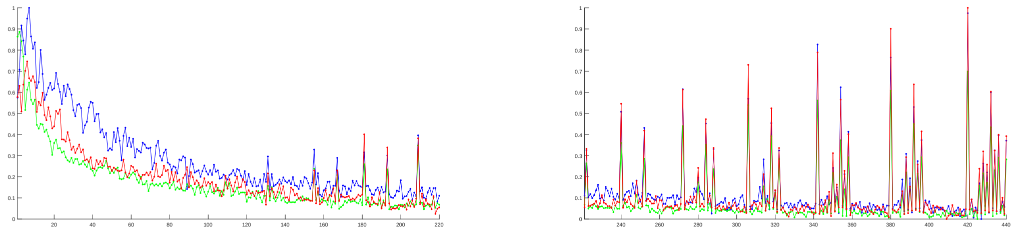

magneta - 600px, ***red*** - 400px, ***green*** - 200px, ***blue*** - 100px

Figure 7.24: Compilation of all 440 Zernike moments before and after normalization for Series II (spindle neurons tissue).

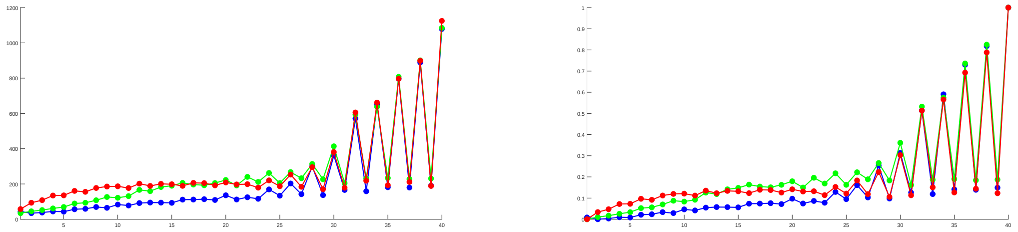

magneta - 600px, ***red*** - 400px, ***green*** - 200px, ***blue*** - 100px

Figure 7.25: Graphic presentation of accumulated Zernike moments data before and after normalization for Series II (spindle neurons tissue).

before normalization

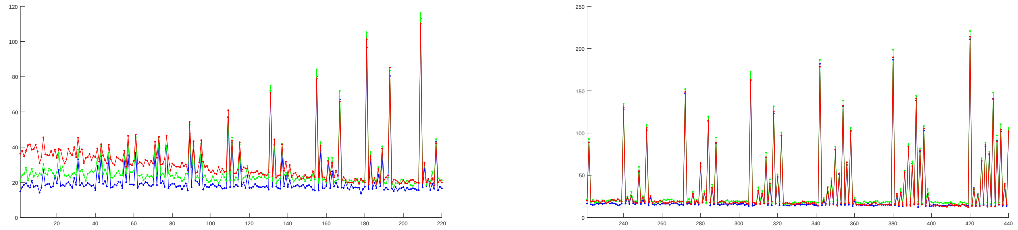

after normalization

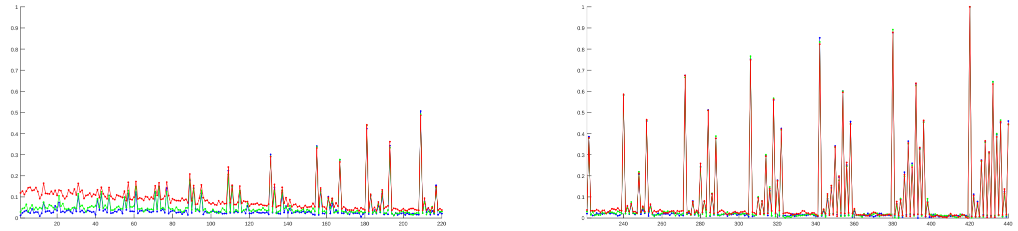

magneta - 600px, ***red*** - 400px, ***green*** - 200px, ***blue*** - 100px

Figure 7.26: Compilation of all 440 Zernike moments before and after normalization for Series III (tendon tissue).

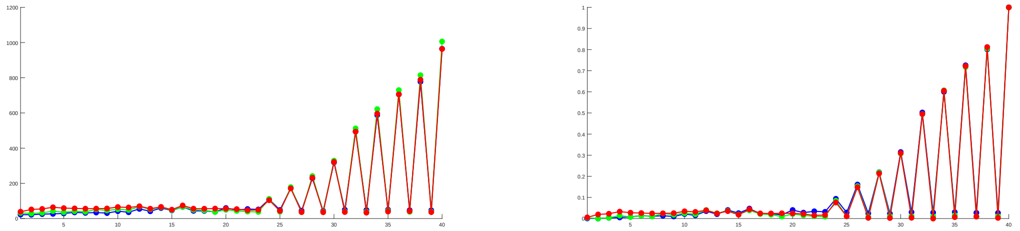

magneta - 600px, ***red*** - 400px, ***green*** - 200px, ***blue*** - 100px

Figure 7.27: Graphic presentation of accumulated Zernike moments data before and after normalization for Series III (tendon tissue).

Three types of classifiers are used in this method: class profiles and MSE (CP+MSE), neural networks (NN, own implementation) and neural networks (NN, from *Matlab* toolbox). The computing environment for all algorithms is *Matlab*.

There are two methods of building a classification model in these experiments. The first case is a training set built out of images of varying level of magnification. The second is a training set that consists only of images of the same magnification level. In this case the testing set is built out of images of the other two levels of magnification. Each approach is tested in a set-up designed for it.

In the classification process itself we use patterns of the accumulated Zernike moments (AZM). The training set consists of 50% of available images, the rest is put in the testing set. In the second set-up, the training set consists of images at the very high level of magnification (400X). It is 90 images in total. As the measure of accuracy/effectiveness of the classification we use a simple percent metric

$$\frac{\#\text{ correctly classified images}}{\#\text{ images}}. \tag{7.5}$$

The classification results for the first set-up are in Table 7.6. The table is organized by the type of classifier and the test case. The results for each case are calculated according to (7.5). The results fall into 80% to 96% range in terms of correctly classified samples. This proves that AMZ sequences can be used as classification patterns in these types of problems. The benefit of this approach is the lessened computation effort since AMZ vectors consists of only 40 components.

The classification results for the second set-up are in Table 7.7. In this case the results are less promising. The classification results oscillate around 80% mark for CP+MSE classifier. For neural networks the results are less than optimal and stay in the 53% to 63% accuracy bracket. Using only one set of images as a testing set proves to be inefficient. It quite negatively impacts the results for both NN methods. It is a major change compared to the first classification approach. No further testing is carried in this direction.

Classifier	**TC #1**	**TC #2**	**TC #3**	**TC #4**	**TC #5**
CP+MSE	0.8321	0.8469	0.8543	0.8568	0.8469
NN	0.9259	0.9506	0.9556	0.9580	0.9605
NN (*Matlab*)	0.8049	0.9111	0.9160	0.9012	0.8938

Table 7.6: Results of classification for the first type of method, where the training set consists of images of varying levels of magnification (40X, 100X, 400X).

Classifier	**TC #1**	**TC #2**	**TC #3**	**TC #4**	**TC #5**
CP+MSE	0.8346	0.8346	—	—	—
NN	0.5630	0.5358	0.5407	—	—
NN (matlab)	0.5679	0.6099	0.6395	—	—

Table 7.7: Results of classification for the second type of method, where the training set consists of images of a single level of magnification (400X).

In this study we reach a few conclusions. Firstly, resizing image impacts the numeric values of Zernike moments as the pool of data changes its volume accordingly. Zernike moments turn out to be scalable proportionally to the surface area of the image. The value of a Zernike moment can be rescaled when the sizes of the original and descendant images are known. Normalization of values of Zernike moments allows us to eliminate the difference in values of moments originating from image samples of different sizes. Zernike moments of lower orders are more robust and scale invariant than Zernike moments of higher orders. The differences for Zernike moments of higher order are much more difficult to eliminate. The analysis does not cover the change of scale only for objects in the image, only the case of the entire image scaling. Both Zernike moments and accumulated Zernike moments can be used in these types of classification problems. The additional property of scale invariance can prove useful in the case of microscope tissue images taken at various levels of magnitude.

7.2 Tissue Type Identification in Microscope Images Using Zernike Moments with MSE Deciding Criterion

This section covers the method of solution of the problem of identification of tissue types on the basis of tissue samples. In this approach we rely on accumulated Zernike moments. Image samples come from various regions of the tissue. Multiple image samples make up a collection of images of a tissue type (an atlas). The goal is to have a general method of identification of various types of tissue. The method should not be restricted to a single tissue image or a collection of a tissue type. It should be applicable to a wide spectrum of different types of tissue. The difficulty arises from sample images that appear not to share a lot in common and are hard to identify, especially "at first glance". These issues need to be addressed when building an algorithm for general identification of the tissue type. The method should be able to identify the tissue type regardless of the innate diverse structure of that tissue. It should also take into account that sample images may contain fragments of the tissue that differ in terms of structure and intensity ([33], [128]).

As in the previous cases, this time we also rely on Zernike moment descriptors as the main tool in this classification problem. Zernike moments and other moments have a history of application in various image identification problems [7]. We also happened to publish a paper on the subject of image classification with the use of Zernike moments [40].

For this problem our database consists of multiple image samples that originate from microscope images of different types of tissue. The test images are prepared using a full microscope image of a tissue as a source material. The samples are picked at random across the entire image. The process is depicted in Figure 7.28 and examples of various such samples that showcase the great variation of the tissue matter are in Figure 7.29. We use multiple microscope images of one type of tissue to build a sample database of that tissue type.

We differentiate four classes of tissue types. The samples for each class are selected at random and come from at least two different preparations of a given tissue type. Such approach allows us to have a very diversified sample group that depicts the same type of tissue. It is needed to properly calibrate the recognition algorithm and show the properties of the method. The examples of samples that are used in this experiment are in Figure 7.30.

We can classify the problem of tissue recognition as a subcategory of classification. The main goal is the construction and calibration of a classifier that allows us for identification of the tissue type in the image. The middle goal is to define a criterion that allows us to recognize the type of the tissue in the image. Such criterion is called the main reference pattern (MRP) and describes the given type

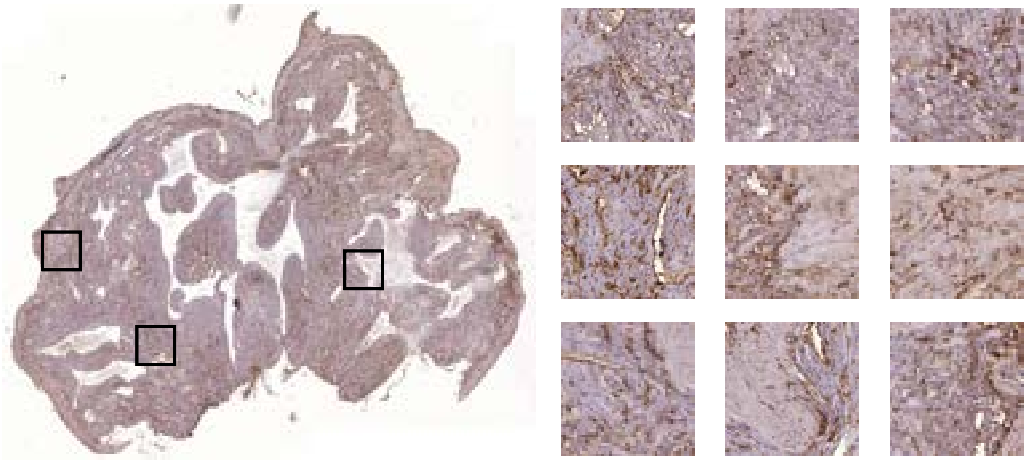

Figure 7.28: Illustration of the sampling process for a tissue preparation and examples of samples that come from such image.

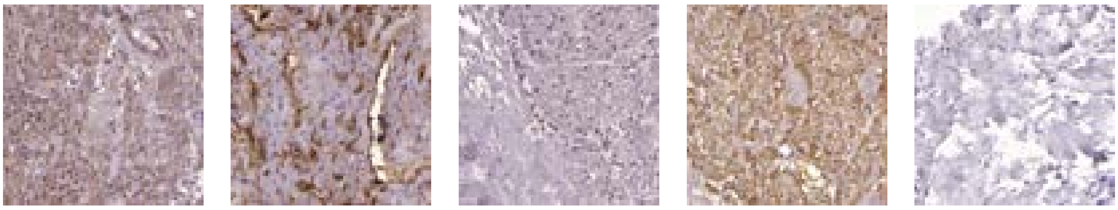

Figure 7.29: Some tissue samples that are used in the experiments. The samples are picked at random from the source image. Multiple source images are used to create the sample database.

Collection S5 → Class 1

Collection S27 → Class 2

Collection S40 → Class 3

Collection S102 → Class 4

Figure 7.30: Samples from each tissue collection that is used in the experiments. There are four collections available.

of tissue. The main reference pattern is constructed on the basis of sample images that come in a training set.

The image descriptor for each tissue sample as well as the main reference patterns for each tissue collection is constructed with Zernike moments. We further refer to such pattern as a descriptor. Each descriptor is different and linked to a particular sample. Therefore, it can serve as an identifier of sorts for the image. The main descriptor is a characteristic of a group profile of images that undisputedly describes a tissue type or a class. The classification process is run based on the calculated image descriptors.

The descriptor is constructed using the formula from (4.6). The core of the descriptor is a Zernike moment and the formula is presented as

$$\{|A_1|, |A_2|, |A_3|, \ldots, |A_N|\}, \tag{7.6}$$

where A_i is an accumulated Zernike moment of order i and N is the maximum order of a Zernike moment in the sequence.

The descriptor from (7.6) is an ordered sequence of modules of accumulated Zernike moments which serves as the identifier of the image. Additionally, the sequence is normalized to the $[0, 1]$ range in order to minimize the influence of varying intensity levels between images. Examples of descriptors of samples from each collection are shown in Figure 7.31. The difference between a normalized and unmodified image descriptor can be viewed in Figure 7.32.

The main class descriptor is calculated according to formula

$$\{ \quad \frac{1}{n}\sum_{i=1}^{n}|A_1^i|, \quad \frac{1}{n}\sum_{i=1}^{n}|A_2^i|, \quad \ldots \quad \frac{1}{n}\sum_{i=1}^{n}|A_N^i| \quad \} \tag{7.7}$$

where n is the sample size of the training set. The main descriptor provides a distinctive pattern that is exclusive to one type of tissue (class of tissue). This characteristic can serve as an identification profile of a class. We construct it using samples from the training set of the collection. It takes a form of an averaged and normalized sequence of accumulated Zernike moments. The main descriptors (class profiles) of each type of tissue from our database are in Figure 7.33. How the main descriptor projects against the descriptors for each sample in the training set is shown in Figure 7.34.

This type of descriptors has many positive properties. The most important is that it provides an unambiguous method of identifying a particular image by creating an individual signature of such an image. It also carries a lot of properties associated with Zernike moments like rotation invariance within image boundaries and robustness to many types of noises [86]. After normalization, it also carries some resistance to varying intensity levels that can occur in images. By modifying

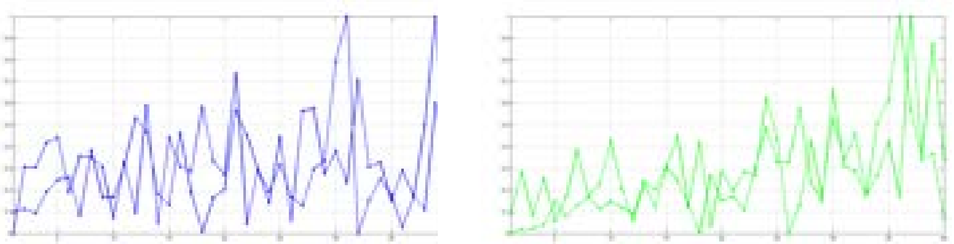

(a) Image descriptors from Class 1

(b) Image descriptors from Class 2

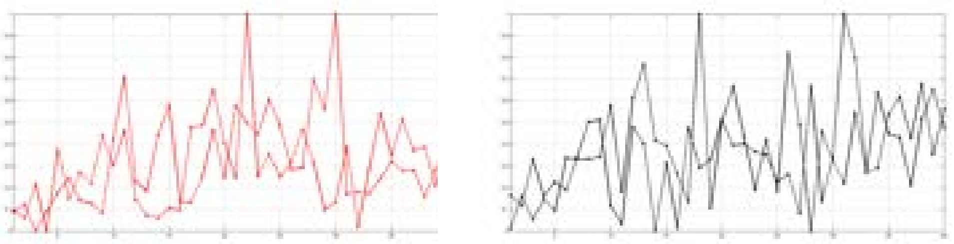

(c) Image descriptors from Class 3

(d) Image descriptors from Class 4

Figure 7.31: Examples of normalized image descriptors of samples from each tissue collection.

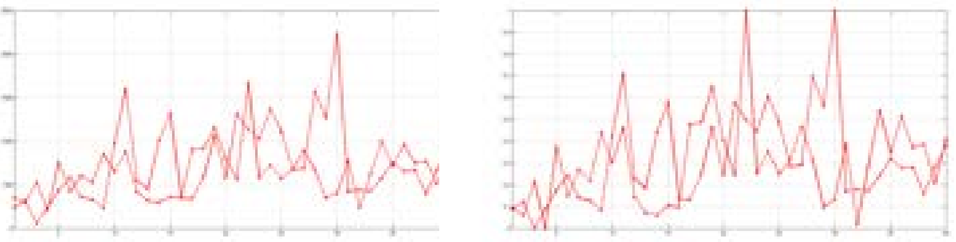

(a) I.d. for Class 3 before normalization.

(b) I.d. for Class 3 after normalization.

Figure 7.32: The normalization process of an image descriptor that highlights the difference between a normalized and unmodified image descriptor.

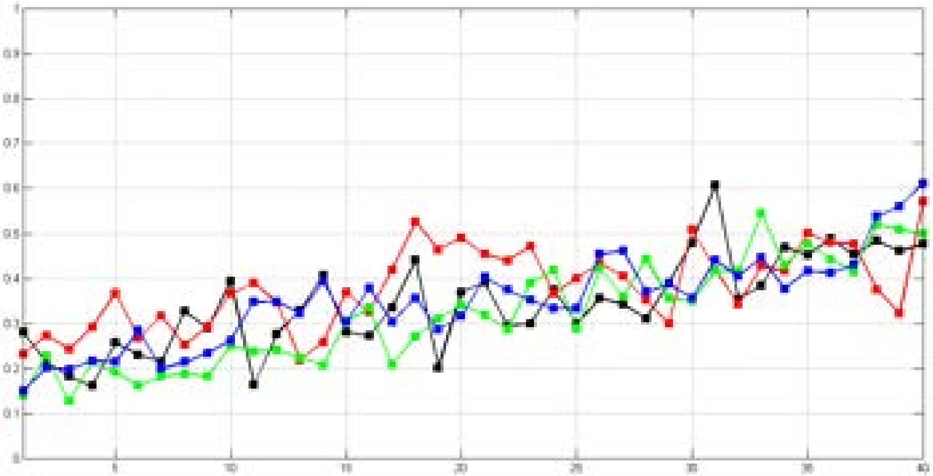

blue - Class 1, ***green*** - Class 2, ***red*** - Class 3, ***black*** - Class 4

Figure 7.33: The calculated class descriptors for each tissue collection using sample images from a training set.

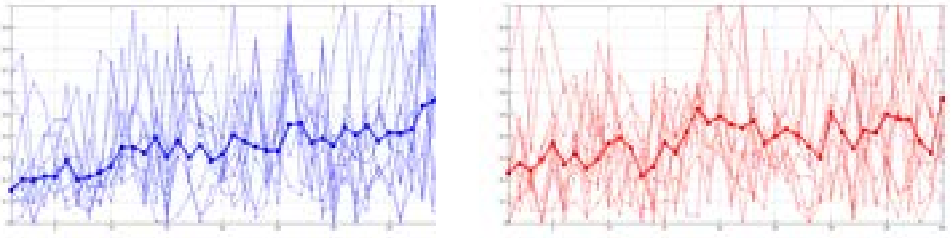

(a) Class 1

(b) Class 3

Figure 7.34: Main image descriptor for a class/tissue collection overlying descriptors of samples in a training set. Examples.

the order of moments in use it is possible to control the level of detail in the recognition process.

We assume that the method of tissue recognition should allow us for tissue type identification on the basis of the known class pattern or descriptor. As the identification criterion we are using MSE (Mean Squared Error). In this algorithm the image descriptor is compared to all available class descriptors, and the match-up with the lowest value of MSE is the correct match. The MSE in this case is calculated according to the formula

$$MSE = \frac{1}{N} \sum_{i=1}^{N} (|\hat{A}_i| - |A_i|)^2 \tag{7.8}$$

where $\hat{A}_i$ is the mean value of a Zernike moment in the main descriptor pattern. This way the MSE is the sum of squared differences between correlating values in the actual and assumed sequences of the main descriptor and pattern descriptor. The recognition criterion is the minimum value of MSE. The use of MSE as a base criterion establishes a point of reference for future development of the method. We do not expect very accurate results from using it.

The testing is performed on the database consisting of four types of tissue. Some examples of samples from the dataset are shown in Figure 7.30. It is a diverse set both in the context of in-class and out-class.

We divide the samples of each tissue class into training and testing sets. The training set is used to construct the main class descriptor (class profile) while we test the effectiveness of the method using the testing set. We use 75% of samples to build the profile and the remaining 25% are assigned to the testing set. We use MSE criterion to classify the testing samples.

The results of identification for each collection can be viewed in Figure 7.35 and Table 7.8. On the basis of this data we can establish how accurate is this approach for the problem of tissue identification. The data is divided into four columns which show how many samples are directed into each class. The accuracy of the classification is calculated according to the proportion of how many samples are identified correctly to the number of the samples in the whole set. The overall accuracy of identification using this approach is 53.6%. The worst accuracy is reached for Class 4, and it is 45%. The best results are for Class 3, and it is 75%. The results for the remaining collections stay in 45% to 56% range. In such situation, good results for Class 3 appear to be an exception.

Since true nature of tissue in the collections is not exactly verified, we cannot identify the samples beyond assigning them the label (S5, S40 and so on). The exact relation between collections is unknown, so it may influence the classification outcome. Despite poor results this approach works better than random guessing where the probability of success is 25%. We can try to expand on the idea by adding

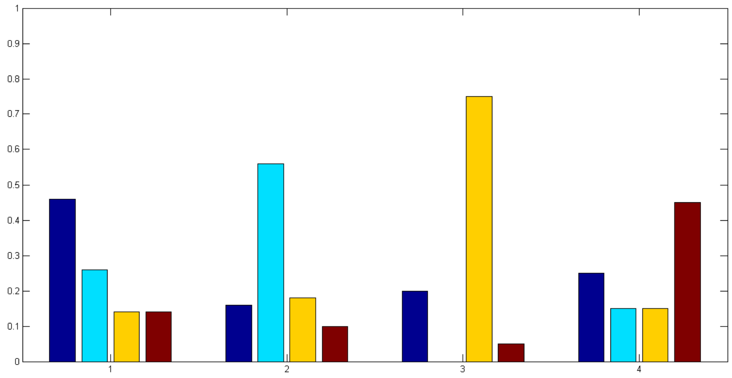

Figure 7.35: Plot of identification results for each tissue collection using MSE criterion.

Descriptor →	**1**	**2**	**3**	**4**	Color
Class 1	**0.4600**	0.2600	0.1400	0.1400	*blue*
Class 2	0.1600	**0.5600**	0.1800	0.1000	*light blue*
Class 3	0.2000	0.0000	**0.7500**	0.0500	*yellow*
Class 4	0.2500	0.1500	0.1500	**0.4500**	*red*

Table 7.8: Identification results for each tissue collection based on the MSE criterion.

more details into the descriptor by using the complete Zernike moment sequence instead of its accumulated form. Alternatively, we can use a more simplified image pattern and reduce the number of orders of Zernike moments. However, this approach limits the overall effectiveness of the method. In another approach, we may try using a classifier system that is more sophisticated than the basic MSE to improve the accuracy.

Alternative methods of recognition for this approach may include boosting algorithms [40] or neural networks [41]. Boosting algorithms are an approach to machine learning that centers around creating a precise prediction rule that uses many smaller, weak and imprecise rules. Examples of this approach are the AdaBoost algorithm and the weight and popularity voting approach [97]. In the case of neural networks the numeric model is created by generalization of the knowledge for the previously unknown data and the input and output data is depicted by weighted association.

7.3 Tissue Type Recognition on the Basis of Fragments Using Zernike Moments

This section follows up on the topic of recognition and classification of tissue types in microscope images. However, this time we expand our approach by using more complex tools. We construct a multi-classifier tool using many basic classifiers like neural networks and logistic regression. The final classification decision is a combined output of all the component classifiers. The input data still consists of Zernike moment-based descriptors of microscope images.

The goal of the proposed approach is to create a method that allows us for unambiguous recognition of the tissue type in the microscope image. We assume that identification should cover many types of tissue. The method should also allow us for a certain generalization of the knowledge, because while tissue samples are similar they may not contain common elements. To cover such cases the classifiers should support a multi-class system.

Tissue in microscope images often has characteristic, but complex structures. Some unambiguous differences may occur between various tissue types. Even one collection of some tissue can consist of a very diversified group. Because of that tissue structure is very difficult to translate into numeric space. Examples of microscope images of some tissue that highlight the diversity of the subject are in Figure 7.36.

Figure 7.36: Examples of microscope images of various tissue samples that showcase the diversity between different types of tissue as well as within the groups.

The proposed method uses a classification algorithm that is built out of a combination of known classification algorithms and Zernike moment-based image descriptors. The image descriptor is a sequence of Zernike moments calculated according to (4.1). It corresponds to a numeric pattern of the image making it a descriptor of the said image. The image classification is performed on the basis of sequences of Zernike moments. In this concept, the composite classifier consists of a set of common classifiers and the final decision is made according to the mechanism of majority voting.

The sequence of Zernike moments is build according to (4.6):

$$\{|A_1|, |A_2|, |A_3|, \ldots, |A_N|\}, \tag{7.9}$$

where A_i is an accumulated Zernike moment of the order i and N is the maximum order of the moment used in implementation. It is an ordered sequence, and we assume that similar images share similar sequences.

The composite classifier is build out of a set of singular classifiers. The set of subservient classifiers consists of Random Forests (RF), Neural Networks (NN), Naive Bayes (NB), Support Vector Machine (SVM), Nearest Neighbor (NNB), Logistic Regression (LR). In this implementation we supplement the classifiers form the tool set available in numerical software *Mathematica*.

The form of the composite classifier is as follows

$$\text{Multi} = \{RF, NN, NB, SVM, NNB, LR\}. \tag{7.10}$$

The decision on sample classification is made via the process of majority voting where the sample is assigned to the class with the most occurrences in the set of classifiers. The purpose of this mechanic is to eliminate singular mistakes that can occur when only one classifier is in use.

For this experiment we use images in grayscale. The standard size of the tissue image is 600×600px. In the numeric computation we use images resized to the size of 120×120px. The image database for this experiment consists of 4 types of tissue. The collections are numbered with Roman numerals from I to IV and are as such: I - bronchial epithelium cells (160 samples), II - lung pleura (105 samples), III - striated muscle (168 - samples), IV - tendon (145 samples). Some samples from each collection are shown in Figure 7.37.

The effectiveness of the method is tested in the series of experiments. Between the experiments we change the number of testing samples and the number of classes. The criterion of the effectiveness is the percentage of the number of correctly classified samples. The classification matrix is a graphic presentation of the classification results for the samples across all available classes.

In the experiment, we use the test sets as presented in Table 7.9. We use the notation of "{}". Sets of classification groups are separated with commas. A set can consist of one class of tissue or more. The "+" notation describes the consolidation of at least two classes into one classification set.

In the case of Test #0, the classification error stays in the range from 78.6% (NNB) to 90.2% (SVM), but usually it oscillates around the average accuracy of 84.0%. Depending on the approach the number of misclassified samples is between 10-21%. Most mistaken for each other is tissue from collections I and II. The complete results are shown in Table 7.10 and the graphic distribution of samples in selected classifiers is shown in Figure 7.38.

In set-up of Test #1 there is no class I in order to create a set-up with no tissue interference. With this change the accuracy of the classifiers raised into the 90.3% (NNB) to 96.6% bracket. Lack of two separate, but similar classes improves

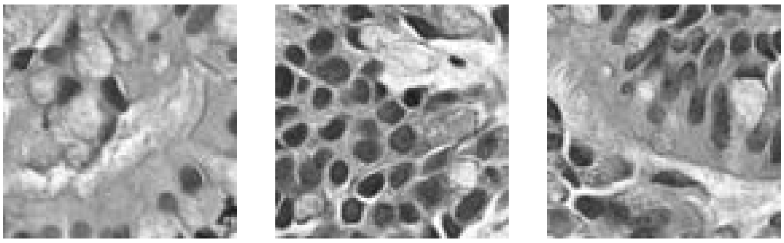

(a) I - bronchial epithelium cells

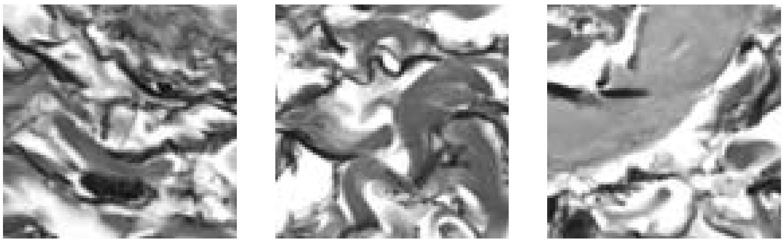

(b) II - lung pleura

(c) III - striated muscle

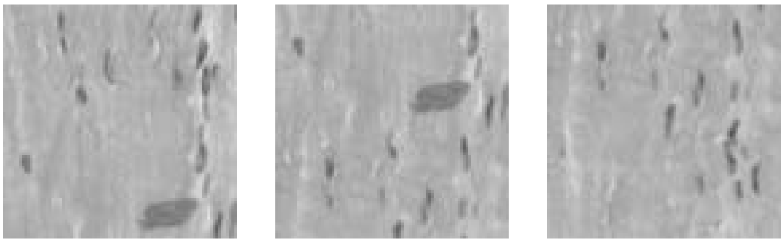

(d) IV - tendon

Figure 7.37: Sample images of tissue collections: I - bronchial epithelium cells, II - lung pleura, III - striated muscle, IV - tendon.

Test #	no. class	classes	no. samples/training set
0	4	{I, II, III, IV}	70%
1	3	{II, III, IV}	50
2	3	{II, III, IV}	70%
3	3	{I, III, IV}	70%
4	2	{I+II, III, IV}	70%
5	2	{I, II}	70%
6	2	{I, II}	73
7	2	{I+II, III+IV}	70%
8	2	{I, II+III+IV}	70%
9	2	{II, I+III+IV}	70%
10	2	{III, I+II+IV}	70%

Table 7.9: Testing sets for the composite classifier of tissue type in the problem of tissue recognition.

Test #	**RF**	**NN**	**NB**	**SVM**	**NNB**	**LR**
0	0.849711	0.867052	0.849711	0.901734	0.786127	0.820809
1	0.955224	0.958955	0.955224	0.966418	0.902985	0.94403
4	0.959538	0.982659	0.976879	0.976879	0.971098	0.959538
7	0.982659	0.988439	0.988439	0.99422	0.988439	0.99422

Table 7.10: Averaged results of classification with individual classifiers from the list for selected test set-ups.

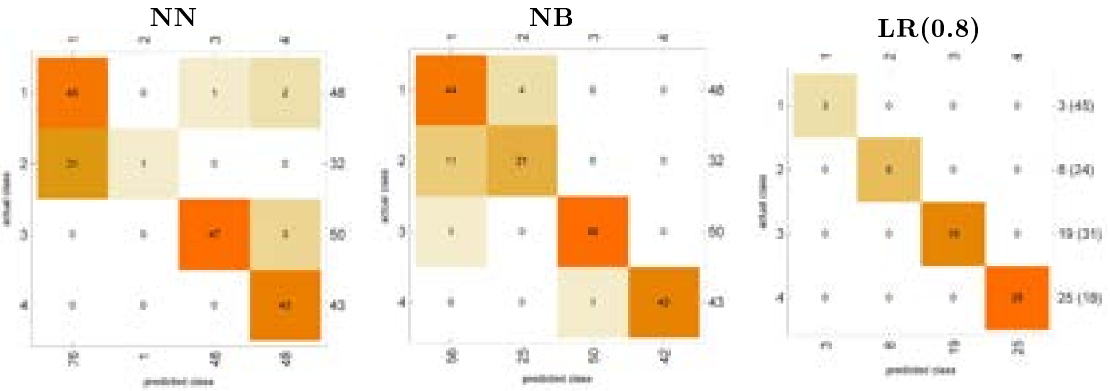

Figure 7.38: Close up on part of the results for Test #0.

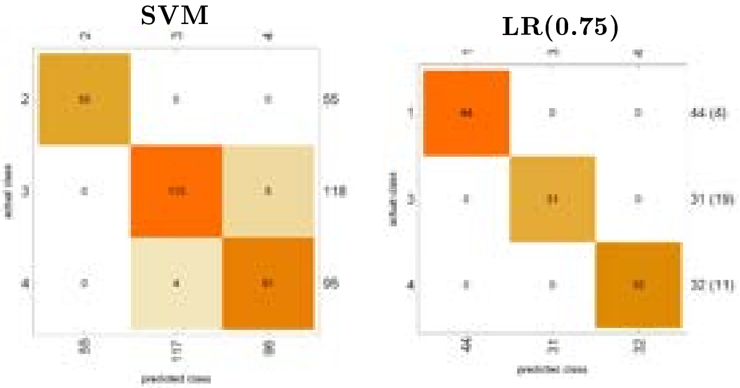
SVM **LR(0.75)**

Figure 7.39: Close up on part of the results for Test #1.

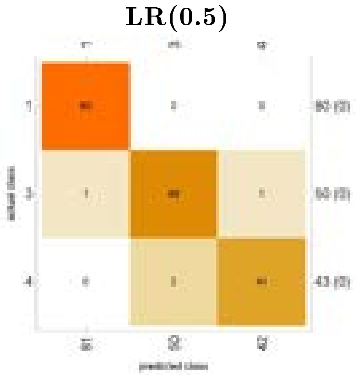
LR(0.5)

Figure 7.40: Close up on part of the results for Test #4.

the accuracy of prediction. The complete results are shown in Table 7.10 and the graphic distribution of samples for selected classifiers is shown in Figure 7.39.

In Test #4, we conflated two classes into one, and so collections I and II become class I+II that contains tissue samples from both of its composite classes. As in the case of Test #1 this set-up aims to minimize the interference that comes from similarity of two tissue collections, but this time by conflating the two classes. The classification error in this case is in the range from 96.0% (RF, LF) to 98.2% (NN). Depending on the classifier, the number of misclassified samples is in the 2-6% range. The complete results are shown in Table 7.10 and the graphic distribution of samples for selected classifiers is shown in Figure 7.40.

In Test #7, we reduce the number of available classes to two. The new classes consist of a joined collection of I and II (I+II) and III and IV (III+IV). Class I+II represents the lung tissue and class III+IV represents a muscle tissue of the heart and tendon respectively. The classification error for this set-up stays in the very close range of 98.3% (RF) to 99.3% (SVM, LR). The differentiation within the

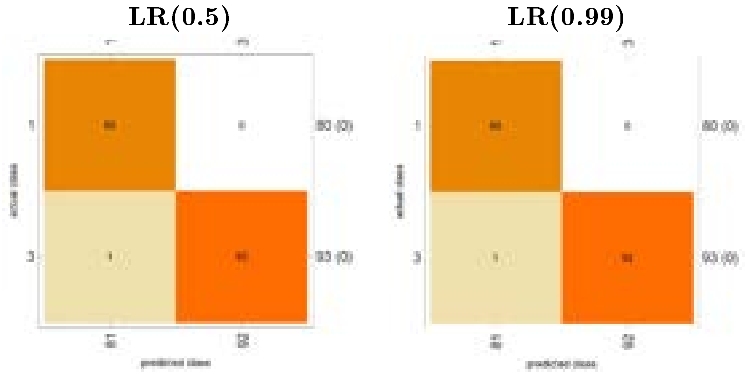

Figure 7.41: Close up on part of the results for Test #7.

Classifier	Class I samples	Accuracy
RF	1 1 1 1 1 1 1 1 1 2 1 1 1 2 1 1 1 2 1 1 1 1 1 1 1 1 1 1 1 1 1 1 1 1 1 1	0.9167
NN	1 1 2 1 1 1 1 1 1 1 2 1 1 2 1 1 1 1 1 1 1 1 1 1 1 1 1 1 1 1 2 2 1 1 1 1	0.8611
NNB	1 1 1 1 1 1 1 1 1 1 1 1 1 2 1 1 1 1 1 1 1 1 1 2 1 1 1 1 1 1 2 1 1 1 1 1	0.9167
SVM	1 1 1 1 1 1 1 1 1 1 1 1 1 2 1 1 1 1 1 1 1 1 1 2 1 1 1 1 1 1 2 1 1 1 1 1	0.9167
NB	1 1 1 1 1 1 1 1 4 1 1 1 1 1 1 1 1 1 1 1 1 1 1 1 1 1 1 1 1 3 1 1 1 1 1 1	0.9444
LR	1 1 2 1 1 1 1 1 1 2 2 1 1 2 1 1 1 2 1 2 2 1 1 1 1 1 1 1 1 1 1 2 1 1 1 1	0.7778
Multi	1 1 1 1 1 1 1 1 1 1 1 1 1 2 1 1 1 1 1 1 1 1 1 1 1 1 1 1 1 1 1 1 1 1 1 1	0.9722

Table 7.11: Class assignment of samples in the testing set for class I from Test #0.

same group of tissue for classes I and II, and III and IV stays in the 20-39%. The complete results are shown in Table 7.10 and the graphic distribution of samples for selected classifiers is shown in Figure 7.41.

The composite classifier improves the rates of accuracy. In some cases the results are no better than the best accuracy of individual classifiers, but it is not the worst result in the entire comparison. The achieved accuracy does not fall below 75% in all tests. With correct configuration it is possible to obtain accuracy on the level of 90% and more. Depending on the classifier, the classification error can be minimized to 3-11%. The majority of errors occur in collections that contain similar types of tissue or ones that come form similar sources, e.g. different types of lung tissue. This approach is also collected and presented in [41].

This method allows us to use Zernike moments for recognition of tissue types in microscope images. In most cases the accuracy of sample identification remains in the 90% level or higher. The method is easily scalable and can be used in more complex classification problems. The method can be improved by introducing a weight system to the voting process. In such case, classifiers with better prediction abilities would have a greater weight assigned to them.

Classifier	Class II samples	Accuracy
RF	2 1 2 2 2 2 1 1 2 1 1 2 1 1 2 1 1 1 2 1 2 2 2 1 2 2 1 1 1 1 2 1	0.4688
NN	1 2 2 2 2 2 2 1 2 2 2 2 1 1 2 1 1 1 2 2 2 2 2 2 2 2 2 1 1 1 1 2	0.6563
NNB	2 1 2 2 2 2 2 1 2 1 2 2 1 2 2 1 1 1 2 2 2 2 2 1 2 1 2 2 1 1 2 2	0.6563
SVM	2 2 2 2 2 2 1 1 2 1 2 2 1 2 2 1 1 1 2 2 2 2 2 2 2 2 1 1 1 1 2 2	0.6563
NB	1 1 1 1 1 1 1 1 1 1 1 1 1 1 1 1 1 1 1 1 1 1 1 1 2 1 1 1 1 1 1 1	0.0313
LR	1 2 2 2 2 2 2 2 2 1 2 2 2 1 2 1 1 1 2 1 2 2 2 1 2 2 1 1 1 1 1 1	0.5625
Multi	2 2 2 2 2 2 2 1 2 1 2 2 1 1 2 1 1 1 2 2 2 2 2 1 2 2 1 1 1 1 2 2	0.6250

Table 7.12: Class assignment of samples in the testing set for class II from Test #0.

7.4 Automatic Tissue Type Classification Using Sampling Data and Zernike Moments

The problem in this section is tissue identification of histological sections on large microscope images. These are very high resolution images containing gigabytes of data. Effectively processing such amount of data directly in computation is difficult and often inviable. Another set of difficulties arises form internal structures of tissue samples that vary across different regions of the tissue. There is also the issue of tissue damage, disfigurement and discoloration that can occur in microscope images.

The proposed approach to this problem is a robust classification algorithm that identifies the tissue type of microscope image. The method uses only parts of the available image data. We procure sample data in the process of multiple random sampling. The main component of the method are accumulated Zernike moments that serve as image descriptors. This approach was previously tested in [40] and [41].

At the basis of the algorithm are accumulated Zernike moments. Their properties and the method of calculation are already included in section 4.2. The image descriptor is constructed with accumulated Zernike moments, and it is an ordered set. Such depiction allows us to look at it as a pattern. We assume that similar images are described with sequences of similar values, and we can look at it as a pattern-matching problem. The descriptor also borrows from the properties of Zernike moments. Most notable are that their invariants can be calculated independently of higher orders without the need to recalculate low order invariants. They do not carry redundant data and the information does not get replicated in consecutive moments. Using right processing methods they can be made invariant to rotation, translation, and scaling.

Many complexities of the tissue structure make it difficult to identify the subject on the basis of random small sample images. In many cases, using the entire image in investigation is also impossible due to the sheer size and the amount of data that would need to be processed. Therefore, in this approach we rely on a localized and small-scale, but a more compound process of classification. We use multiple small classifications for multiple random samples form the source image. The final identification decision is made using combined outputs from all individual classifications. Single classification decision for a small sample may not fully correspond to the source image. Using multiple samples and classification tools broadens the scope and makes the final decision more robust and less likely to be misinterpreted due to one poor questioning classification. This approach relies on the notion that the likelihood of good classification grows with more observations [55].

(a) I (b) II (c) III

Figure 7.42: Selected source images of microscope sections of human tissue.

The classification algorithm in this method uses build-in classification tools provided by *Mathematica* software. In this experiment, we apply three types of classifiers from its toolbox: Neural Networks (NN), Support Vector Machine (SVM) and Logistic Regression (LR).

The accumulated classification output is calculated according to the formula

$$\overline{y} = [\overline{y}_1, \overline{y}_2, \ldots, \overline{y}_K], \tag{7.11}$$

where

$$\overline{y}_i = \sum_{j}^{M} y_{ij} \tag{7.12}$$

and y_{ij} is the output of the j-th classification for the class i. Here, K is the number of classes in this experiment, and M is the number of outputs used to calculate the accumulated result.

The output of the classification is normalized into a probability distribution using a softmax function

$$S(\overline{y}_i) = \frac{\exp(\overline{y}_i)}{\sum_j \exp(\overline{y}_j)}, \tag{7.13}$$

where $\overline{y}_i$ is the classifier's accumulated output for the class. The decision criterion in this case takes the form of

$$\max_i S(\overline{y}_i). \tag{7.14}$$

The data set used in the experiment consists of microscope images of human tissue. The source images of histological sections are stored in big data format (∼1.5GB). The samples are cut out from random regions across multiple subjects in the same series of slides. The standard size of the sample image is 400×400 px. We have three image series, numbered in Roman numerals from I to III that consist of 800 sample images each. Selected source images are shown in Figure 7.42, and examples of input image samples are in Figure 7.43.

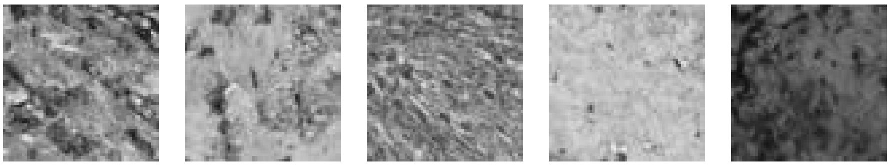

(a) Class I

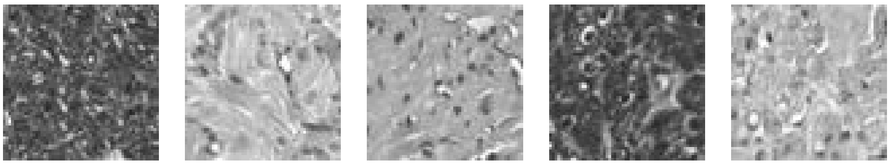

(b) Class II

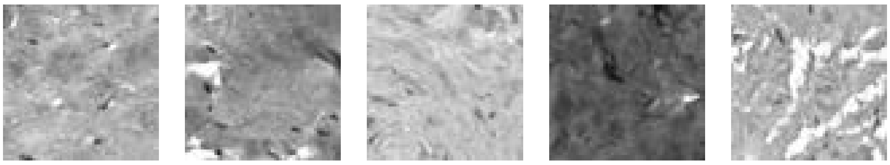

(c) Class III

Figure 7.43: Sample images of input samples from microscope image series from Figure 7.42.

Cl.	#1	#2	#3	#4	#5	#6	#7	#8	#9	#10
I	0.4200	0.5250	0.5587	0.6000	0.6375	0.6300	0.6387	0.7200	0.6975	0.7875
II	0.6088	0.7025	0.7725	0.8100	0.8125	0.8625	0.8488	0.9000	0.8888	0.9375
III	0.7462	0.8300	0.9187	0.9200	0.9563	0.9750	0.9800	1.0000	0.9788	1.0000

Table 7.13: Classification results for Logistic Regression using multiple input samples in Classes I to III.

The test suits in this experiment are organized by classifier and by the number of samples used in classification. We use the in-built classifiers from *Mathematica* toolbox that are Neural Networks (NN), Support Vector Machine (SVM) and Logistic Regression (LR). The number of samples that are used in classification is counted from 1 to 10. Accounting for each cross-case, in total, that makes 30 test scenarios.

The averaged results for each test suit are accumulated in Table 7.13, 7.14 and 7.15. The tables contain classification output grouped for each classification method. Each table contains the breakdown for each tissue type and the classification output for the number of samples used in the classification.

The data in the tables shows that the probability of correct classification rises with every additional sample. The initial classification results for a single sample range from 42% to 77% depending on the class and the classification method that

Cl.	#1	#2	#3	#4	#5	#6	#7	#8	#9	#10
I	0.5587	0.5900	0.6600	0.7250	0.7250	0.7650	0.7700	0.8500	0.8100	0.9250
II	0.6312	0.7300	0.7950	0.8250	0.8625	0.9000	0.9012	0.9300	0.9225	0.9375
III	0.7113	0.8150	0.8775	0.9100	0.9313	0.9450	0.9625	0.9900	0.9788	1.0000

Table 7.14: Classification results for Support Vector Machine using multiple input samples in Classes I to III.

Cl.	#1	#2	#3	#4	#5	#6	#7	#8	#9	#10
I	0.5250	0.6325	0.6563	0.7100	0.7375	0.7725	0.7700	0.8100	0.7988	0.8375
II	0.5625	0.6625	0.6862	0.7400	0.7625	0.8100	0.8050	0.8200	0.8438	0.8750
III	0.7738	0.8475	0.9000	0.9300	0.9375	0.9675	0.9800	0.9800	0.9675	0.9750

Table 7.15: Classification results for Neural Networks using multiple input samples in Classes I to III.

is used. In this set-up, the lowest score is achieved with LR classifier for class I and the highest one with NN classifier for class III. With the maximum number of samples, that is 10, the classification falls into the range from 79% to over 90%.

The end results depend heavily on the applied classifier and the diversity of the image series. SVM classifier works better for this type of problem than NN and LR classifiers. The most divisive class of tissue turns out to be I. It is the class that results in the most number of inaccurate classifications, but using the appropriate number of samples in the process increases the probability of a correct classification. Classes II and III are much more approachable with III being the easiest to correctly identify.

The correct classification threshold starts in the lower 90% for most of the test cases if we include a necessary number of samples. Depending on the type and the complexity of the tissue the number of needed samples vary and needs to be adjusted accordingly. Depending on the size of the source image and the number of samples that are used. We utilize approximately 0.8%-1.1% of the original image to solve this classification problem.

This method promises to be easily scalable as both the number of samples and the size of the image can be modified. Since there is no restriction to the size of the source image, it can easily be applied to more complex classification problems with large image data. This approach and parts of the work are presented in [42].

7.5 Detection of Damage and Errors in Microscope Section Collections

This section covers the application of accumulated Zernike moments in detection of damage and errors in microscope section collections. Damaged, erred and/or absent preparations that occur in microscope section collections can interfere in collection and atlas image database building among other things. This problem covers such issues as damaged or missing parts of the tissue in the section, heavy discoloration or deformation of the tissue or mislabeled and misclassified preparations. Therefore, their identification and detection are quite important. The purpose of this method is to provide new means of automated detection of such phenomena in very big data collections that normally would be too difficult and time-consuming for manual inspection.

It is important to detect when the preparation is damaged or absent, or even sent to a collection by mistake, regardless of the cause of the issue. The main goal is to keep the collection homogenous and without outliers that can influence the analysis or diagnosis.

The problem can be summarized as detection of absent, damaged and/or mislabelled preparations in microscope section collections. The expected functionality of the algorithm should allow us to detect damaged preparations or their absence, to select images that were sent to the collection by mistake and to keep integrity of the collection.

The proposed approach provides a method of automatic inspections of such collections and allows us for preliminary selection of suspect preparations. That is damaged, absent and non-matching data samples in microscope image collections and sequences. The potential benefits of such approach are limited manual interaction with samples, shortened time of data selection and segregation and that the image data is stored in compact form and takes up less disk space.

The method uses accumulated Zernike moments as a primary tool in its pattern-recognition algorithm. It is assumed that if the biomedical tissue belongs to the same-purpose group, e.g. cardiac or muscle tissue, the patterns of both sequences would be similar.

We use precise sequences of accumulated Zernike moments to calculate descriptor/pattern references for microscope images. Based on this sequence we estimate the identification pattern for the tissue type that serves as the reference for any future microscope images. This reference descriptor allows us to find any image descriptors that do not match the pattern in any remarkable way. Depending on the complexity of the subject the reference descriptor can be obtained by using an AI system (e.g. a neural network) or other numeric methods (e.g. MSE).

The sequence of accumulated Zernike moments is described with

$$D = Z_1, Z_2, Z_3, \ldots, Z_N \tag{7.15}$$

This formula is already introduced in [EQUATIONREF]. The examples of application of this sequence for selected collections of tissue are visible in Figure. 7.44.

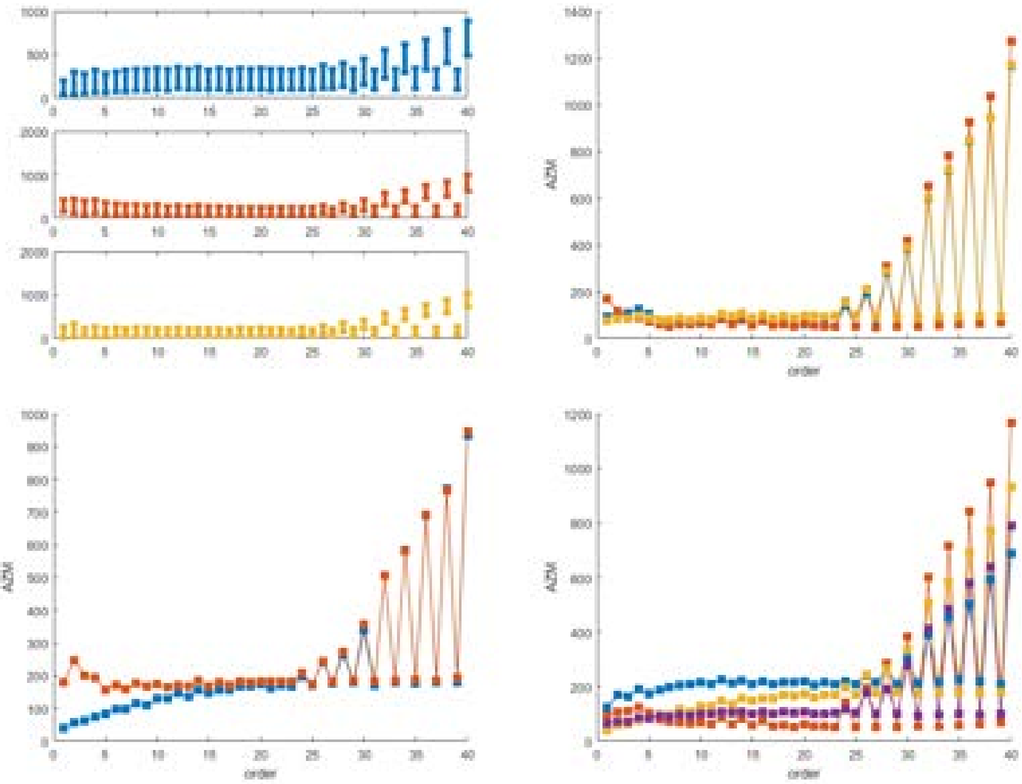

Figure 7.44: Examples of sequences of accumulated Zernike moments for selected collections of tissue samples. The examples include, from left-to-right and top-to-bottom, collection of cardiac muscle tissue with complete, damaged and unrelated samples, collection of striated muscle tissue with the same as previous example, collection of vein tissue with complete and damaged samples and multiple collections of various types of tissue.

In this experiment we evaluate three scenarios: selection of complete samples from the image collection, dividing collection into sample groups of interest, detection of samples that do not match the collection. Each data set is constructed using the mix of samples from various groups of tissue.

In this evaluation the reference image descriptor is build for each type of the tissue. It implements one of the preselected strategies: only complete samples,

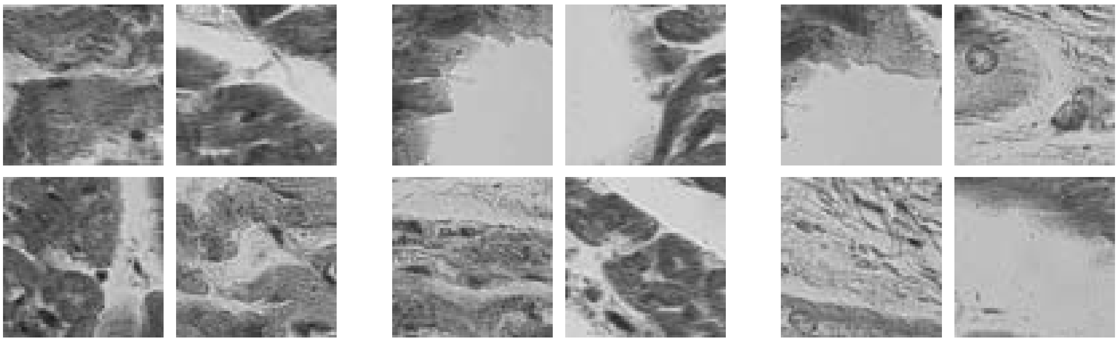

(a) Complete (b) Parts (c) Other

Figure 7.45: Tissue samples of cardiac muscle.

samples with damages (ranging from minor to major damages) and samples that do not match the common pattern of the tissue type. Any significant variation between the reference descriptor and the inspected sample descriptor can point to a potentially damaged or absent section. The reference descriptor for each type and identification strategy is build using *Mathematica* software and its classification tools. We use Logistic Regression (LR), Neural Networks (NN) and Support Vector Machines (SVM) methods as the classifiers. The samples are selected/detected using the probability of classification as the metric. The decision criterion refers to the probability value to make the final assessment.

In the experiments, we use 4 different collections of microscope images of biomedical tissue. The collections contain samples of tissues from cardiac muscle, striated muscle, tissue of vein preparation - label S27, tissue of vein preparation - label S40. The collection is derived from multiple high-resolution microscope images that are sectioned into smaller parts. The origin image has either missing, discolored or non-related parts. Thus, we can divide the database into the following categories of samples: complete, damaged and other. The database for this study consists of over 7000 image samples with assigned image descriptors. We can organize the data samples into two major categories that can be divided further into minor categories. The major categories are the type of biomedical tissue, e.g. cardiac muscle, striated muscle. The minor categories describe the level of integrity and content of the sample that cover cases where the image contains complete tissue, the image contains tissue that is missing parts or is deformed in some way or the image contains tissue that does not match the baseline pattern of the type of tissue. The examples of the tissue samples can be viewed in Figure 7.45, 7.46, 7.47 and 7.48.

Set-up #1, **selection of complete samples from the image collection**, describes a scenario where we expect the sample to be identified as either a complete

(a) Complete (b) Parts (c) Other

Figure 7.46: Tissue samples of striated muscle.

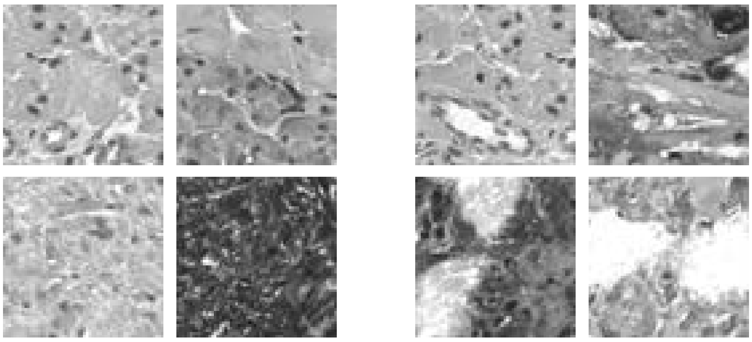

(a) Complete (b) Parts

Figure 7.47: Tissue samples of vein section S27.

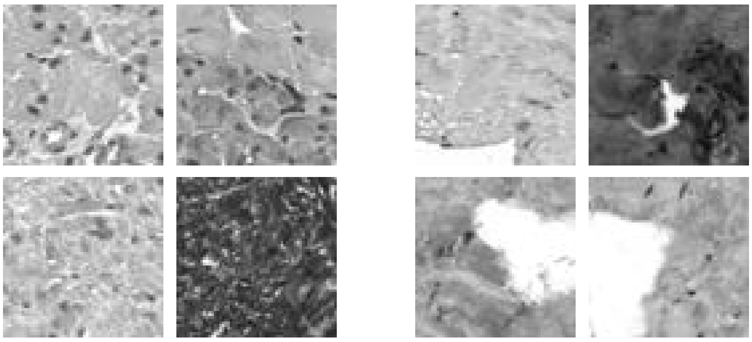

(a) Complete (b) Parts

Figure 7.48: Tissue samples of a vein section S40.

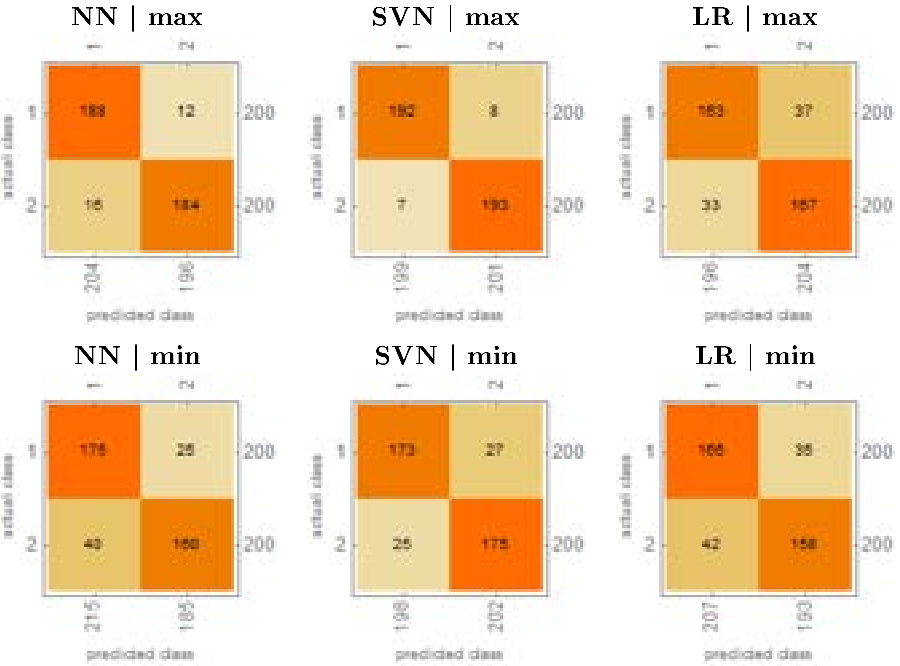

Figure 7.49: Minimum and maximum accuracy distribution for cardiac muscle collection in set-up #1.

sample or other (non-complete). The complete category stands for an image that contains a tissue fragment that is neither disfigured, nor discolored, nor has any missing parts. Everything that does not fit this criterion is ascribed to the other category. The aim of this test set is to evaluate how accurate is this method in detection and identification of damaged and complete tissue samples. This set-up is run for all collections of tissue samples.

The highest achieved accuracy for this set-up is 96.3% (SVM), the lowest - 79.0% (SVM) with mean value of 87.2% across all samples and classifiers (see Table 7.22). The averaged results for all test runs are collected in Table 7.16 and 7.17. This is the most evened out set-up when it comes to accuracy across all cases.

The accuracy of detection stays at similar level across all tissue collections and ranges from 85% to 88.5% on the average (Table 7.16). A similar case is present for the classifiers that are used in the test. The accuracy of all classifiers stays on a similar level and ranges from 85.4% to 88.8% (see Table 7.17). Using a predetermined reference pattern of a complete tissue sample it is possible to detect samples that are damaged or different from the default within the collection. To obtain good results the collection does not need to be very homogenous in appearance, but it still should contain a recognizable pattern.

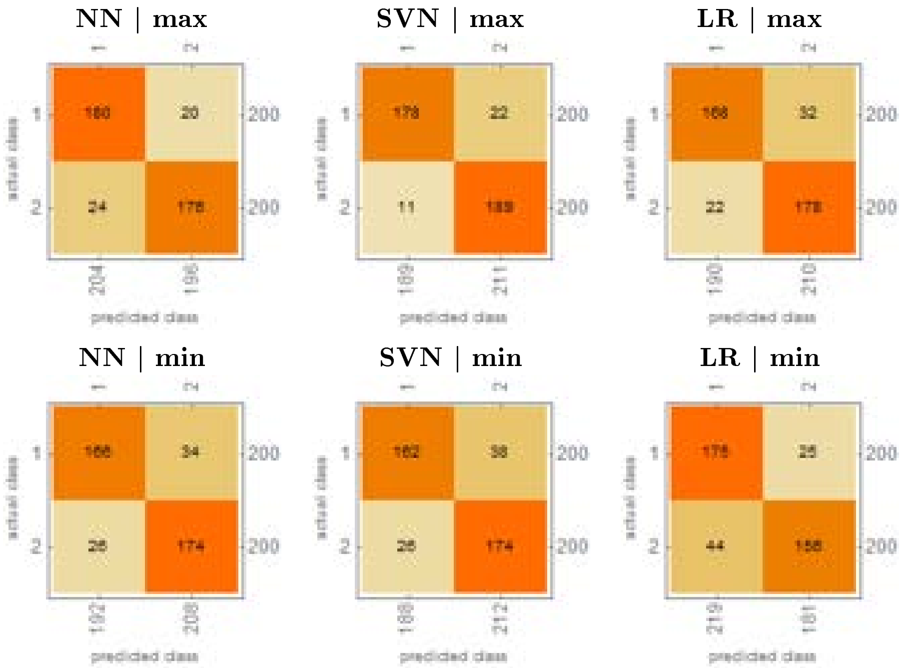

Figure 7.50: Minimum and maximum accuracy distribution for striated muscle collection in set-up #1.

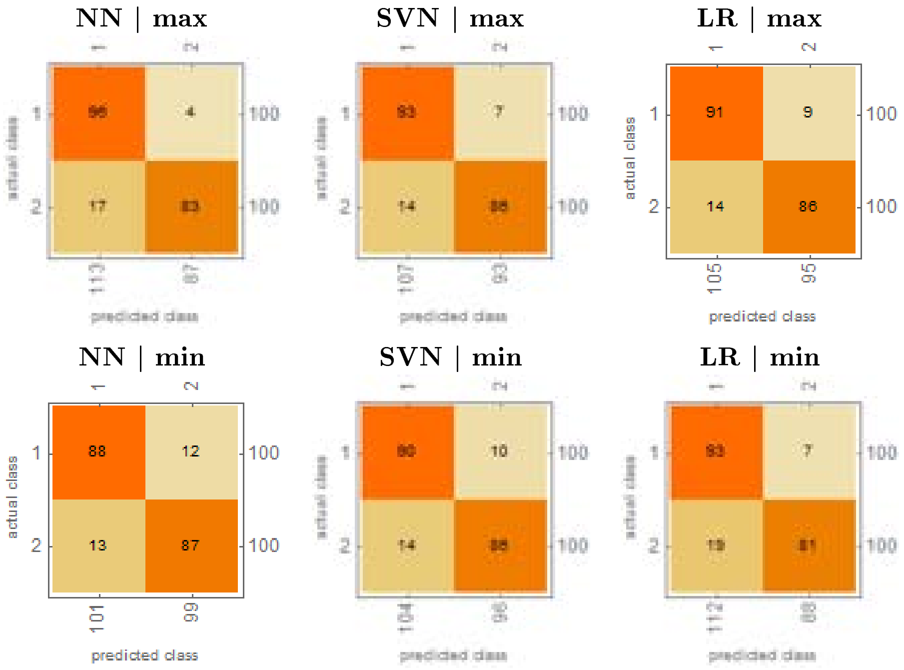

Figure 7.51: Minimum and maximum accuracy distribution for tissue S40 collection in set-up #1.

cardiac muscle

	max	**min**	**mean**
NN	0.930	0.830	0.887
SVM	0.963	0.870	0.915
LR	0.873	0.808	0.852
all	0.963	0.808	0.885

striated muscle

	max	**min**	**mean**
NN	0,890	0,850	0,868
SVM	0,918	0,840	0,888
LR	0,865	0,823	0,841
all	0,918	0,823	0,866

tissue S40

	max	**min**	**mean**
NN	0,895	0,875	0,885
SVM	0,895	0,880	0,885
LR	0,885	0,870	0,874
all	0,895	0,870	0,881

tissue S27

	max	**min**	**mean**
NN	0,854	0,835	0,847
SVM	0,854	0,790	0,836
LR	0,888	0,849	0,867
all	0,888	0,790	0,850

Table 7.16: Collection of minimum, maximum and averaged values of achieved accuracy for each tissue collection across all classifiers. Set-up #1.

neural networks

	max	**min**	**mean**
cardiac	0,930	0,830	0,887
striated	0,890	0,850	0,868
s40	0,895	0,875	0,885
s27	0,854	0,835	0,847
all	0,930	0,830	0,874

support vector machines

	max	**min**	**mean**
cardiac	0,963	0,870	0,915
striated	0,918	0,840	0,888
s40	0,895	0,880	0,885
s27	0,854	0,790	0,836
all	0,963	0,790	0,888

logistic regression

	max	**min**	**mean**
cardiac	0,873	0,808	0,852
striated	0,865	0,823	0,841
s40	0,885	0,870	0,874
s27	0,888	0,849	0,867
all	0,888	0,808	0,854

Table 7.17: Collection of minimum, maximum and averaged values of achieved accuracy for all classifiers across all tissue collections. Set-up #1.

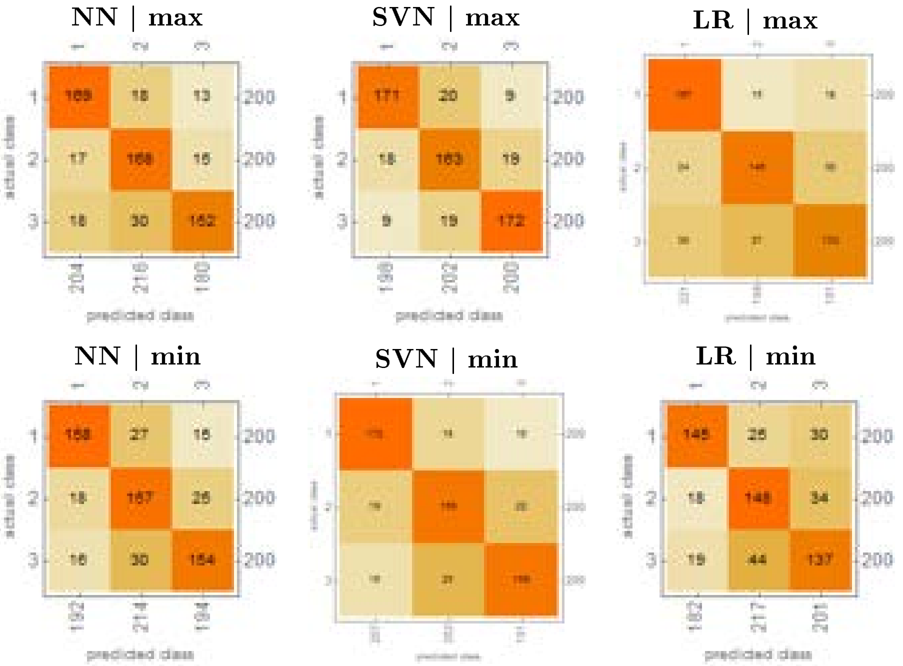

Figure 7.52: Minimum and maximum accuracy distribution for cardiac muscle collection in set-up #2.

In the set-up #2, **identification of samples that does not match the collection**, the testing covers the situation where the collection contains both complete and damaged samples of the same type as well as images that contain unrelated tissue samples. Because of that, we divide the collection into three categories: complete, damaged and other. The goal is to test the accuracy of identification of both the given type of tissue and detection of damaged samples and unrelated samples. This set-up is run for collections of cardiac muscle and striated muscle tissue samples.

The highest achieved accuracy is 86.3% (SVM), the lowest - 71.7% (LR) with averaged value of 80.0% across all samples and classifiers (see Table 7.22). The averaged results for all test runs are collected in Table 7.18 and 7.19.

The accuracy of the detection oscillates between 70% and lower 80%, and it is the most diverse pool of results. This is the case for both tissue collections (see Table 7.18) and all the applied classifiers (see Table 7.19). However, for SVM classifier the accuracy stays over the 80% and boasts the configuration of the highest achieved accuracy.

This set-up is the most inconsistent and has the lowest averaged accuracy. Differentiating between three groups of similar tissue samples appears to be less unequivocal than the detection of only complete type of samples out of the set.

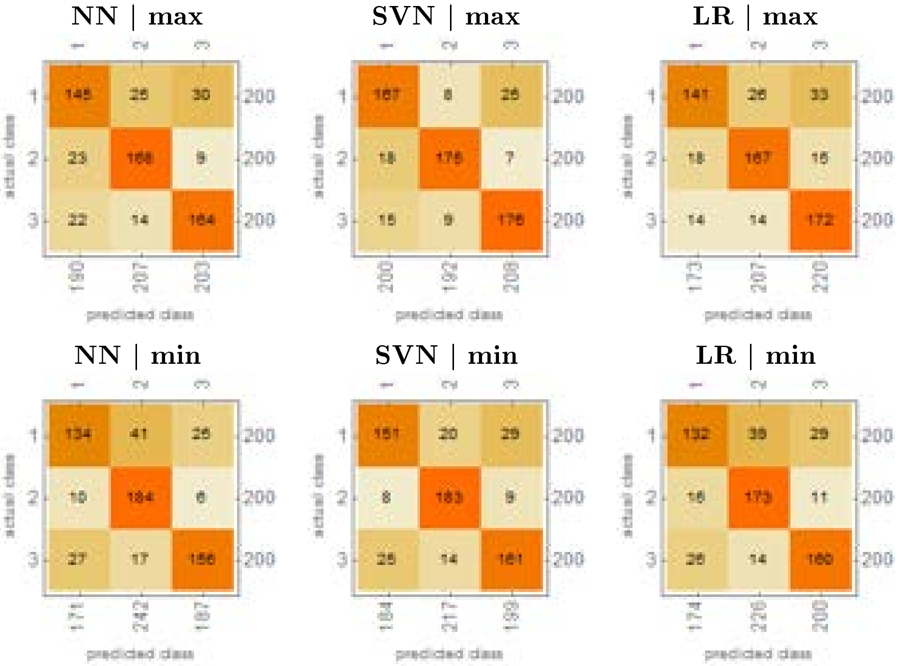

NN | max **SVN | max** **LR | max**

NN | min **SVN | min** **LR | min**

Figure 7.53: Minimum and maximum accuracy distribution for striated muscle collection in set-up #2.

cardiac muscle

	max	**min**	**mean**
NN	0,815	0,782	0,797
SVM	0,843	0,817	0,834
LR	0,743	0,717	0,734
all	0,843	0,717	0,788

striated muscle

	max	**min**	**mean**
NN	0,830	0,790	0,810
SVM	0,863	0,807	0,835
LR	0,800	0,775	0,792
all	0,863	0,775	0,812

Table 7.18: Collection of minimum, maximum and averaged values of achieved accuracy for each tissue collection across all classifiers. Set-up #2.

neural networks

	max	min	mean
cardiac	0,815	0,782	0,797
striated	0,830	0,790	0,810
all	0,830	0,782	0,803

support vector machines

	max	min	mean
cardiac	0,843	0,817	0,834
striated	0,863	0,807	0,835
all	0,863	0,807	0,835

logistic regression

	max	min	mean
cardiac	0,743	0,717	0,734
striated	0,800	0,775	0,792
all	0,800	0,717	0,763

Table 7.19: Collection of minimum, maximum and averaged values of accuracy for all classifiers across all tissue collections. Set-up #2.

striated muscle

	max	min	mean
NN	0,927	0,915	0,921
SVM	0,918	0,917	0,918
LR	0,892	0,877	0,884
all	0,927	0,877	0,908

tissue S40

	max	min	mean
NN	0,850	0,800	0,822
SVM	0,867	0,783	0,823
LR	0,840	0,807	0,820
all	0,867	0,783	0,821

Table 7.20: Collection of minimum, maximum and averaged values of achieved accuracy for each tissue collection across all classifiers. Set-up #3.

Adding another class with similar composition to the set-up lowered the accuracy of the prediction.

In the set-up #3, **identification of samples that does not match the collection**, we have three classes. Two come from the same tissue collection, but contain separated complete and damaged samples of the tissue. The last class contain tissue samples that come from a different collection. The aim of this set-up is to discern whether the algorithm can detect and identify samples that do not belong to the given collection. This set-up is run for the tissue collection of striated muscle and tissue S40 with additional samples coming from cardiac muscle and S27 tissue collections.

The highest achieved accuracy is 92.7% (NN), the lowest - 78.3% (SVM) with mean value of 86.4% across all samples. (see Table 7.22). The averaged results for all test runs are collected in Table 7.20 and 7.21. The accuracy of the identification in majority of the cases stays in 80% range, bar a few exceptions that fall into 70%. The accuracy depends on the subject of the collection: for the striated muscle collection the accuracy stays on 90.8% on average (see Table 7.20) with the weakest results for LR classifier that is the only one that falls below 90% threshold. For tissue samples of S40 collection the accuracy is 82.1% on average. There is not much in terms of disparity between the classifiers (see Table 7.20).

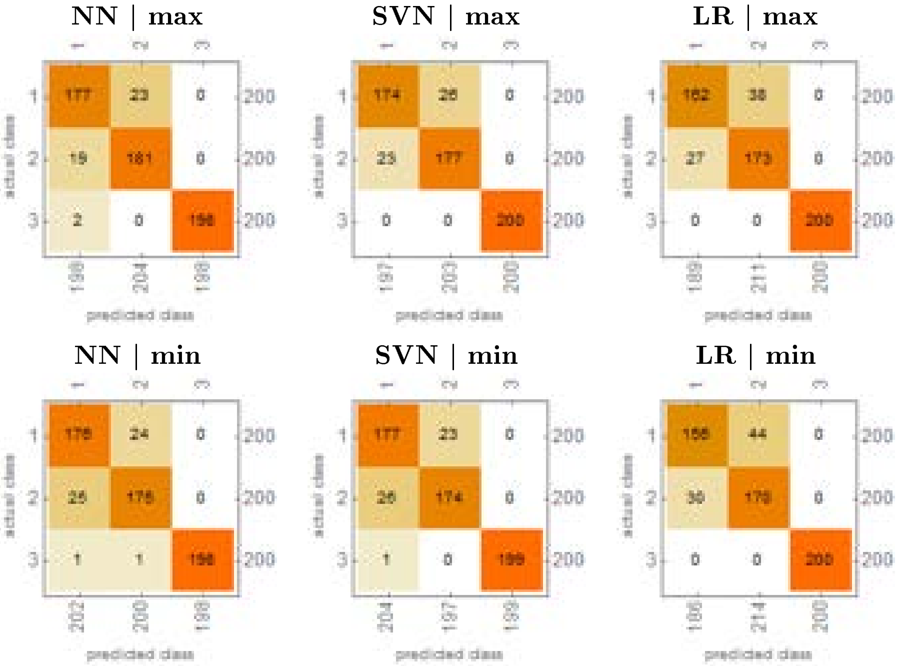
NN | max
SVN | max
LR | max
NN | min
SVN | min
LR | min

Figure 7.54: Minimum and maximum accuracy distribution for striated muscle collection in set-up #3.

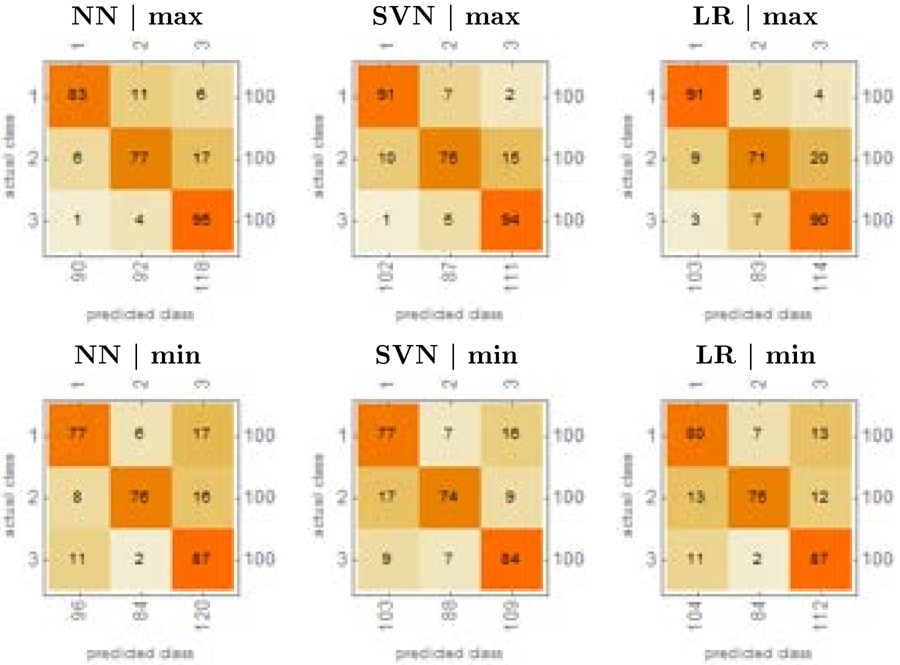
NN | max
SVN | max
LR | max
NN | min
SVN | min
LR | min

Figure 7.55: Minimum and maximum accuracy distribution for tissue S40 collection in set-up #3.

neural networks

	max	min	mean
striated	0,927	0,915	0,921
S40	0,850	0,800	0,822
all	0,927	0,800	0,855

support vector machines

	max	min	mean
striated	0,918	0,917	0,918
S40	0,867	0,783	0,823
all	0,918	0,783	0,854

logistic regression

	max	min	mean
striated	0,892	0,877	0,884
S40	0,840	0,807	0,820
all	0,892	0,807	0,841

Table 7.21: Collection of minimum, maximum and averaged values of achieved accuracy for all classifiers across all tissue collections. Set-up #3.

set-up #1

	max	min	mean
all	0,963	0,790	0,872
NN	0,930	0,830	0,874
SVM	0,963	0,790	0,888
LR	0,888	0,808	0,854

set-up #2

	max	min	mean
all	0,863	0,717	0,800
NN	0,830	0,782	0,803
SVM	0,863	0,807	0,835
LR	0,800	0,717	0,763

set-up #3

	max	min	mean
all	0,927	0,783	0,850
NN	0,927	0,800	0,855
SVM	0,918	0,783	0,854
LR	0,892	0,807	0,841

Table 7.22: Collection of minimum, maximum and averaged values of achieved accuracy for all classifiers across all tissue collections. All Set-ups.

Identification of unrelated tissue samples appears to work and does not disturb the detection of damaged samples within the collection. It proves that the method preforms up to expectations regardless of the presence of different tissues within the collection.

The summary of results for each set-up is displayed in Table 7.22. The distribution of results across all collections is displayed in Figure 7.56. The graphs show the minimum and maximum accuracy for each collection as well as the averaged value that is obtained across all testing set-ups and classifiers.

The results for the screening of the microscope image collections stay on the high-end of detection. Depending on the classification system the accuracy is spread starting from low 80% to high 80%/low 90% as shown in Table 7.22. The algorithm can differentiate between different types of tissue (set-up #3) and it can be tuned to identify tissue samples within the collection by given selection strat-

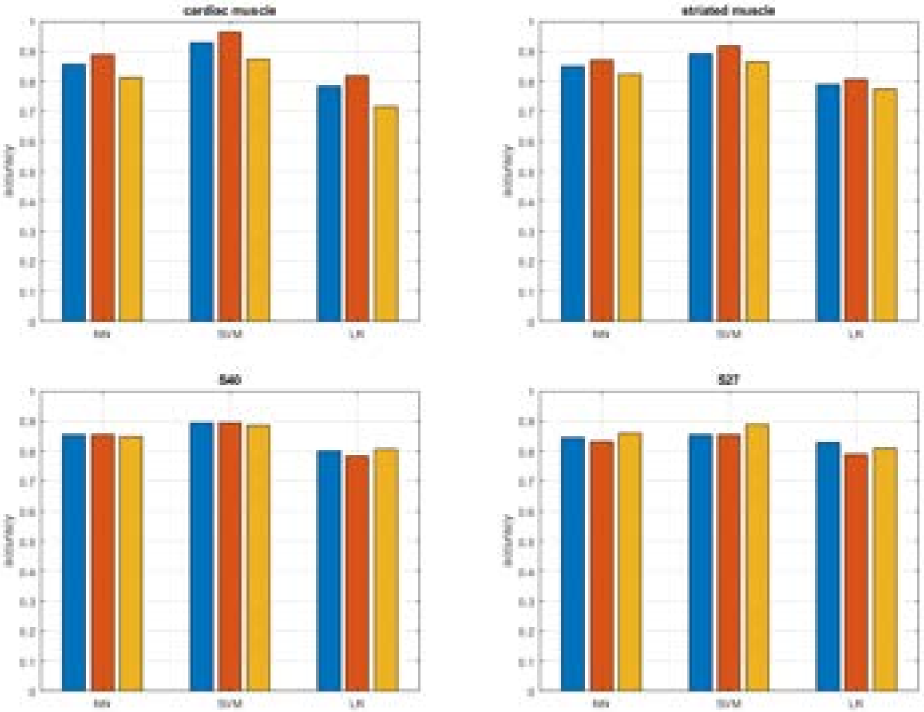

Figure 7.56: Highest identification scores for the sample collections. We compare three classifiers: NN - neural networks, SVM - support vector machines, LR - logistic regression. Blue - average, red - maximum, yellow - minimum values.

egy (set-up #1 and #2). Adjusting the threshold level for the decision metric can increase the accuracy of the detection providing a soft or hard elimination criterion for the process. It can be configured to create a dedicated detection/selection system for specified collections. It is a robust and highly accurate method for microscope image analysis that deals with preemptive data screening. Furthermore, it distinguishes itself by providing a single method to assess the microscope image collection in terms of potential errors of many types.

Chapter 8

Conclusions

The main goals of this thesis is to find new methods of approaching the problem of sequencing and identification of tissue samples in microscope images. In this case, our main tool are Zernike moments. We use them to construct image descriptors in the forms of vectors. Such descriptors make the basis of all our algorithms. Zernike moments were selected, because of their pattern-recognition properties which were proven in many past works. We cite some of them in Chapters 2 and 3.

The problem of sequencing finds use in sorting and ordering of microscope data. It occurs, because despite the order in the process of acquisition some histological sections may still come in the form of unordered slides. The reasons vary from simple human errors through imprecise methods of acquisition to just machine error. For the purpose of medical analysis it is often expected from the slides to be an ordered sequence with tissue aligned to the same origin point. We can point out a few image registration issues for this problem: the number of images to sort, the minimal differences between consecutive section slides, and translation and rotation of the tissue in the image. One of the key Zernike moments properties is that they can be made rotation- and translation-invariant. Modules of Zernike moments are rotation invariant by default. Translation-invariance can be achieved by centering the content of the image before any Zernike moment calculations. Descriptors built out of Zernike moments and accumulated Zernike moments retain some of these properties and because of that they are able to discriminate between slides. Detectio of such differences allows us to construct sequences of microscope slides. We further deployed machine learning alorithms (mostly neural networks) to estimate the order of slides using the descriptors as input data in place of microscope images. However, this method does not provide automatic adjustment of tissue in images as Zernike moments while are rotation-invariant, they do not provide enough information to align tissue in the slides. Thus, any alignment has to be done in post-processing and with other means. However, both the calculations of Zernike moment-based descriptors and sequencing with machine learning algorithms is a fully automatic process. Because the proposed approach does not adjust the content of the image, we cannot call the method fully successful.

In the second part of the thesis, we focused on the problems related to identification of tissue from microscope images. We can divide them into following categories: a classic problem of classification of tissue types, the problem of tissue identification by random sampling of the image, and the problem of detection of damage and other errors in tissue images. All algorithms ran on input data consisting of image descriptors using Zernike moments. We used two types of descriptors: a sequence of modules of Zernike moments, and a sequence of accumulated Zernike moments.

For the first type of the problem, we performed classification of four different types of vein tissue. As a classifier we used a simple MSE criterion. This approach did not prove effective, mostly because of the type of the classifier used. The MSE criterion used a straightforward differentiator which did not work well with Zernike moments. Zernike moment-based descriptors would require a classifer more attuned to pattern recognition. Therefore, we changed the strategy and started using classifiers which were based on machine learning algorithms like linear regression (LR), support vector machines (SVM) or neural networks (NN). In this case, we used microscope images of bronchial epithelium cells, lung pleura, striated muscle and tendon tissue as test data. This approach returned better results, with machine learning algorithms we were able to construct a classification criterion which allowed us to correctly classify different types of tissue based on the Zernike moment-based descriptors.

Microscope images often come in high-resolution format. Thus, a lot of work with microscope images covers managing big amount of data. Since histological sections are a complex subject on itself, such issues add on to the problem.

The previous solution focused on images of tissue which contained fragments of the tissue matching the phenotype of the tissue. Despite narrowing the pool of data such selection aimed to bolster the recognizability of the tissue by relying on the tissue matching the phenotype in major ways. However, we ran the risk of losing the effectivness of the algorithm against more diverse data. Previously, microscope images needed to be resized before any processing to bypass the issue of the size of the source image. Such approach lowered the quality of the source image, but improved the chances of recognizability by compressing the original image into smaller volume. In the case of this solution, we decided not to resize the source images. Instead, we sampled the original image, extracting small fragments which were then used in calculations. This way we lost access to entirety of the data, but at the same time this allowed us to retain the micro-level information from tissue images.

Our aim become identification of the tissue in the image using randomly sampled fragments of the tissue. We still used the Zernike moment-based descriptors of the image samples as input data, and we still used the machine learning algorithms like neural networks as our classification tools. We proved that using a few such samples can still lead to correct identification of the tissue. By increasing the number of samples utilized, we increased the chances of successful identification. At the same time, we effectively lessened the amount of the data which needed to be processed in the whole process, and we did not need to extensively interfere in the content of the image. This method has a wide range of potential applications in identification problems, where a very detailed and complex structures are the subject, e.g. histological section of tissue or satellite maps.

Since Zernike moment-based descriptors proved to be effective in identification and classification problems, we explored alternative uses of their properties. In the last case, we dealt with the problem of detecting damage and other errors in microscope images. The core of the method relies on the ability of the descriptors to identify matching images. On this ground it should also be possible to exclude images that do not match. We used the same data set as in the previous problem. However, this time we also included tissue images which had missing fragments or did not match the tissue phenotype in any form. The method proved that it is possible to use Zernike moment-based descriptors for this type of problem. The method had no issues with differentiating between complete and proper images of tissue and images of tissue which contained some defects (missing portions of the tissue, contamination in the image, etc.)

Zernike moment-based descriptors as well as their variant using accumulated Zernike moments proves to be an effective tool in many problems of microscope image analysis. The problems which were subject of this thesis included the sequencing of microscope images slides, identification and classification of the type of tissue using entire microscope images or through sampling, and detection of damage and other inconsistencies in images.

In Chapter 6, we described the problem of sequencing and ordering of slides in microscope image series. The problem occurs mostly, because in the process of acquisition, images of tissue sections may become misaligned and unordered. This is why we need methods to rectify these issues in order to obtain a sequence of slides which reflects the natural order and position of the tissue. Methods which allow us to sort and align such images become necessary. In our case, we mainly relied on descriptors based on accumulated Zernike moments in combination with edge histogram descriptors. Zernike moment-based descriptors were used as the input data in the process of constructing an ordered sequence of slides. The pattern-recognition properties of Zernike moments were enough to differentiate between various slides. Thus, the sequence was constructed on the basis of these minor differences. Images with the smallest differences between them were paired into adjacent slides. In the end, the entire sequence was constructed out of the chain of such small differences. The task of edge histogram descriptors was to align the tissue fragments into the same direction and orientation. Images showcasing the results of such sequencing are in shown in figures for this chapter. While Zernike moment-based descriptors were able to estimate the natural order of the sequence, they were unable to align content of the image on their own. However, this does not change that Zernike moment-based descriptors are able to describe images with complex patterns. But, it makes practical application of Zernike moment-based descriptors in the problem of ordering and sequencing somehow limited.

In chapter 7, the focus is on the problem of tissue identification. We consider three scenarios: identification of the tissue type and image classification using entire microscope images, identification of the tissue type using random samples from the source image and detection of damage in collections of microscope images of tissue.

In the first case, we establish whether Zernike moment-based descriptors can serve as means of identifying types of tissue in the image. Using machine learning algorithms like neural networks as classifiers and the descriptors as input data, we built an algorithm that allowed us to classify various tissue types in microscope images with high rate of success. In this approach, we also tested a composite classification algorithm which consisted of six different classifiers. It was implemented in order to improve the classification results. The purpose of this approach was to minimize the risk of incorrect classification by minimizing the influence of a singular incorrect classification on the decision, while bolstering other classifiers which might return positive results. Because of the processing power required in calculations of Zernike moments, calculating them for images with high resolution is taxing and not optimal. Therefore, it is often necessary to use microscope images which are downscaled. However, this approach may lead to loss of data from the images and as a result loose us some recognizability of the tissue. However, the proposed method still allows us to use Zernike moments for recognition of tissue types in microscope images. In most cases the accuracy of sample identification remains in the 90% level or higher. The method is easily scalable and can be used in more complex classification problems.

To bypass the downscaling issue, we slightly modified the approach. Instead of resizing the entire image, we sampled the source image in high resolution. From then, we used smaller, but still complex images of the tissue in the identification process. This approach allowed us to deliver a more accurate input data for classification. Howeverm choosing random fragments from a tissue image may not reflect on the entirety of the tissue in the image. Thus, we made the classification decision using a set of sampled images. This way, we provided quite thorough description of the tissue while reducing the number of data to process. The final classification decision was a cumulative decision of classification outputs for all samples. For classification, we used the same classification algorithms as in the previous cases (mostly neural networks). This approach delivered good results while reducing the cost of processing. The correct classification threshold started in the lower 90% if we included enough samples. Depending on the type and the complexity of the tissue the number of necessary samples varied and needed to be adjusted accordingly. Depending on the size of the source image and the number of samples that were used. We utilized around 1% of the source image to solve this classification problem.

Finally, we broadened the scope of application of Zernike moment-based descriptors and used them in the problem of detection of damage in microscope images of tissue. However, this time we taught the classification algorithm to differentiate between images of tissue which were whole and which were damaged in some capacity. The algorithm was capable of making this distinction. This allowed us to deploy automatic sorting of image collections where images of undamaged tissue were kept in the collection while damaged samples were removed from it. It not only removed human element from the process in a major way, but also sped up the processing. The results of the automated screening of the microscope image collections stayed on the high-end of detection. Depending on the classification system the accuracy spread from low 80% to high 80%/low 90% as shown in the mentioned chapter. The proposed algorithm can differentiate between different types of tissue, and it can be tuned to identify tissue samples within the collection using a given selection strategy.

In our approach, we propose another way of using Zernike moments in image description. We have two methods of constructing the decsriptor: with modules of Zernike moments and with accumulated Zernike moments. While the former is the usual take on Zernike moments, the latest is a completely new way of calculating Zernike moments for these types of problems. However, the main focus of the thesis remains the application of Zernike moments in problems of microscope image analysis like sequencing or classification of types of tissue in microscope images. Zernike moments are often used as tools in various problems related to shape recognition. However, in medical images this usually takes the form of localizing various ROIs. In our case, the pattern-recognition properties are used for the purpose of finding differences between images of microscope slides of the same tissue. Determining differences between consecutive images in the series allows us to sort images in the slide sequence. Another example of application is classification which relies on describing similarities between images using Zernike moments.

However, Zernike moments are used only in the form of image descriptors, therefore, for this problem we also have to use additional tools like neural networks to boost the process of building profiles of various types of tissue necessary to classification. This approach continues to be robust. It allows us to indentify tissue in microscope images at varying levels of magnitude (from medium magnification of 10X to very high magnification of 400X). Using this method it is possible to match images of different types of tissue raging from cardiac tissue, tendon, gray matter to vein tissue. We further expand on this topic by using small random samples from the source images of high resolution to identify the tissue. Such approach to the problem of image identification carries many positives. It allows us to identify tissue with complex internal structures without having to include the entire image in calculations. After calculating the Zernike moment-based descriptor once, it can serve as universal input data for many types of problems (classification, sequencing, damage detection). Using small parts of image reduces the time and the resource consumption. The algorithm allows us for automated sorting of tissue samples. Further, it allows us to build a collection of tissue samples while removing images that do not match the tissue, are empty or contain missing fragments. Automated sorting shortens the time and excludes human presence from the process.

In the beginning of this thesis, we focused on the sequencing of tissue slides with Zernike moment-based descriptors. Initially, we wanted to test the potential application of Zernike moments in the problem of sequencing. The approach relied on the idea that Zernike moments are sensitive enough to differentiate between microscope images of consecutive tissue slides. Building a path of the smallest differences between consecutive images allowed us to construct and optimal order of the sequence of microscope slides. However, the descriptors turned out not to be sensitive enough to unambiguously construct such sequence. Moreover, it still left us with the issue of the orientation of the content of the image since modules of Zernike moments are rotation invariant and rotation was not taken into the account in the process. Therefore, to obtain an ordered and properly oriented sequence postprocessing must take place.

Zernike moment-based descriptors proved much more effective in automated classification of types of tissue in microscope images. In classification, identification and similar problems we do not have to find the orientation and translation of the content of the image. We also do not have to rely on the error-free accuracy of the descriptor. Using neural networks we can build profiles of different types of tissue which constitute the input data of the classification. This allowed us to apply Zernike moment-based descriptors to multiple types of problems like recognition of types of tissue or detection of damage in tissue samples.

The sequencing turned out to be the most time-engaging part of the thesis while returning the least promising results. The sequencing was not as accurate as we assumed and some additional issues like rotation alignment turned out to need resolving in postprocessing. The second part of the thesis proved more fruitful. The automated identification of tissue samples with Zernike moment-based descriptors should be the main focus of the thesis. This is the most promising part of the thesis hich returns the best results.

The application of Zernike moment-based descriptors for the problem of tissue recognition in microscope images proved to be effective. We used this approach in the problems of sequence building of tissue slides, classification of different tissue types, identification of the tissue on the basis of random sampling from the microscope image and detection of damage in microscope images of tissue. However, the application of this approach needs not to be restricted to microscope image analysis. There are many venues which may benefit from these methods. Most likely this would be image analysis of images with characteristics similar to medical images. The most likely candidates would be analysis of images from satellites or recognition of human faces from images.

List of Figures

List of Tables

Bibliography

[1] S. Agarwal, A. K. Verma, P. Singh. Content based image retrieval using discrete wavelet transform and edge histogram descriptor. *2013 International Conference on Information Systems and Computer Networks*, strony 19–23. IEEE, 2013.

[2] S. Ahn, J. A. Fessler. Standard errors of mean, variance, and standard deviation estimators. *EECS Department, The University of Michigan*, strony 1–2, 2003.

[3] F. Alam, S. U. Rahman. Medical image registration: Classification, applications and issues. *JPMI*, 32(4):300, 2018.

[4] F. Alam, S. U. Rahman, S. Ullah, K. Gulati. Medical image registration in image guided surgery: Issues, challenges and research opportunities. *Biocybernetics and Biomedical Engineering*, 38(1):71–89, 2018.

[5] I. M. Alsaadi. Physiological biometric authentication systems, advantages, disadvantages and future development: A review. *International Journal of Scientific & Technology Research*, 4(12):285–289, 2015.

[6] I. Arganda-Carreras, R. Fernández-González, A. Muñoz-Barrutia, C. Ortiz-De-Solorzano. 3d reconstruction of histological sections: Application to mammary gland tissue. *Microscopy research and technique*, 73(11):1019–1029, 2010.

[7] R. Athilakshm, A. Wahi. Improving object classification using zernike moment, radial cheybyshev moment based on square transform features: a comparative study. *World Appl. Sci. J*, 32(7):1226–1234, 2014.

[8] M. Auer, P. Regitnig, G. A. Holzapfel. An automatic nonrigid registration for stained histological sections. *IEEE Transactions on Image Processing*, 14(4):475–486, 2005.

[9] U. Bagci, L. Bai. Fully automatic 3d reconstruction of histological images. *Biomedical Imaging: From Nano to Macro, 2008. ISBI 2008. 5th IEEE International Symposium on*, strony 991–994. IEEE, 2008.

[10] R. Baskar, K. A. Lee, R. Yeo, K.-W. Yeoh. Cancer and radiation therapy: current advances and future directions. *International journal of medical sciences*, 9(3):193, 2012.

[11] S. Bauer, R. Wiest, L.-P. Nolte, M. Reyes. A survey of mri-based medical image analysis for brain tumor studies. *Physics in Medicine & Biology*, 58(13):R97, 2013.

[12] S. Belongie, J. Malik, J. Puzicha. Shape matching and object recognition using shape contexts. *IEEE transactions on pattern analysis and machine intelligence*, 24(4):509–522, 2002.

[13] Y. Benard, N. Lopez-Gil, R. Legras. Subjective depth of field in presence of 4th-order and 6th-order zernike spherical aberration using adaptive optics technology. *Journal of Cataract & Refractive Surgery*, 36(12):2129–2138, 2010.

[14] W. Birkfellner, J. Wirth, W. Burgstaller, B. Baumann, H. Staedele, B. Hammer, N. C. Gellrich, A. L. Jacob, P. Regazzoni, P. Messmer. A faster method for 3d/2d medical image registration—a simulation study. *Physics in Medicine & Biology*, 48(16):2665, 2003.

[15] N. Bonnet. Some trends in microscope image processing. *Micron*, 35(8):635–653, 2004.

[16] M. Borga, T. Andersson, O. D. Leinhard. Semi-supervised learning of anatomical manifolds for atlas-based segmentation of medical images. *2016 23rd International Conference on Pattern Recognition (ICPR)*, strony 3146–3149. IEEE, 2016.

[17] M. Born, E. Wolf. The diffraction theory of aberrations principles of optics: Electromagnetic rheory of propagation, interference, and diffraction of light (ed., pp. 459-490), 1989.

[18] M. Born, E. Wolf. *Principles of optics: electromagnetic theory of propagation, interference and diffraction of light.* Elsevier, 2013.

[19] T. J. Carter, M. Sermesant, D. M. Cash, D. C. Barratt, C. Tanner, D. J. Hawkes. Application of soft tissue modelling to image-guided surgery. *Medical engineering & physics*, 27(10):893–909, 2005.

[20] L. A. Carvalho. Accuracy of zernike polynomials in characterizing optical aberrations and the corneal surface of the eye. *Investigative ophthalmology & visual science*, 46(6):1915–1926, 2005.

[21] A. Chaudhary, S. S. Singh. Lung cancer detection on ct images by using image processing. *2012 International Conference on Computing Sciences*, strony 142–146. IEEE, 2012.

[22] R. S. Choraś. Multimodal biometric personal authentication integrating iris and retina images. *Image Processing and Communications Challenges 2*, strony 121–131. Springer, 2010.

[23] R. S. Choras, i in. Ocular biometrics-automatic feature extraction from eye images. *10th WSEAS International Conference on Telecommunications and Informatics and Microelectronics, Nanoelectronics, Optoelectronics*, strony 179–183, 2011.

[24] W. R. Crum, T. Hartkens, D. Hill. Non-rigid image registration: theory and practice. *The British journal of radiology*, 77(suppl_2):S140–S153, 2004.

[25] J. Diedrichsen, J. H. Balsters, J. Flavell, E. Cussans, N. Ramnani. A probabilistic mr atlas of the human cerebellum. *Neuroimage*, 46(1):39–46, 2009.

[26] M. Doube, M. M. Kłosowski, I. Arganda-Carreras, F. P. Cordelières, R. P. Dougherty, J. S. Jackson, B. Schmid, J. R. Hutchinson, S. J. Shefelbine. Bonej: free and extensible bone image analysis in imagej. *Bone*, 47(6):1076–1079, 2010.

[27] R. R. Edelman. The history of mr imaging as seen through the pages of radiology. *Radiology*, 273(2S):S181–S200, 2014.

[28] I. El Naqa, P. W. Grigsby, A. Apte, E. Kidd, E. Donnelly, D. Khullar, S. Chaudhari, D. Yang, M. Schmitt, R. Laforest, i in. Exploring feature-based approaches in pet images for predicting cancer treatment outcomes. *Pattern recognition*, 42(6):1162–1171, 2009.

[29] M. Färber, J. Ehrhardt, H. Handels. Automatic atlas-based contour extraction of anatomical structures in medical images. *International Congress Series*, wolumen 1281, strony 272–277. Elsevier, 2005.

[30] D. C. Fernandez, R. Bhargava, S. M. Hewitt, I. W. Levin. Infrared spectroscopic imaging for histopathologic recognition. *Nature biotechnology*, 23(4):469–474, 2005.

[31] P. Filipczuk, T. Fevens, A. Krzyżak, A. Obuchowicz. Glcm and glrlm based texture features for computer-aided breast cancer diagnosis. *Journal of Medical Informatics & Technologies*, 19, 2012.

[32] C. P. Filson, S. Natarajan, D. J. Margolis, J. Huang, P. Lieu, F. J. Dorey, R. E. Reiter, L. S. Marks. Prostate cancer detection with magnetic resonance-ultrasound fusion biopsy: The role of systematic and targeted biopsies. *Cancer*, 122(6):884–892, 2016.

[33] J. M. Fitzpatrick, M. Sonka. Medical image processing and analysis. *Handbook of Medical Imaging, Medical Image Processing and Analysis*, 2:1108, 2000.

[34] J. Flusser, T. Suk, B. Zitová. *2D and 3D Image Analysis by Moments.* John Wiley & Sons, 2016.

[35] D. Fortin, P. S. Basran, T. Berrang, D. Peterson, E. S. Wai. Deformable versus rigid registration of pet/ct images for radiation treatment planning of head and neck and lung cancer patients: a retrospective dosimetric comparison. *Radiation Oncology*, 9(1):1–7, 2014.

[36] T. Gaens, F. Maes, D. Vandermeulen, P. Suetens. Non-rigid multimodal image registration using mutual information. *International Conference on Medical Image Computing and Computer-Assisted Intervention*, strony 1099–1106. Springer, 1998.

[37] R. C. Gonzales, R. E. Woods. *Digital Image Processing.* Upper Saddle River, NJ, USA: Prentice-Hall, Inc., 2006.

[38] E. P. Goodwin, J. C. Wyant. Field guide to interferometric optical testing. SPIE Bellingham, WA, 2006.

[39] A. Górniak, E. Skubalska-Rafajłowicz. Registration and sequencing of vessels section images at macroscopic levels. *IFIP International Conference on Computer Information Systems and Industrial Management*, strony 399–410. Springer, 2015.

[40] A. Górniak, E. Skubalska-Rafajłowicz. Object classification using sequences of zernike moments. *IFIP International Conference on Computer Information Systems and Industrial Management*, strony 99–109. Springer, 2017.

[41] A. Górniak, E. Skubalska-Rafajłowicz. Tissue recognition on microscopic images of histological sections using sequences of zernike moments. *IFIP International Conference on Computer Information Systems and Industrial Management*, strony 16–26. Springer, 2018.

[42] A. Górniak, E. Skubalska-Rafajłowicz. Automatic tissue type classification in large-scale microscopic images using zernike moments. *International Conference on Information Systems Architecture and Technology*, strony 310–319. Springer, 2019.

[43] S.-Y. Guan, T.-M. Wang, C. Meng, J.-C. Wang. A review of point feature based medical image registration. *Chinese Journal of Mechanical Engineering*, 31(1):1–16, 2018.

[44] E. Haber, J. Modersitzki. Numerical methods for volume preserving image registration. *Inverse problems*, 20(5):1621, 2004.

[45] J. Haddadnia, M. Ahmadi, K. Faez. An efficient feature extraction method with pseudo-zernike moment in rbf neural network-based human face recognition system. *EURASIP Journal on Advances in Signal Processing*, 2003(9):1–12, 2003.

[46] N. Hashimoto, P. A. Bautista, H. Haneishi, M. Snuderl, Y. Yagi. Development of a 2d image reconstruction and viewing system for histological images from multiple tissue blocks: towards high-resolution whole-organ 3d histological images. *Pathobiology*, 83(2-3):127–139, 2016.

[47] M. P. Heinrich, I. J. Simpson, B. W. Papież, M. Brady, J. A. Schnabel. Deformable image registration by combining uncertainty estimates from supervoxel belief propagation. *Medical image analysis*, 27:57–71, 2016.

[48] B. E. Henderson, J. R. Seamans. Image acquisition of microscopic slides. *Image Acquisition and Scientific Imaging Systems*, wolumen 2173, strony 21–27. International Society for Optics and Photonics, 1994.

[49] P. Hew, M. Alder. *Zernike Or Orthogonal Fourier-Mellon Moments for Representing and Recognising Printed Digits*. University of Western Australia. Department of Mathematics, 1998.

[50] D. L. Hill, P. G. Batchelor, M. Holden, D. J. Hawkes. Medical image registration. *Physics in medicine & biology*, 46(3):R1, 2001.

[51] H. Horstmann, C. Körber, K. Sätzler, D. Aydin, T. Kuner. Serial section scanning electron microscopy (s^3em) on silicon wafers for ultra-structural volume imaging of cells and tissues. *PloS one*, 7(4):e35172, 2012.

[52] N. Houhou, V. Duay, A. S. Allal, J.-P. Thiran. Medical images registration with a hierarchical atlas. *2005 13th European Signal Processing Conference*, strony 1–4. IEEE, 2005.

[53] M. B. Imran, S. A. Meo, M. Yousuf, S. Othman, A. Shahid. Medical image registration: basic science and clinical implications. *Journal of Ayub Medical College Abbottabad*, 22(2):199–204, 2010.

[54] A. Işın, C. Direkoğlu, M. Şah. Review of mri-based brain tumor image segmentation using deep learning methods. *Procedia Computer Science*, 102:317–324, 2016.

[55] G. James, D. Witten, T. Hastie, R. Tibshirani. *An introduction to statistical learning*, wolumen 112. Springer, 2013.

[56] S. Jeong, J. Lee, K. Sohn. Multi-domain unsupervised image-to-image translation with appearance adaptive convolution. *ICASSP 2022-2022 IEEE International Conference on Acoustics, Speech and Signal Processing (ICASSP)*, strony 1750–1754. IEEE, 2022.

[57] K. Kartasalo, L. Latonen, J. Vihinen, T. Visakorpi, M. Nykter, P. Ruusuvuori. Comparative analysis of tissue reconstruction algorithms for 3d histology. *Bioinformatics*, 34(17):3013–3021, 2018.

[58] S. Karthick, S. Maniraj. Different medical image registration techniques: a comparative analysis. *Current Medical Imaging*, 15(10):911–921, 2019.

[59] S. Keereweer, J. D. Kerrebijn, P. B. Van Driel, B. Xie, E. L. Kaijzel, T. J. Snoeks, I. Que, M. Hutteman, J. R. Van Der Vorst, J. S. D. Mieog, i in. Optical image-guided surgery—where do we stand? *Molecular Imaging and Biology*, 13(2):199–207, 2011.

[60] M. Kersten-Oertel, P. Jannin, D. L. Collins. The state of the art of visualization in mixed reality image guided surgery. *Computerized Medical Imaging and Graphics*, 37(2):98–112, 2013.

[61] V. S. Khoo, D. P. Dearnaley, D. J. Finnigan, A. Padhani, S. F. Tanner, M. O. Leach. Magnetic resonance imaging (mri): considerations and applications in radiotherapy treatment planning. *Radiotherapy and Oncology*, 42(1):1–15, 1997.

[62] A. Khotanzad, Y. H. Hong. Invariant image recognition by zernike moments. *IEEE Transactions on pattern analysis and machine intelligence*, 12(5):489–497, 1990.

[63] H. S. Kim, H.-K. Lee. Invariant image watermark using zernike moments. *IEEE transactions on Circuits and Systems for Video Technology*, 13(8):766–775, 2003.

[64] M. Kowal, P. Filipczuk, A. Obuchowicz, J. Korbicz, R. Monczak. Computer-aided diagnosis of breast cancer based on fine needle biopsy microscopic images. *Computers in biology and medicine*, 43(10):1563–1572, 2013.

[65] S. Krishnamurthy, S. S. Iyengar, R. J. Holyer, M. Lybanon. Histogram-based morphological edge detector. *IEEE Transactions on Geoscience and Remote Sensing*, 32(4):759–767, 1994.

[66] Y. Kumar, A. Aggarwal, S. Tiwari, K. Singh. An efficient and robust approach for biomedical image retrieval using zernike moments. *Biomedical Signal Processing and Control*, 39:459–473, 2018.

[67] P. T. Kuruganti, H. Qi. Asymmetry analysis in breast cancer detection using thermal infrared images. *Proceedings of the Second Joint 24th Annual Conference and the Annual Fall Meeting of the Biomedical Engineering Society][Engineering in Medicine and Biology*, wolumen 2, strony 1155–1156. IEEE, 2002.

[68] S. F. Lamoureux, J. Bollmann. Image acquisition. *Image analysis, sediments and paleoenvironments*, strony 11–34. Springer, 2005.

[69] S. G. Langer, S. J. Carter, D. R. Haynor, K. R. Maravella, D. Mattes, E. D. Strandness Jr, B. K. Stewart. Image acquisition: ultrasound, computed tomography, and magnetic resonance imaging. *World journal of surgery*, 25(11):1428–1437, 2001.

[70] S. Li, M.-C. Lee, C.-M. Pun. Complex zernike moments features for shape-based image retrieval. *IEEE Transactions on Systems, Man, and Cybernetics-Part A: Systems and Humans*, 39(1):227–237, 2008.

[71] S. X. Liao, M. Pawlak. On the accuracy of zernike moments for image analysis. *IEEE transactions on pattern analysis and machine intelligence*, 20(12):1358–1364, 1998.

[72] M. Liu, Y. He, B. Ye. Image zernike moments shape feature evaluation based on image reconstruction. *Geo-spatial Information Science*, 10(3):191–195, 2007.

[73] L. G. Luna. Manual of histologic staining methods of the armed forces institute of pathology. 1968.

[74] J. A. Maintz, M. A. Viergever. A survey of medical image registration. *Medical image analysis*, 2(1):1–36, 1998.

[75] J. B. A. Maintz, M. A. Viergever. An overview of medical image registration methods. Raport instytutowy, In Symposium of the Belgian hospital physicists association (SBPH-BVZF, 1996.

[76] A. Masood, B. Sheng, P. Li, X. Hou, X. Wei, J. Qin, D. Feng. Computer-assisted decision support system in pulmonary cancer detection and stage classification on ct images. *Journal of biomedical informatics*, 79:117–128, 2018.

[77] M. H. Modarres, R. Aversa, S. Cozzini, R. Ciancio, A. Leto, G. P. Brandino. Neural network for nanoscience scanning electron microscope image recognition. *Scientific reports*, 7(1):1–12, 2017.

[78] J. Modersitzki. *Numerical methods for image registration*. Oxford University Press on Demand, 2004.

[79] Z. Murez, S. Kolouri, D. Kriegman, R. Ramamoorthi, K. Kim. Image to image translation for domain adaptation. *Proceedings of the IEEE Conference on Computer Vision and Pattern Recognition*, strony 4500–4509, 2018.

[80] F. P. Oliveira, J. M. R. Tavares. Medical image registration: a review. *Computer methods in biomechanics and biomedical engineering*, 17(2):73–93, 2014.

[81] N. Otsu. A threshold selection method from gray-level histograms. *IEEE transactions on systems, man, and cybernetics*, 9(1):62–66, 1979.

[82] S. Ourselin, A. Roche, G. Subsol, X. Pennec, N. Ayache. Reconstructing a 3d structure from serial histological sections. *Image and vision computing*, 19(1-2):25–31, 2001.

[83] A. Padilla-Vivanco, A. Martinez-Ramirez, F.-S. Granados-Agustin. Digital image reconstruction using zernike moments. *Optics in Atmospheric Propagation and Adaptive Systems VI*, wolumen 5237, strony 281–289. International Society for Optics and Photonics, 2004.

[84] D. K. Park, Y. S. Jeon, C. S. Won. Efficient use of local edge histogram descriptor. *Proceedings of the 2000 ACM workshops on Multimedia*, strony 51–54, 2000.

[85] S.-K. Park, B.-S. Kim, S.-H. Jeong, H.-J. Kang, P.-J. Yoon. Lane estimation using lateral histogram in radar based acc system. *2014 11th European Radar Conference*, strony 193–196. IEEE, 2014.

[86] M. Pawlak. Image analysis by moments: reconstruction and computational aspects. *Oficyna Wydawnicza Politechniki Wrocławskiej*, 2006.

[87] E. S. Pearson, M. A. Stephens. The ratio of range to standard deviation in the same normal sample. *Biometrika*, 51(3/4):484–487, 1964.

[88] B. Qin, Z. Gu, X. Sun, Y. Lv. Registration of images with outliers using joint saliency map. *IEEE signal processing letters*, 17(1):91–94, 2009.

[89] A. Ramalingam, R. T. Selvi. An efficient zernike moments with logistic regression classifier based skin lesion diagnosis using dermoscopic images. *European Journal of Molecular & Clinical Medicine*, 7(9):1732–1742, 2020.

[90] P. B. Rao, D. V. Prasad, C. P. Kumar. Feature extraction using zernike moments. *International Journal of Latest Trends in Engineering and Technology*, 2(2):228–234, 2013.

[91] H. Ren, Z.-N. Li. Object detection using edge histogram of oriented gradient. *2014 IEEE International Conference on Image Processing (ICIP)*, strony 4057–4061. IEEE, 2014.

[92] L. Rundo, A. Tangherloni, C. Militello, M. C. Gilardi, G. Mauri. Multimodal medical image registration using particle swarm optimization: a review. *2016 IEEE Symposium Series on Computational Intelligence (SSCI)*, strony 1–8. IEEE, 2016.

[93] D. B. Russakoff, T. Rohlfing, C. R. Maurer Jr. Fast intensity-based 2d-3d image registration of clinical data using light fields. *ICCV*, wolumen 3, strona 416, 2003.

[94] T. Saba. Recent advancement in cancer detection using machine learning: Systematic survey of decades, comparisons and challenges. *Journal of Infection and Public Health*, 13(9):1274–1289, 2020.

[95] T. Saitou, H. Kiyomatsu, T. Imamura. Quantitative morphometry for osteochondral tissues using second harmonic generation microscopy and image texture information. *Scientific Reports*, 8(1):1–14, 2018.

[96] E. Scalco, G. Rizzo. Texture analysis of medical images for radiotherapy applications. *The British journal of radiology*, 90(1070):20160642, 2017.

[97] R. E. Schapire. The boosting approach to machine learning: An overview. *Nonlinear estimation and classification*, strony 149–171. Springer, 2003.

[98] J. Schreier, F. Attanasi, H. Laaksonen. A full-image deep segmenter for ct images in breast cancer radiotherapy treatment. *Frontiers in oncology*, 9:677, 2019.

[99] D. Sen, S. K. Pal. Gradient histogram: Thresholding in a region of interest for edge detection. *Image and Vision Computing*, 28(4):677–695, 2010.

[100] C. Shang, C. Daly, J. McGrath, J. Barker. Analysis and classification of tissue section images using directional fractal dimension features. *Proceedings 2000 International Conference on Image Processing (Cat. No. 00CH37101)*, wolumen 1, strony 164–167. IEEE, 2000.

[101] C. Singh, N. Mittal, E. Walia. Face recognition using zernike and complex zernike moment features. *Pattern Recognition and Image Analysis*, 21(1):71–81, 2011.

[102] Y. N. Singh, S. K. Singh. Evaluation of electrocardiogram for biometric authentication. 2011.

[103] E. Skubalska-Rafajłowicz. Estimation of horizontal and vertical translations of large images based on columns and rows mean energy matching. *Multidimensional Systems and Signal Processing*, 25(2):273–294, 2014.

[104] E. Skubalska-Rafajłowicz, A. Górniak. Kohonen som for image slides sequencing. *IFIP International Conference on Computer Information Systems and Industrial Management*, strony 352–365. Springer, 2016.

[105] G. Song, J. Han, Y. Zhao, Z. Wang, H. Du. A review on medical image registration as an optimization problem. *Current Medical Imaging*, 13(3):274–283, 2017.

[106] M. Sonka, J. M. Fitzpatrick. Handbook of medical imaging(volume 2, medical image processing and analysis). SPIE- The international society for optical engineering, 2000.

[107] M. Szymkowski, E. Saeed, M. Omieljanowicz, A. Omieljanowicz, K. Saeed, Z. Mariak. A novelty approach to retina diagnosing using biometric techniques with svm and clustering algorithms. *IEEE Access*, 8:125849–125862, 2020.

[108] A. Tahmasbi, F. Saki, S. B. Shokouhi. Classification of benign and malignant masses based on zernike moments. *Computers in biology and medicine*, 41(8):726–735, 2011.

[109] W. J. Tango. The circle polynomials of zernike and their application in optics. *Applied physics*, 13(4):327–332, 1977.

[110] M. R. Teague. Image analysis via the general theory of moments. *JOSA*, 70(8):920–930, 1980.

[111] G. Tian, H. Fu, D. D. Feng. Automatic medical image categorization and annotation using lbp and mpeg-7 edge histograms. *2008 International Conference on Information Technology and Applications in Biomedicine*, strony 51–53. IEEE, 2008.

[112] D. Tomazevic, B. Likar, F. Pernus. 3-d/2-d registration by integrating 2-d information in 3-d. *IEEE transactions on medical imaging*, 25(1):17–27, 2005.

[113] K. Trojacanec, G. Mirceva, D. Davcev. Application of edge histogram descriptor and region shape descriptor to mris. *ICT innovations conference*, strony 1–10, 2009.

[114] K. Vaidehi, T. Subashini. Automatic classification and retrieval of mammographic tissue density using texture features. *2015 IEEE 9th International Conference on Intelligent Systems and Control (ISCO)*, strony 1–6. IEEE, 2015.

[115] H. C. van Assen, M. Egmont-Petersen, J. H. Reiber. Accurate object localization in gray level images using the center of gravity measure: accuracy versus precision. *IEEE Transactions on Image Processing*, 11(12):1379–1384, 2002.

[116] P. A. Van den Elsen, E.-J. Pol, M. A. Viergever. Medical image matching-a review with classification. *IEEE Engineering in Medicine and Biology Magazine*, 12(1):26–39, 1993.

[117] P. Vikhar, P. Karde. Improved cbir system using edge histogram descriptor (ehd) and support vector machine (svm). *2016 International Conference on ICT in Business Industry & Government (ICTBIG)*, strony 1–5. IEEE, 2016.

[118] Q. D. Vu, S. Graham, T. Kurc, M. N. N. To, M. Shaban, T. Qaiser, N. A. Koohbanani, S. A. Khurram, J. Kalpathy-Cramer, T. Zhao, i in. Methods for segmentation and classification of digital microscopy tissue images. *Frontiers in bioengineering and biotechnology*, 7:53, 2019.

[119] C.-W. Wang, E. B. Gosno, Y.-S. Li. Fully automatic and robust 3d registration of serial-section microscopic images. *Scientific reports*, 5:15051, 2015.

[120] M. Wang, P. Li. A review of deformation models in medical image registration. *Journal of Medical and Biological Engineering*, 39(1):1–17, 2019.

[121] J. Wayman, A. Jain, D. Maltoni, D. Maio. An introduction to biometric authentication systems. *Biometric Systems*, strony 1–20. Springer, 2005.

[122] S. Wirtz, B. Fischer, J. Modersitzki, O. Schmitt. Superfast elastic registration of histologic images of a whole rat brain for 3d reconstruction. *Medical Imaging 2004: Image Processing*, wolumen 5370, strony 328–335. International Society for Optics and Photonics, 2004.

[123] C. S. Won, D. K. Park, S.-J. Park. Efficient use of mpeg-7 edge histogram descriptor. *ETRI journal*, 24(1):23–30, 2002.

[124] Q. Wu, F. Merchant, K. Castleman. *Microscope image processing*. Elsevier, 2010.

[125] Y. Xuan, P. Jihong. Elastic image registration using attractive and repulsive particle swarm optimization. *Asia-Pacific Conference on Simulated Evolution and Learning*, strony 782–789. Springer, 2006.

[126] H. Zhang, J. E. Fritts, S. A. Goldman. Image segmentation evaluation: A survey of unsupervised methods. *computer vision and image understanding*, 110(2):260–280, 2008.

[127] J. Zhang, J. Hu. Image segmentation based on 2d otsu method with histogram analysis. *2008 International Conference on Computer Science and Software Engineering*, wolumen 6, strony 105–108. IEEE, 2008.

[128] B. Zitova, J. Flusser. Image registration methods: a survey. *Image and vision computing*, 21(11):977–1000, 2003.